

2015

Fundamental studies and practical catalytic applications of silica encapsulated alloys synthesized using the inorganic capping agent and water-in-oil microemulsion approaches

Kyle Brashler
Iowa State University

Follow this and additional works at: <https://lib.dr.iastate.edu/etd>

 Part of the [Inorganic Chemistry Commons](#), [Materials Science and Engineering Commons](#), and the [Mechanics of Materials Commons](#)

Recommended Citation

Brashler, Kyle, "Fundamental studies and practical catalytic applications of silica encapsulated alloys synthesized using the inorganic capping agent and water-in-oil microemulsion approaches" (2015). *Graduate Theses and Dissertations*. 15884.
<https://lib.dr.iastate.edu/etd/15884>

This Thesis is brought to you for free and open access by the Iowa State University Capstones, Theses and Dissertations at Iowa State University Digital Repository. It has been accepted for inclusion in Graduate Theses and Dissertations by an authorized administrator of Iowa State University Digital Repository. For more information, please contact digirep@iastate.edu.

Fundamental studies and practical catalytic applications of silica encapsulated alloys synthesized using the inorganic capping agent and water-in-oil microemulsion approaches

by

Kyle Theodore Brashler

A thesis submitted to the graduate faculty
in partial fulfillment of the requirements for the degree of
MASTER OF SCIENCE

Major: Inorganic Chemistry

Program of Study Committee:
Wenyu Huang, Major Professor
Aaron Sadow
Igor Slowing

Iowa State University

Ames, Iowa

2015

Copyright © Kyle Theodore Brashler, 2015. All rights reserved.

TABLE OF CONTENTS

	Page
ACKNOWLEDGEMENTS.....	iii
ABSTRACT.....	iv
CHAPTER 1 – GENERAL INTRODUCTION	1
References.....	7
CHAPTER 2 – ELUCIDATING THE ORIGIN OF ENHANCED ACTIVITY AND CINNAMYL ALCOHOL SELECTIVITY IN CINNAMALDEHYDE HYDROGENATION OVER PERFLUORINATED LIGAND CAPPED Pt_5Fe_x SURFACES	13
Abstract.....	13
Introduction.....	14
Results and Discussion	19
Synthesis of Pt_5Fe_x Using High-Temperature Stable Mesoporous Silica as an Inorganic Capping Agent.....	19
Organic Capping Agent and Reactant Accessibility to $Pt_5Fe_x@mSiO_2$ Catalyst Surfaces.....	30
Understanding $Pt_5Fe_x@mSiO_2$ as a Cinnamaldehyde Hydrogenation Catalyst	40
Conclusions.....	50
Materials and Methods.....	51
References.....	58
CHAPTER 3 – WATER-IN-OIL MICROEMULSION PRODUCED SILICA NANOCAPSULES FOR A TWO STEP SYNTHESIS OF ALLOY NANOPARTICLES ENCAPSULATED IN MESOPOROUS SILICA	64
Abstract.....	64
Introduction.....	64
Results and Discussion	67
Bimetallic Alloy Formation with the Initial System.....	67
Ni@SiO ₂ as a Model Nanostructure to Improve the Initial System	70
Coating and Etching Ni@SiO ₂ Nanocapsules	74
Organic Additives for Enhanced Metal Loading	77
Shell Modifications for Enhanced Metal Loading.....	83
Conclusions.....	86
Materials and Methods.....	87
References.....	94
CHAPTER 4 – CONCLUSIONS AND FUTURE OPPORTUNITIES	99
References.....	103
APPENDIX – SUPPLEMENTAL INFORMATION FOR CHAPTER 2.....	105

ACKNOWLEDGEMENTS

I would like to thank my advisor, Wenyu Huang, for his help and guidance during his first few busy years as a faculty member at Iowa State. He has always pushed me to challenge myself and my ability to work smart and hard during my time as a graduate student has changed as a result. I would also like to thank Aaron Sadow and Igor Slowing, both of whom have decided to help me through my final months as members of my program of study committee.

I would also like to thank my colleagues for their advice and support during my time here. The post-doc in our research group, Chaoxian Xiao, has contributed to setting up all of our instruments and has volunteered numerous hours to help get them running smoothly. I will miss the other graduate students in my group and all of their quirks.

The undergraduate students I have worked with have been a huge help to me by running experiments I would not otherwise have time for. Jeff Gustafson has been with our group for two and a half years and has helped with both the study concerning cinnamaldehyde conversion over organic capping agent modified Pt-Fe surfaces and the water-in-oil microemulsion synthesis discussed in Chapters 2 and 3, respectively. Xuechen Luan has also helped synthesize $Pt_5Fe_x@mSiO_2$ nanoparticles for the study in Chapter 2.

I would like to thank my wife, Karin Lynn Brashler, for being patient with the late nights and weekends I've worked in the lab with hopes of better opportunities in our lives in the future. Thanks to my mom, dad, and sister, of whom have travelled to Ames and supported me.

ABSTRACT

Ordered alloys have been studied frequently as catalysts in recent years because of their modified electronic and geometric structure relative to monometallic catalysts. A recent report claims that perfluorinated ligands enhance the activity and cinnamyl alcohol selectivity during cinnamaldehyde hydrogenation over low temperature synthesized Pt-Fe catalysts, however, other publications discussing supported Pt-Fe alloys report enhanced catalytic properties without the need for hydrophobic perfluorinated ligand additives. One of the objectives of this thesis is to elucidate the effects of Fe and organic capping agents on the catalytic properties of Pt-Fe alloys during cinnamaldehyde hydrogenation.

Recently, mesoporous shells were reported for three-dimensional confinement of noble metal nanoparticles and offer enhanced thermal stability compared to columnar mesoporous supports and ligand-protected nanoparticulate catalysts. We have employed this motif to elucidate the roots of enhanced activity and cinnamyl alcohol selectivity in cinnamaldehyde hydrogenation over Pt_5Fe_x ($x = 0, 1, \text{ or } 2$) catalysts without organic capping agents or modified with saturated or perfluorinated capping agents. We show that added Fe enhances cinnamyl alcohol selectivity under all conditions, whereas perfluorinated ligands enhance activity over Pt_5Fe_2 reduced at 300 °C and Pt_5Fe reduced at 500 °C. We therefore believe that activity enhancements are affected by several factors, including Fe/Pt ratio, reduction temperature, ligand hydrophobicity, and support hydrophobicity, and are therefore difficult to predict.

While completing this fundamental study, we also synthesized 3D confined nanoparticles using water-in-oil microemulsions to develop a bimetallic system that is

easily scalable and contains tunable metal ratios and core sizes, which is necessary for industrial applications and correlating intermetallic phases with improved results. Metal precursors were coated with microporous silica in a one-pot process, and a one-pot coating and etching procedure was employed to create a yolk-shell structure with mesopores instead. The addition of organic modifiers containing amide, carboxylic acid, and sulfonic acid functional groups was also completed to confine metal ions to the core during etching steps. Our results provide the groundwork for the development of easily scalable mesoporous yolk-shell structures with tunable metal ratios in the future.

CHAPTER 1

GENERAL INTRODUCTION

Intermetallic compounds are solids that consist of two or more elements forming ordered phases that are often different from the structures of their constituent parent elements.¹ These compounds can contain mixes of electropositive and electronegative metals resulting in distinct combinations of covalent and ionic interactions as well as the presence of conducting electrons.² One can tune the electronic structure on the surface and in the bulk of such metals by changing metal ratios or the elements present to design intermetallic compounds for a unique application. For example, intermetallic compounds have been demonstrated as useful superconductors (MgB_2),³ thermoelectric devices ($\text{Sr}_8\text{Ga}_{16}\text{Ge}_{30}$),⁴ magnets (PtFe),⁵ hydrogen absorbers (ZrNiH_3),⁶ corrosion resistant coatings (FeSn_2),⁷ batteries (LaNi_5),⁸ and heterogeneous catalysts.⁹

Intermetallic compounds and ordered alloys are of interest in catalysis because an added second metal can modify the activity and selectivity of the catalytic surface on an active metal. This is achieved by modifying the adsorption energy of reactants, intermediates, and products on a catalytic surface or by altering the geometric effects of metal atoms on the surface. Geometric effects can isolate the catalytic active sites and make the surface more resistant to poisoning. This site isolation can also cause the catalyst to be more selective to a desired product by inhibiting specific reaction pathways as is seen in the case of acetylene hydrogenation on PdGa catalysts.¹⁰ Typically, electronic effects are the main determinants of the outcome of a reaction and geometric effects can be used for fine tuning of substrates adsorbing to the surface.¹¹

Another important aspect to consider when designing a bimetallic catalyst is the type of alloy present. If the alloy used is substitutional, then the structure can rearrange at high temperatures and form islands on the surface that are rich in one element.¹² As a result, the substrate adsorption properties of the surface change from those of ordered alloys to those of the constituent elements. As an alternative, many binary systems offer several structurally ordered intermetallic compounds that are resistant to this surface segregation at high temperatures, with each structure containing properties that are different from their individual elements. Atoms in intermetallic compounds adopt specific site locations because of chemical bonds formed in the structure,¹³⁻¹⁵ resulting in an exclusion of surface segregation and a preservation of a specific crystal and electronic structure under reaction conditions. As a result, intermetallic compounds tend to show enhanced stability and are currently being researched as alternatives to unstable alloys in the chemical industry.

Nanoparticulate metals used in catalytic studies are often loaded into two-dimensionally confined mesoporous supports, such as SBA-15,¹⁶⁻¹⁸ MCF-17,¹⁸⁻¹⁹ or MCM-41.^{16, 20} These supports are synthesized in a few steps and require small volumes of solvent compared to nanoparticulate supports, such as Stöber synthesized silica,²¹ that are synthesized in research labs. Additionally, these supports provide two-dimensional confinement of nanoparticles during low temperature processes by isolating particles within columnar channels. However, at higher temperatures nanoparticles within a single channel can diffuse, and sintering can result in decreased metal surface areas. This has a negative impact on catalytic activity. Recently, researches have published methods to prevent sintering from occurring by confining nanoparticles in three dimensions through

the use of SiO₂ shells,²²⁻²⁵ however, shell porosity is a concern if the reactants studied are too bulky.

Methods for loading metal precursors into industrial catalysts also rely on simple techniques such as incipient wetness impregnation and deposition-precipitation.²⁶ These methods are used because the loading of metals is easily scalable and the percentage of ionic metal loaded on the support is high. However, synthesizing catalysts using this method has some challenges that should be overcome when studying active sites on catalysts. For example, the formed nanoparticles can have a large distribution of particle sizes, and there is limited control over the element ratios in individual particles when the nanocrystalline alloys are annealed.²⁷ Large distributions in particle size can obscure conclusions between reported systems since it becomes more difficult to determine the surface area of the catalytic metal.

Additionally, it has been observed that several transition metals, included Au, Ag, Cu, Pd, and Ni have shifts in their core-level binding energies that alter substrate binding energies to the surface when the particle size is varied from bulk particles to less than 10 nm.²⁸ This results in a change in the electronic structure with particle size.²⁸ Selectivity during cinnamaldehyde hydrogenation over Pt catalysts has been shown to change with particle size.²⁹ Therefore, it is essential that monodisperse particle sizes are used for catalytic studies. Changes in element ratios on the surface of particles are also proportional to changes in element ratios in the bulk, which makes it necessary to ensure the ratios of metals in a sample is the same in every particle. For example, if a sample contains a 50/50 mixture of PtFe₃ and Pt₃Fe, it will also have different activities and

selectivities relative to a sample that is homogeneous in element composition, such as pure PtFe.

Methods for reducing metals before loading them into mesoporous silica are often employed to avoid these disadvantages. Often, metal nanoparticles are reduced in the presence of capping agents to control particle size,³⁰⁻³² shape,³³⁻³⁴ and to enhance long term stability.³⁵ Capping agents can also play a role during catalytic reactions by preventing certain orientations of reactants when they bond to the catalyst surface.³⁶⁻³⁷ This reduces the activity of the reaction, but can enhance the selectivity.³⁶ Contrariwise, if reactants experience noncovalent interactions with the hydrocarbon tail, hydrophobic ligands have been shown to increase the turnover frequency of reactions. Researchers are also searching for alternative capping and reducing agents to create environmentally friendly processes that rely on renewable resources. For example, ascorbic acid,³⁸ caffeine,³⁹ and glucose⁴⁰ have been reported as effective reducing and capping agents in the synthesis of Ag, Fe, and Pd nanoparticles, and may be preferable to capping agents that are derived from fuels, such as polyvinyl pyrrolidone.

The chemical industry is also experiencing new challenges as it is shifting to synthesizing chemicals from biomass feedstock as opposed to using natural gases and fossil fuels. For example, petroleum sources are hydrophobic, whereas biomass derived sources are hydrophilic because of the abundance of oxygen present in their molecular structure. As a result, more studies need to be done to find alternative pathways in the conversion of oxygenates to chemicals with practical applications. Several allylic and benzylic aldehydes can be derived from natural sources including furfural, acetophenone, citral and cinnamaldehyde.⁴¹ Studying the selective hydrogenation of C=O in the

presence of C=C bonds acts as a model for steps in the syntheses of fragrances (geraniol, nerol, bacdanol),⁴²⁻⁴³ pharmaceuticals [(8*E*,10*R*,12*Z*)-10-Hydroxy-8,12-octadecadienoic acid],⁴³⁻⁴⁴ and food additives (cinnamyl alcohol).^{43, 45} Ideally, hydrogenation of the α,β -unsaturated C=C bond should be prevented while hydrogenation of the C=O bond forms the desired product. However, hydrogenation of the α,β -unsaturated C=C bond is more thermodynamically favored over unmodified Pt catalysts.

This thesis discusses an elucidation of modifications that are necessary to improve selectivity in cinnamaldehyde hydrogenation over Pt catalysts. Several research groups have shown that addition of Fe, Sn, and Co to Pt has modified the electronic and geometric structure of the surface enough to provide significant selectivity to cinnamyl alcohol.^{36, 46-48} However, a recent report has discussed the possibility of perfluorinated ligands enhancing conversion and selectivity in this system.⁴⁹ Reviewing that recent report raises questions about the contributions a second metal or added capping agents have on activity and selectivity. Does adding a base metal, such as Fe, to a Pt surface play a bigger role in enhancing selectivity towards α,β -unsaturated aldehydes than adding capping agents to the system? Will one of these factors influence activity in the system more than the other? What causes the enhancement in activity and cinnamyl alcohol selectivity?

In this thesis in Chapter 2, we discuss the development of ligand protected Pt-Fe alloys using Pt encapsulated in a mesoporous silica shell as a starting material to answer these questions. The advantage to this system is the easy synthesis of control catalysts. Using this structure, we study Pt, Pt₅Fe, and Pt₅Fe₂ as Fe/Pt compositions, 300 °C, 500 °C, and 700 °C as reduction temperatures, and no ligand, decanoic acid, and

perfluorodecanoic acid as capping agent treatments. We confirm that cinnamaldehyde hydrogenation selectivity towards cinnamyl alcohol is enhanced through the addition of Fe to Pt catalysts, whereas perfluorinated ligands enhance the activity of the reaction in $\text{Pt}_5\text{Fe}_2@\text{mSiO}_2$ catalysts reduced at 300 °C and $\text{Pt}_5\text{Fe}@\text{mSiO}_2$ catalysts reduced at 500 °C.

While we were completing an important fundamental study, we also desired synthesizing a 3D confined intermetallic catalyst in high yields using a minimal amount of solvent, and we discuss our attempts at synthesizing this structure in Chapter 3. After further modifications and analysis, this project should have influential consequences in the chemical industry, because 3D confined nanoparticles are less prone to sintering compared to 2D confined particles in mesoporous channels.^{23, 50} The water-in-oil microemulsion method is an ideal method for synthesizing core-shell metal@SiO₂ particles in high yields because the small volume of water utilized during the synthesis is segregated from the oil phase using nonionic surfactants, such as Brij C10 or Igepal CO-520. A metal precursor can be dissolved in the water phase, and a silica shell can be grown around it in one step with high loading efficiencies.

Herein, progress towards the synthesis of scalable nanoscale systems with tunable metal ratios designed for liquid phase catalytic reactions is also discussed. The first structures described are the results of attempts at modifying a structure reported by Gao's research group to create a core-shell metal-silica structure that is easily scalable, porous, has a minimal number of synthesis steps, and has a metal core that is easily replaceable with other metals.²⁴ The reported method utilizes the water-in-oil microemulsion method

to synthesize 2.3 nm Au encapsulated with microporous silica that has demonstrated long term stability for the CO oxidation reaction when run under high temperature conditions.

There were some challenges when trying to repeat the reported synthesis of Au encapsulated with silica. It was observed that the shell thickness was not uniform throughout the samples and metal cores were not located in the center of particles. This could lead to metal cores escaping the silica shell and coalescing with other metal particles during high temperature treatments. The silica is also characterized as microporous, which limits the scope of the catalytic structure mainly to gas phase catalytic reactions. As a result, we also utilize a recently reported structure developed by Cai's research group.⁵¹ In their report, they discuss the synthesis of hollow mesoporous shells by coating and etching water-in-oil microemulsion synthesized SiO₂ in a single step. The larger pores would allow for the diffusion of bulkier molecules, allowing this structure to be tested in biomass conversion reactions in the future. However, we have found that the etching process also causes metal leaching and we discuss our utilization of organic additives containing amide, carboxylic acid, and sulfonic acid functional groups to minimize leaching during these steps. These results provide an excellent foundation towards the development of easily scalable yolk-shell structures with tunable metal ratios.

References

- (1) Atkins, P. O., T.; Rourke, J.; Weller, M.; and Armstrong, F., *Inorganic Chemistry*, 5th ed.; Oxford University Press, 2010.
- (2) Armbruster, M.; Schlögl, R.; Grin, Y., Intermetallic Compounds in Heterogeneous Catalysis-a Quickly Developing Field. *Sci. Technol. Adv. Mater.* **2014**, *15*, 17.

- (3) Choi, H. J.; Roundy, D.; Sun, H.; Cohen, M. L.; Louie, S. G., The Origin of the Anomalous Superconducting Properties of MgB₂. *Nature* **2002**, *418*, 758-760.
- (4) Nolas, G. S.; Cohn, J. L.; Slack, G. A.; Schujman, S. B., Semiconducting Ge Clathrates: Promising Candidates for Thermoelectric Applications. *Appl. Phys. Lett.* **1998**, *73*, 178-180.
- (5) He, C. N.; Zhao, N. Q., One-Step Solid-Phase Synthesis of Ultrasmall Homogeneous Face-Centered Tetragonal FePt Nanoparticles Encapsulated in Thin Carbon Shells. *J. Mater. Chem.* **2012**, *22*, 1297-1304.
- (6) Dantzer, P., Properties of Intermetallic Compounds Suitable for Hydrogen Storage Applications. *Materials Science and Engineering: A* **2002**, *329-331*, 313-320.
- (7) Sarafianos, N., Determining Reaction-Time at Iron Tin Interface of Electrolytic Tinplate During 1st Stage of FeSn₂ Growth. *Mater. Sci. Technol.* **1987**, *3*, 66-71.
- (8) Ovshinsky, S. R.; Fetcenko, M. A.; Ross, J., A Nickel Metal Hydride Battery for Electric Vehicles. *Science* **1993**, *260*, 176-181.
- (9) Xiao, C. X.; Wang, L. L.; Maligal-Ganesh, R. V.; Smetana, V.; Walen, H.; Thiel, P. A.; Miller, G. J.; Johnson, D. D.; Huang, W. Y., Intermetallic NaAu₂ as a Heterogeneous Catalyst for Low-Temperature CO Oxidation. *J. Am. Chem. Soc.* **2013**, *135*, 9592-9595.
- (10) Osswald, J.; Giedigkeit, R.; Jentoft, R. E.; Armbruster, M.; Girgsdies, F.; Kovnir, K.; Ressler, T.; Grin, Y.; Schlögl, R., Palladium-Gallium Intermetallic Compounds for the Selective Hydrogenation of Acetylene - Part I: Preparation and Structural Investigation under Reaction Conditions. *J. Catal.* **2008**, *258*, 210-218.
- (11) Gajdos, M.; Eichler, A.; Hafner, J., CO Adsorption on Close-Packed Transition and Noble Metal Surfaces: Trends from Ab Initio Calculations. *J. Phys.-Condes. Matter* **2004**, *16*, 1141-1164.
- (12) Zahn, D.; Haarmann, F.; Grin, Y., Atomistic Simulation Study of Cu(0.327)Ni(0.673) Alloys: From Solid Solution to Phase Segregation. *Z. Anorg. Allg. Chem.* **2008**, *634*, 2562-2566.
- (13) Armbruster, M.; Schnelle, W.; Cardoso-Gil, R.; Grin, Y., Chemical Bonding in Compounds of the CuAl₂ Family: MnSn₂, FeSn₂ and CoSn₂. *Chem.-Eur. J.* **2010**, *16*, 10357-10365.
- (14) Armbruster, M.; Schnelle, W.; Schwarz, U.; Grin, Y., Chemical Bonding in TiSb₂ and VSb₂: A Quantum Chemical and Experimental Study. *Inorg. Chem.* **2007**, *46*, 6319-6328.

- (15) Grin, Y.; Wagner, F. R.; Armbruster, M.; Kohout, M.; Leithe-Jasper, A.; Schwarz, U.; Wedig, U.; von Schnering, H. G., CuAl₂ Revisited: Composition, Crystal Structure, Chemical Bonding, Compressibility and Raman Spectroscopy. *J. Solid State Chem.* **2006**, *179*, 1707-1719.
- (16) Lee, B.; Ma, Z.; Zhang, Z. T.; Park, C.; Dai, S., Influences of Synthesis Conditions and Mesoporous Structures on the Gold Nanoparticles Supported on Mesoporous Silica Hosts. *Microporous Mesoporous Mat.* **2009**, *122*, 160-167.
- (17) Rioux, R. M.; Song, H.; Hoefelmeyer, J. D.; Yang, P.; Somorjai, G. A., High-Surface-Area Catalyst Design: Synthesis, Characterization, and Reaction Studies of Platinum Nanoparticles in Mesoporous SBA-15 Silica. *J. Phys. Chem. B* **2005**, *109*, 2192-2202.
- (18) Alayoglu, S.; Aliaga, C.; Sprung, C.; Somorjai, G. A., Size and Shape Dependence on Pt Nanoparticles for the Methylcyclopentane/Hydrogen Ring Opening/Ring Enlargement Reaction. *Catalysis Letters* **2011**, *141*, 914-924.
- (19) Tsung, C. K.; Kuhn, J. N.; Huang, W. Y.; Aliaga, C.; Hung, L. I.; Somorjai, G. A.; Yang, P. D., Sub-10 nm Platinum Nanocrystals with Size and Shape Control: Catalytic Study for Ethylene and Pyrrole Hydrogenation. *J. Am. Chem. Soc.* **2009**, *131*, 5816-5822.
- (20) Konya, Z.; Puentes, V. F.; Kiricsi, I.; Zhu, J.; Ager, J. W.; Ko, M. K.; Frei, H.; Alivisatos, P.; Somorjai, G. A., Synthetic Insertion of Gold Nanoparticles into Mesoporous Silica. *Chem. Mat.* **2003**, *15*, 1242-1248.
- (21) Stöber, W.; Fink, A.; Bohn, E., Controlled Growth of Monodisperse Silica Spheres in the Micron Size Range. *J. Colloid Interface Sci.* **1968**, *26*, 62-69.
- (22) Xiao, C. X.; Maligal-Ganesh, R. V.; Li, T.; Qi, Z. Y.; Guo, Z. Y.; Brashler, K. T.; Goes, S.; Li, X. L.; Goh, T. W.; Winans, R. E.; Huang, W. Y. High-Temperature-Stable and Regenerable Catalysts: Platinum Nanoparticles in Aligned Mesoporous Silica Wells. *ChemSusChem* **2013**, *6*, 1915-1922.
- (23) Joo, S. H.; Park, J. Y.; Tsung, C. K.; Yamada, Y.; Yang, P. D.; Somorjai, G. A., Thermally Stable Pt/Mesoporous Silica Core-Shell Nanocatalysts for High-Temperature Reactions. *Nat. Mater.* **2009**, *8*, 126-131.
- (24) Zhang, T. T.; Zhao, H. Y.; He, S. N.; Liu, K.; Liu, H. Y.; Yin, Y. D.; Gao, C. B., Unconventional Route to Encapsulated Ultrasmall Gold Nanoparticles for High-Temperature Catalysis. *ACS Nano* **2014**, *8*, 7297-7304.
- (25) Wu, C. Z.; Lim, Z. Y.; Zhou, C.; Wang, W. G.; Zhou, S. H.; Yin, H. F.; Zhu, Y. J., A Soft-Templated Method to Synthesize Sintering-Resistant Au-Mesoporous-

Silica Core-Shell Nanocatalysts with Sub-5 nm Single-Cores. *Chem. Commun.* **2013**, 49, 3215-3217.

- (26) Xiong, H. F.; Nolan, M.; Shanks, B. H.; Datye, A. K., Comparison of Impregnation and Deposition Precipitation for the Synthesis of Hydrothermally Stable Niobia/Carbon. *Appl. Catal. A-Gen.* **2014**, 471, 165-174.
- (27) Edwards, J. K.; Solsona, B. E.; Landon, P.; Carley, A. F.; Herzing, A.; Kiely, C. J.; Hutchings, G. J., Direct Synthesis of Hydrogen Peroxide from H₂ and O₂ Using TiO₂-Supported Au-Pd Catalysts. *J. Catal.* **2005**, 236, 69-79.
- (28) Rao, C. N. R.; Kulkarni, G. U.; Thomas, P. J.; Edwards, P. P., Size-Dependent Chemistry: Properties of Nanocrystals. *Chem.-Eur. J.* **2002**, 8, 29-35.
- (29) Durndell, L. J.; Parlett, C. M. A.; Hondow, N. S.; Isaacs, M. A.; Wilson, K.; Lee, A. F., Selectivity Control in Pt-Catalyzed Cinnamaldehyde Hydrogenation. *Sci. Rep.* **2015**, 5, #9425.
- (30) Sun, S.; Zeng, H.; Robinson, D. B.; Raoux, S.; Rice, P. M.; Wang, S. X.; Li, G., Monodisperse MFe₂O₄ (M = Fe, Co, Mn) Nanoparticles. *J. Am. Chem. Soc.* **2003**, 126, 273-279.
- (31) Yu, Y. S.; Yang, W. W.; Sun, X. L.; Zhu, W. L.; Li, X. Z.; Sellmyer, D. J.; Sun, S. H., Monodisperse MPt (M = Fe, Co, Ni, Cu, Zn) Nanoparticles Prepared from a Facile Oleylamine Reduction of Metal Salts. *Nano Lett.* **2014**, 14, 2778-2782.
- (32) Carencu, S.; Boissiere, C.; Nicole, L.; Sanchez, C.; Le Floch, P.; Mezailles, N., Controlled Design of Size-Tunable Monodisperse Nickel Nanoparticles. *Chem. Mat.* **2010**, 22, 1340-1349.
- (33) Cho, S.; Jung, S. H.; Lee, K. H., Morphology-Controlled Growth of ZnO Nanostructures Using Microwave Irradiation: From Basic to Complex Structures. *J. Phys. Chem. C* **2008**, 112, 12769-12776.
- (34) Zhang, H.; Jin, M. S.; Wang, J. G.; Kim, M. J.; Yang, D. R.; Xia, Y. N., Nanocrystals Composed of Alternating Shells of Pd and Pt Can Be Obtained by Sequentially Adding Different Precursors. *J. Am. Chem. Soc.* **2011**, 133, 10422-10425.
- (35) Kravchyk, K.; Protesescu, L.; Bodnarchuk, M. I.; Krumeich, F.; Yarema, M.; Walter, M.; Guntlin, C.; Kovalenko, M. V., Monodisperse and Inorganically Capped Sn and Sn/SnO₂ Nanocrystals for High-Performance Li-Ion Battery Anodes. *J. Am. Chem. Soc.* **2013**, 135, 4199-4202.
- (36) Wu, B. H.; Huang, H. Q.; Yang, J.; Zheng, N. F.; Fu, G., Selective Hydrogenation of Alpha, Beta-Unsaturated Aldehydes Catalyzed by Amine-Capped Platinum-

- Cobalt Nanocrystals. *Angewandte Chemie-International Edition* **2012**, *51*, 3440-3443.
- (37) Schoenbaum, C. A.; Schwartz, D. K.; Medlin, J. W., Controlling Surface Crowding on a Pd Catalyst with Thiolate Self-Assembled Monolayers. *J. Catal.* **2013**, *303*, 92-99.
- (38) Sondi, I.; Goia, D. V.; Matijevic, E., Preparation of Highly Concentrated Stable Dispersions of Uniform Silver Nanoparticles. *J. Colloid Interface Sci.* **2003**, *260*, 75-81.
- (39) Huang, L. L.; Weng, X. L.; Chen, Z. L.; Megharaj, M.; Naidu, R., Green Synthesis of Iron Nanoparticles by Various Tea Extracts: Comparative Study of the Reactivity. *Spectroc. Acta Pt. A-Molec. Biomolec. Spectr.* **2014**, *130*, 295-301.
- (40) Xu, L.; Wu, X. C.; Zhu, J. J., Green Preparation and Catalytic Application of Pd Nanoparticles. *Nanotechnology* **2008**, *19*, 6.
- (41) Claus, P., Selective Hydrogenation of Alpha, Beta-Unsaturated Aldehydes and Other C=O and C=C Bonds Containing Compounds. *Top. Catal.* **1998**, *5*, 51-62.
- (42) Saudan, L. A., Hydrogenation Processes in the Synthesis of Perfumery Ingredients. *Accounts Chem. Res.* **2007**, *40*, 1309-1319.
- (43) Ash, M. A., I., *Specialty Chemical Source Book*; Synapse Information Resources Inc.: New York, 1997.
- (44) Kashihara, H.; Suemune, H.; Fujimoto, K.; Sakai, K., A New Synthetic Route to Optically-Active Alpha, Beta-Unsaturated and Beta', Gamma'-Unsaturated Alcohols, and Its Application to the Synthesis of a Fungitoxic C-18 Hydroxy Unsaturated Fatty-Acid. *Chem. Pharm. Bull.* **1989**, *37*, 2610-2614.
- (45) Yadav, G. D.; Devendran, S., Lipase Catalyzed Synthesis of Cinnamyl Acetate Via Transesterification in Non-Aqueous Medium. *Process Biochem.* **2012**, *47*, 496-502.
- (46) Mahata, N.; Goncalves, F.; Pereira, M. F. R.; Figueiredo, J. L., Selective Hydrogenation of Cinnamaldehyde to Cinnamyl Alcohol over Mesoporous Carbon Supported Fe and Zn Promoted Pt Catalyst. *Appl. Catal. A-Gen.* **2008**, *339*, 159-168.
- (47) Gallezot, P.; Richard, D., Selective Hydrogenation of Alpha, Beta-Unsaturated Aldehydes. *Catal. Rev.-Sci. Eng.* **1998**, *40*, 81-126.
- (48) Taniya, K.; Hara, T.; Imai, T.; Ichihashi, Y.; Nishiyama, S., Preparation of Silica-Coated SnPt Bimetallic Nanoparticle Catalysts for the Selective Hydrogenation of Cinnamaldehyde. *J. Chem. Eng. Jpn.* **2014**, *47*, 130-135.

- (49) Vu, K. B.; Bukhryakov, K. V.; Anjum, D. H.; Rodionov, V. O., Surface-Bound Ligands Modulate Chemoselectivity and Activity of a Bimetallic Nanoparticle Catalyst. *ACS Catal.* **2015**, 2529-2533.
- (50) Yang, C. M.; Kalwei, M.; Schüth, F.; Chao, K. J., Gold Nanoparticles in SBA-15 Showing Catalytic Activity in CO Oxidation. *Applied Catalysis A: General* **2003**, 254, 289-296.
- (51) Chen, F.; Hong, H.; Shi, S. X.; Goel, S.; Valdovinos, H. F.; Hernandez, R.; Theuer, C. P.; Barnhart, T. E.; Cai, W. B., Engineering of Hollow Mesoporous Silica Nanoparticles for Remarkably Enhanced Tumor Active Targeting Efficacy. *Sci. Rep.* **2014**, 4, 10.

CHAPTER 2

ELUCIDATING THE ORIGIN OF ENHANCED ACTIVITY AND CINNAMYL ALCOHOL SELECTIVITY IN CINNAMALDEHYDE HYDROGENATION OVER PERFLUORINATED LIGAND CAPPED Pt_5Fe_x SURFACES

Kyle Brashler, Jeff Gustafson, Xuechen Luan, and Wenyu Huang

Department of Chemistry, U.S. DOE Ames Laboratory, Iowa State University, Ames, IA 50011-3111

Abstract

The hydrogenation of α,β -unsaturated aldehydes is an important type of reaction to study because it has applications in the flavoring, fragrance, and pharmaceutical industries. A recent paper has discussed an enhancement in activity and cinnamyl alcohol selectivity in a Pt_xFe catalysts during cinnamaldehyde hydrogenation reactions through the addition of perfluorinated capping agents. However, other publications report that adding Fe to Pt can enhance selectivity towards α,β -unsaturated aldehydes without adding capping agents. In this thesis, we developed a control system based on Pt encapsulated in mesoporous silica modified with added Fe, capping agents, and different reduction treatments to test this claim. It was found that adding perfluorinated capping agents enhances activity in Pt_5Fe_2 reduced at 300 °C and Pt_5Fe reduced at 500 °C, likely because the hydrophobic interactions between the perfluorocarbon tail and the arene ring present in cinnamaldehyde draw the reactant into the pore. On the other hand, cinnamyl alcohol selectivity was found to increase upon Fe addition to the catalyst. Additionally, high temperature treatments were found to further increase cinnamyl alcohol selectivity, possibly because the reduction in pore size in the mesoporous silica shell would lead to increased steric hindrance during reactions. DRIFTS studies were completed to show the interaction of capping agents with the catalyst surface, and XPS was completed to

understand the effects reduction temperatures and Fe/Pt ratios have on surface metal composition, activity, and cinnamyl alcohol selectivity.

Introduction

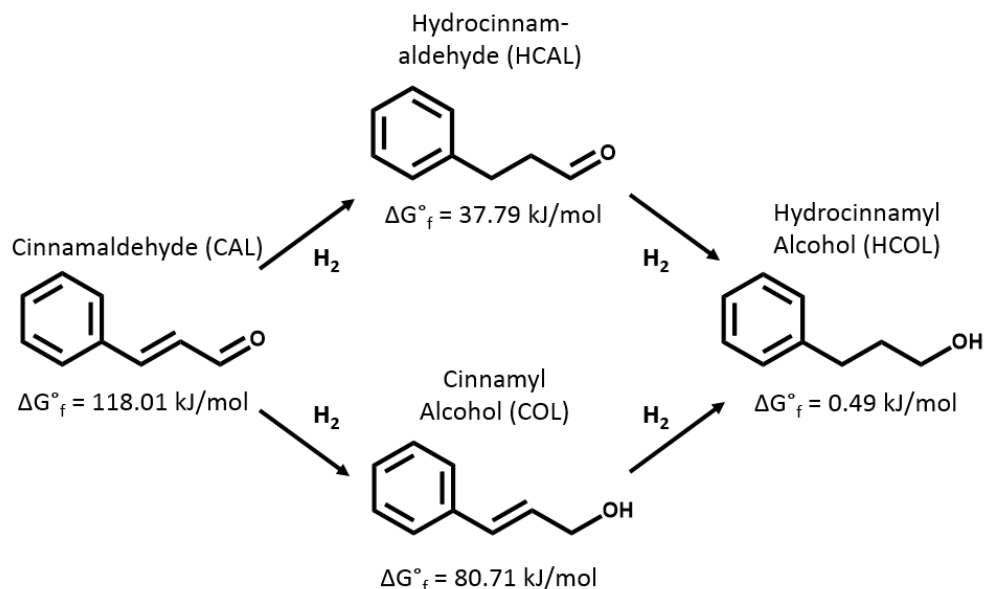
Catalytically active nanoparticles stabilized with organic ligands, also known as capping agents, have been well studied in the synthesis and applications of heterogeneous catalysts in liquid phase reactions.¹⁻⁹ These capping agents have been shown to add complexity to catalysts by sterically hindering the access of reactants to particle surfaces or by enhancing activity and cinnamyl alcohol selectivity by incorporating noncovalent interactions with reactants into the system.^{3, 6, 10} Several strategies have been used to remove capping agents from surfaces in order to make a clean and easily accessible surface for catalysis, including repeated washing steps,¹¹ UV and ozone treatment,¹²⁻¹⁵ thermal treatment,¹⁴⁻¹⁶ acid washing steps,^{15, 17} or ligand exchange with small adsorbates.¹⁸⁻¹⁹ However, when using these treatments it is uncertain how much the surface is clean afterwards, and if too high of a percentage of the surface adsorbates are removed the particles can aggregate.¹⁰ Additionally, when using acid washing or ligand exchange to remove ligands the leaching of base metals may occur.¹⁰

Researchers have also opted to study and utilize the noncovalent interactions induced by ligands instead of removing them.^{2, 20-22} It has been observed that the presence of substituents with saturated or perfluorinated hydrocarbon tails have hydrophobic and superhydrophobic properties, respectively, that result in enhanced affinity towards non-polar organic molecules²³ and an increase in catalytic activity.²⁴⁻²⁵ When products are more hydrophilic than reactants they are expelled from the catalyst surface. This results

in enhanced selectivity towards molecules with intermediate polarity, which is favorable when these molecules can further react on the catalyst surface.²⁶⁻²⁸ Several metals including Pt,^{6,9} Pd,^{6,9} Au,⁵ Rh,⁹ Ru,⁷ and Cu⁸ have been stabilized with ligands to allow them to disperse in liquid media for catalytic studies.

Platinum especially has been utilized in the chemical industry as a heterogeneous hydrogenation catalyst. Adding a base metal such as Co, Sn, or Fe induces geometric effects on the surface by blocking low index Pt sites that are not selective during cinnamaldehyde hydrogenation.²⁹ The second metal can also donate or withdraw electrons from the catalytic metal, therefore modifying the electronic effects in the system by changing adsorbate bonding energies.³⁰ The adjustment of geometric and electronic effects in bimetallic systems is tunable by changing the catalytic metal to base metal ratio allowing for a wide range of catalytic activity or selectivity results. Enhancement in chemoselectivity and activity after doping platinum with a base metal has been observed for several α,β -unsaturated aldehyde hydrogenation reactions including the hydrogenation of cinnamaldehyde,³¹ crotonaldehyde,³² and 5-hydroxymethylfurfural³³.

Cinnamaldehyde hydrogenation is an industrially important reaction because it acts as a model for the synthesis of other α,β -unsaturated alcohols in the pharmaceutical, flavor, and perfume industries.³⁴⁻³⁵ It is considered a challenge to selectively hydrogenate C=C bonds in the presence of aldehydes because α,β -saturated aldehydes are more thermodynamically stable than α,β -unsaturated alcohols (Scheme 1).³⁴ Cinnamyl alcohol selectivity can be enhanced by either inhibiting C=C bond hydrogenation or favoring hydrogenation of the C=O bond. Therefore, it is of interest to develop a system that can



Scheme 1. Cinnamaldehyde hydrogenation reaction products. Standard Gibbs free energy of formation values indicate that cinnamyl alcohol is the least favorable product when reacting cinnamaldehyde with H₂. Thermodynamic values were obtained from the Chemo High Quality Chemical Properties database.³⁶⁻³⁷

accomplish both of these feats through the addition of capping agents and base metals to modify geometric and electronic effects.

Vu and coworkers have recently designed a novel cinnamaldehyde hydrogenation catalyst that utilizes perfluorinated ligands as capping agents over Pt₃Fe and Pt₂Fe bimetallic surfaces.² Carboxylate anions were believed to have an exclusive affinity to surface Fe atoms, because this has been demonstrated in the adsorption of carboxylic acid and thiol containing ligands on PtFe surfaces.³⁸ Therefore, Pt was thought to remain accessible for reactions when the bimetallic surface is stabilized with carboxylate ligands. The perfluorinated ligand-capped Pt_xFe surfaces show an enhancement in cinnamyl alcohol selectivity and activity relative to saturated ligand-capped Pt (Table 1). However,

others have shown that addition of base metals, such as Fe,³⁹⁻⁴¹ Zn,³⁹ Co,^{40, 42} Ge,⁴⁰ or Sn^{31, 40} to Pt based catalysts already enhances activity and cinnamyl alcohol selectivity relative to monometallic catalysts during cinnamaldehyde hydrogenation.

Table 1. Cinnamaldehyde hydrogenation over ligand stabilized Pt, Pt₃Fe, and Pt₂Fe.^{a,b}

Catalyst	Capping Agent	Reaction Time (min)	Conversion (%) ^c	Selectivity (%) ^c		
				COL ^d	HCAL ^d	HCOL ^d
Pt	Oleic Acid	60	14.9	16.2	55.8	28.0
Pt ₃ Fe	Decanoic Acid	180	17.8	52.0	31.3	16.8
Pt ₃ Fe	Perfluorodecanoic Acid	90	43.1	91.8	4.4	3.8
Pt ₂ Fe	Perfluorodecanoic Acid	90	71.1	94.0	1.5	4.5

^aReported by Vu *et al.*'s research group.² ^bReaction Conditions: 500 μ L of n-hexane, 100 μ L of perfluorodecalin, 20 μ L of cinnamaldehyde, 1 atm of H₂, 50 °C, substrate/bulk metal = 125. ^cDetermined using GC-MS and NMR. ^dCinnamyl alcohol (COL), hydrocinnamaldehyde (HCAL), and hydrocinnamyl alcohol (HCOL).

As an example, Mahata and coworkers completed cinnamaldehyde hydrogenation studies over Pt-Fe catalysts supported on sol-gel carbon that was activated under flowing O₂.³⁹ They observed enhanced activity and cinnamyl alcohol selectivity after adding Fe to Pt, and attributed it to two factors: electron transfer from Fe to Pt, as evidenced through XPS analysis, and the creation of electrophilic sites on Fe suitable for cinnamaldehyde adsorption resulting from the electron transfer. The increased electron density in Pt causes a repulsive four-electron interaction between Pt and C=C bonds, but enhances the backbonding interaction with the antibonding pi orbitals in carbon monoxide. The results from this reaction are seen in Table 2. Fe addition was shown to enhance reaction results alone by Mahata and coworkers, and Vu and coworkers' published results require additional control studies to be completed with perfluorinated ligand-capped Pt to make the claim that perfluorodecanoic acid alone can enhance the activity and cinnamyl

alcohol selectivity. We applied our group's method of synthesizing high temperature stable ordered alloys⁴³ to investigate Vu and coworkers' assertion.

Table 2. Cinnamaldehyde hydrogenation over carbon supported Pt and Pt-Fe catalysts.^{a,b}

Catalyst	Pt wt.% ^c	Fe wt.% ^c	Pt ⁰ 4f _{7/2} B.E. (eV)	Pt ⁰ /Pt ²⁺ ratio	Conversion (%) ^d	Selectivity (%) ^d		
						COL ^e	HCAL ^e	HCOL ^e
Pt	5	-	72.1	4.18/1	45	42	45	13
Pt-Fe	5	0.8	71.7	3.57/1	99	59	1	40

^aReported by Mahata *et al.*'s research group.³⁹ ^bReaction Conditions: 100 mL of cyclohexane, 2 mL of cinnamaldehyde, 15.8 atm of H₂, 75 °C, 12 hrs, substrate/bulk metal = 207. ^cEstimated based on target metal wt.% during metal loading. ^dDetermined using GC. ^eCinnamyl alcohol (COL), hydrocinnamaldehyde (HCAL), hydrocinnamyl alcohol (HCOL).

We utilized a mesoporous silica shell (mSiO₂) as an inorganic capping agent as previously reported⁴⁴ to stabilize Pt nanoparticles during Fe addition, thermal treatment, and capping agent attachment processes to pinpoint the origin of enhanced activity and cinnamyl alcohol chemoselectivity in this system. By using XRD, TEM, and physisorption techniques we show that the particles and shell remain stable enough after 700 °C reduction treatments to allow for easy organic capping agent and reactant access to the particle surface. The structure is also stable outside of solution and was studied with XPS and DRIFTS to understand more about the surface composition, oxidation states, and organic capping agent bonding to particle surfaces. We applied the inorganic capping agent strategy to pinpoint the origins of enhanced activity and cinnamyl alcohol selectivity over organic capping agent modified bimetallic Pt₅Fe_x (x = 0, 1, or 2) by comparing cinnamaldehyde hydrogenation results in the presence or absence of Fe and hydrophobic organic capping agents.

Results and Discussion

Synthesis of Pt₅Fe_x Using High-Temperature Stable Mesoporous Silica as an Inorganic Capping Agent

The polyol synthesis⁴⁵⁻⁴⁶ of Pt₅Fe_x alloys was facilitated using tetraethylene glycol (TEG) as a high boiling point solvent and reducing agent in the presence of Pt@mSiO₂. The mSiO₂ acted as a mesoporous inorganic support that stabilized Pt particles against aggregation during high temperature syntheses. In preliminary experiments, several Fe salts were tested as potential metal precursors for the synthesis of Pt₅Fe_x bimetallic particles (Table 3). The salt was diluted to the proper concentration with a common solvent and the correct mass of salt was transferred using gravimetric measurements when low masses of salt precursor were used. Fe(acac)₃ was determined as the optimal precursor, because it was found to be soluble in acetone, which is a relatively low boiling point solvent that could be removed from the reaction flask before the experiment began. For the addition of Fe(acac)₃ to Pt@mSiO₂, it was determined that 200 °C would be the optimal reduction temperature because the possibility of Fe(acac)₃ reducing as separate nuclei in solution would be decreased. It should be noted that Fe(acac)₃ may have decomposed in solution and deposited on the mSiO₂ shell instead of receiving electrons after catalytic oxidation of TEG over the Pt surface, because the decomposition of acetylacetonate precursors is known to occur at temperatures below 300 °C.⁴⁷⁻⁴⁸

It was decided that it would be easier to observe the addition of the metal by using 1/1 ratios of Fe(acac)₃ precursor/Pt atoms in the Pt@mSiO₂ structures and look for the formation of the PtFe ordered face centered tetragonal phase using XRD to determine if

the synthesis was successful. Table 4 shows the ICP-MS results after analyzing the synthesized sample, and the Fe/Pt ratio was found to be approximately 4/5.

Table 3. Solvent induced reduction or decomposition of Fe precursors.

Fe Precursor	Precursor Solvent	Reaction Solvent	Initial Reduction Temperature	Final Reduction Temperature	Observation
Fe(acac) ₃	Acetone	TEG	183.7 °C	203.7 °C	Changes from Dark Red to Opaque
FeBr ₂	Acetone	TEG	-	> 320 °C	Light Red and Transparent
FeBr ₂	Acetone	Oleylamine	-	> 350 °C	Yellow and Transparent
FeCl ₃ ·6H ₂ O	Acetone	TEG	-	> 320 °C	Dark Yellow and Transparent
Fe(NO ₃) ₃ ·9H ₂ O	Water	TEG	197.7 °C	219.1 °C	Changes from Dark Red to Opaque

Table 4. ICP-MS calculated Fe/Pt ratios and metal wt.%^a

Sample	Target Fe/Pt Ratio	Actual Fe/Pt Ratio ^c	Fe Percent Yield ^{c,d}	wt.% Pt ^e	wt.% Fe ^e
Pt@mSiO ₂		-	-	44.9%	-
Pt ₅ Fe@mSiO ₂	0.33/1	(0.23 ± 0.01)/1	66 ± 3%	46.2%	3.0%
Pt ₅ Fe ₂ @mSiO ₂	0.50/1	(0.39 ± 0.04)/1	77 ± 9%	44.5%	4.8%
Pt ₅ Fe ₄ @mSiO ₂ ^b	1.00/1	(0.85 ± 0.08)/1	85 ± 8%	31.8%	7.7%

^aAll samples were oxidized at 550 °C for 6 hours before determining ICP-MS loading. ^bThis sample was additionally reduced at 700 °C for 6 hours before determining ICP-MS loading. ^cThree batches were averaged for Fe percent yield and Fe/Pt ratio for Pt₅Fe₂@mSiO₂ and Pt₅Fe@mSiO₂, whereas three ICP measurements were averaged for Fe percent yield and Fe/Pt ratio for Pt₅Fe₄@mSiO₂. ^dThis value was calculated by dividing the actual Fe yield determined using ICP-MS after Fe(acac)₃ reduction by the theoretical amount obtainable. ^ePt₅Fe₂, Pt₅Fe, and Pt were all synthesized from a single batch of catalyst for wt.% determination.

To see if the degree of crystal ordering in the structure could be tuned and tested at various temperatures, high temperature treatments were completed on the Pt₅Fe₄@SiO₂ sample. After heating the sample to 600 °C, superlattice peaks corresponding to the formation of ordered Pt-Fe alloys begin to form and are present at $2\theta = 23^\circ$ and 32° . A peak at 48° that corresponds to the PtFe phase is also present after reducing the sample at

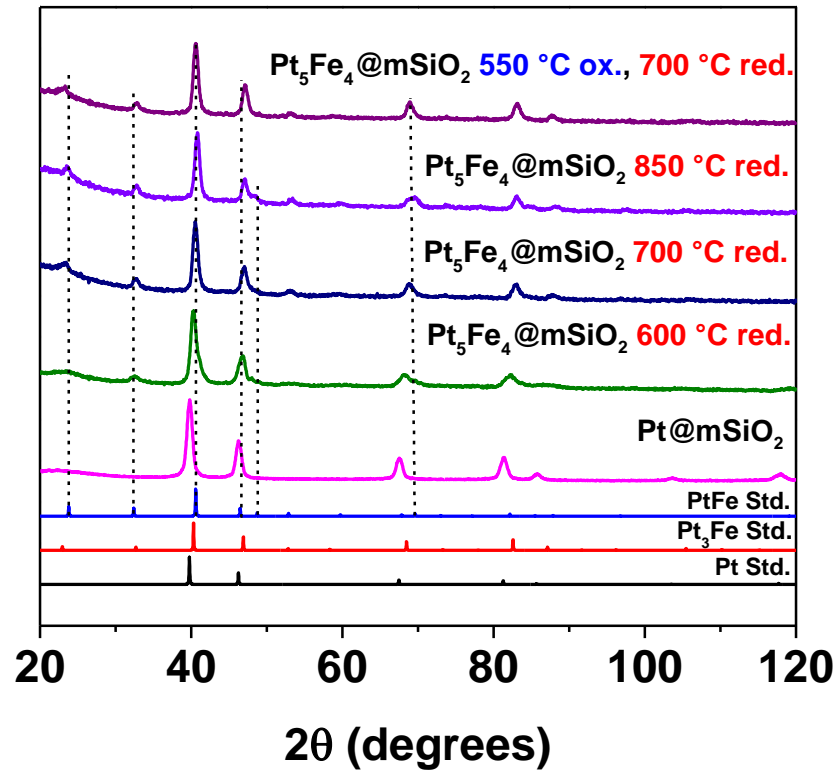


Figure 1. Changes in diffraction pattern of $\text{Pt}_5\text{Fe}_4@m\text{SiO}_2$ samples with changing heat treatment conditions indicates increasing order with increasing temperature.

850 °C (Figure 1). Additionally, the intense peak present between 39° and 41° shifts to higher angles with higher reduction temperatures (Table 5). However, Vu and coworkers completed their study over Pt-Fe alloys synthesized at low temperatures that still exhibited the fcc phase,² so 700 °C was the maximum temperature that was examined in our system. For catalytic measurements it is important that the silica shell is porous, therefore, an oxidation treatment was added before the high temperature reduction treatment to remove residual TEG and acetone. The Scherrer equation was used to calculate changes in crystallite size as follows:

$$\tau = K\lambda/(\beta\cos\theta) \quad (1)$$

Table 5. Crystallite size increase upon thermal treatment of Pt₅Fe_x@mSiO₂ alloys.

Sample	Oxidation Temperature (°C) ^a	Reduction Temperature (°C) ^b	Reduction Time (hrs)	Crystallite Size (nm)	Primary Peak Location (°)
Pt@mSiO ₂	-	-	-	10.7 ± 0.2	39.78
Pt ₅ Fe ₄ @mSiO ₂	-	600	6	10.3 ± 1.3	40.18
Pt ₅ Fe ₄ @mSiO ₂	-	700	6	10.7 ± 0.3	40.49
Pt ₅ Fe ₄ @mSiO ₂	-	850	1	11.3 ± 0.3	40.78
Pt ₅ Fe ₄ @mSiO ₂	550	700	6	12.3 ± 0.2	40.58
Pt@mSiO ₂ ^c	550	700	6	10.8 ± 0.2	39.84
Pt ₅ Fe@mSiO ₂ ^c	550	700	12	11.4 ± 0.2	40.28
Pt ₅ Fe ₂ @mSiO ₂ ^c	550	700	12	12.0 ± 0.3	40.25

^aSamples were oxidized in air as follows: they were dried at 100 °C for 2 hours, heated to 550 °C with a rate of 1 °C/min, and kept at 550 °C for 6 hours. ^bSamples were reduced in 10% H₂/Ar with a rate of 1 °C/min. ^cSamples were made from the same large mixed batch of Pt@mSiO₂.

In Equation 1, K is the crystallite shape factor, can vary depending on the geometry of the particle analyzed, and usually is estimated as 0.9. λ is the wavelength of light, θ is the angle at which a local maxima of constructive interference is observed, β is the full width at half maximum of the peak observed at that angle, and τ is the calculated crystallite size. As observed in Table 5, the particle size increased when including a high temperature calcination treatment before reducing at 700 °C. More Fe was likely incorporated into the structure, but no additional peak shift was observed because the PtFe phase can form over a wide range of Fe/Pt ratios as seen in Figure 2. After observing a shift corresponding to the PtFe phase in the Pt₅Fe₄@mSiO₂ sample, the synthesis of Pt₂Fe@mSiO₂ and Pt₃Fe@mSiO₂ was attempted from a single, large batch of Pt@mSiO₂. The ICP-MS estimated Fe/Pt ratios after attempting the synthesis with Fe/Pt ratios of 1/2 and 1/3 were 1/2.5 and 1/5, respectively. These samples had structures corresponding to the Pt₃Fe phase and an increase in crystallite size was also observed after adding Fe to the structure (Figure 3 and Table 5).

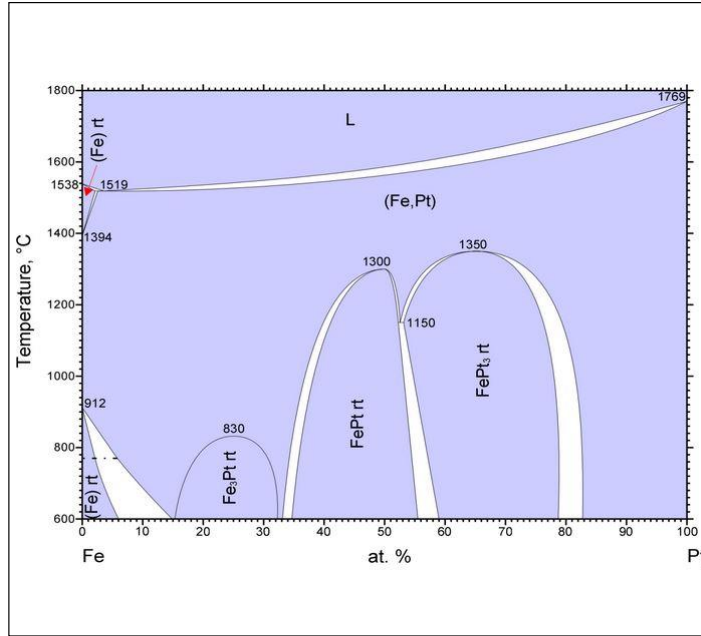


Figure 2. Pt-Fe phase diagram showing that PtFe and Pt₃Fe phases form over a wide range of Fe/Pt ratios.⁴⁹

TEM images from the samples were collected to confirm the stability of the Pt₅Fe_x@mSiO₂ samples after the calcination and reduction conditions were completed (Figure 4). The Pt₅Fe₄@mSiO₂ sample reduced at 850 °C is visible in Figure 4a. The lattice in the Pt₅Fe₄@mSiO₂ particles after reducing the sample at 850 °C has a spacing between the {101} planes equal to 0.220 nm. This corresponds to a lattice spacing most similar to the PtFe phase, which has a distance of 0.222 nm. The experimental lattice spacing can also be calculated from the angle of the most intense peak observed for the 850 °C reduced Pt₅Fe₄@mSiO₂ sample seen in Figure 1 using Bragg's Law:

$$n\lambda = 2d\sin\theta \quad (2)$$

In Equation 2, n is a positive integer, λ is the wavelength of incident radiation, d is the spacing observed in the lattice, and θ is the angle at which constructive interference

is the strongest. In X-ray diffraction, n is unity and the equation can be rearranged to give:

$$d = \lambda / (2 \sin \theta) \quad (3)$$

The $\text{Pt}_5\text{Fe}_4@\text{mSiO}_2$ sample therefore has a lattice spacing of 0.221 nm when using the angle at $2\theta = 40.78^\circ$. This value is in close agreement to the particle observed in Figure 4b, confirming that the particle observed is a representative nanoparticle of the entire sample.

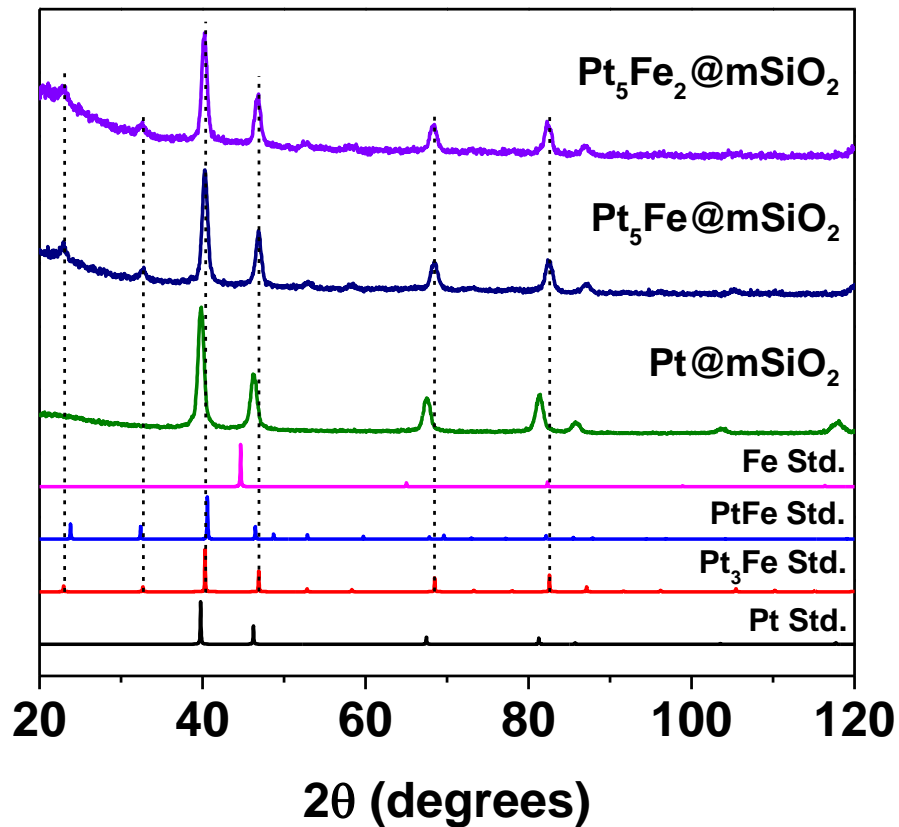


Figure 3. Diffraction patterns of obtained $\text{Pt}_5\text{Fe}_2@\text{mSiO}_2$ and $\text{Pt}_5\text{Fe}@\text{mSiO}_2$ samples after attempting to synthesize $\text{Pt}_2\text{Fe}@\text{mSiO}_2$ and $\text{Pt}_3\text{Fe}@\text{mSiO}_2$, respectively.

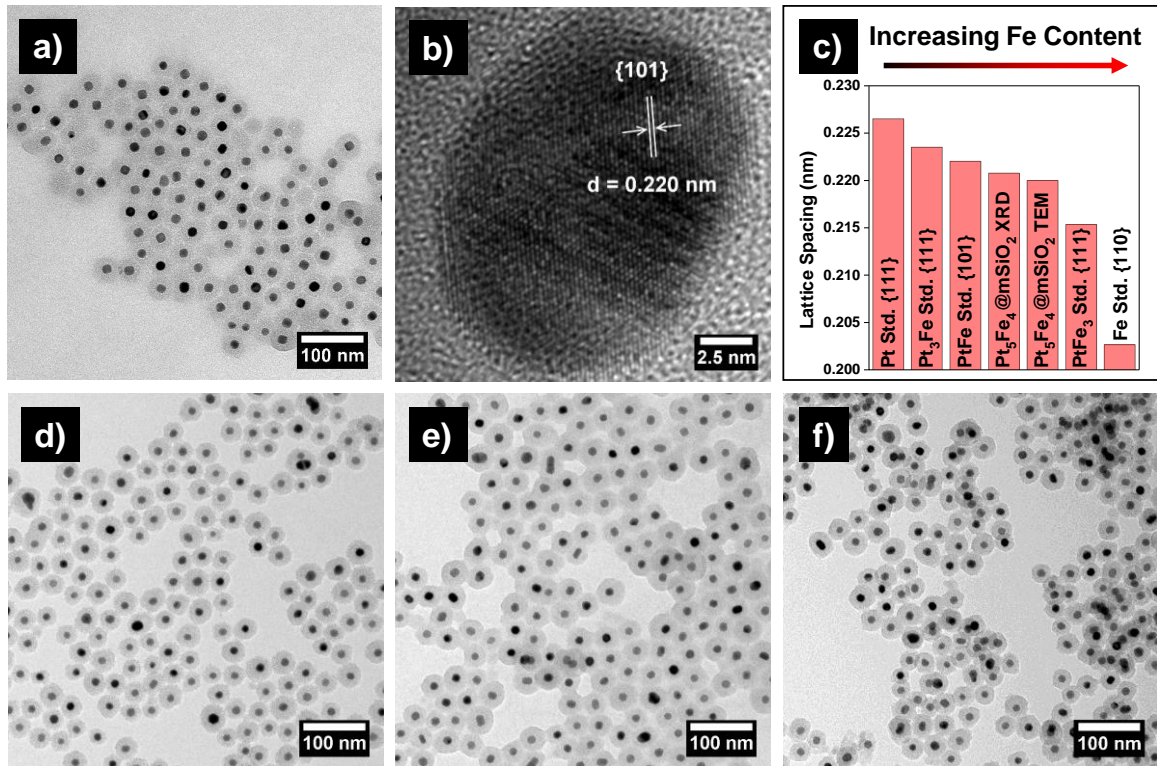


Figure 4. a) Pt₅Fe₄@mSiO₂ after 850 °C reduction. b-c) Calculated lattice spacing of Pt₅Fe₄@mSiO₂ XRD peak at $2\theta = 40.78^\circ$ is similar to the high resolution image of Pt₅Fe₄@mSiO₂ particle. Both have a lattice spacing most similar to PtFe phase. d-f) All 3 images are after 550 °C calcination and 700 °C reduction. d) Pt@mSiO₂ used to synthesize e) Pt₅Fe@mSiO₂ and f) Pt₅Fe₂@mSiO₂.

It should be noted that Vegard's law can be used to estimate the metal compositions of binary alloys if the crystal structure does not change when altering metal ratios:

$$d_{AB} = a \times d_A + (1 - a) \times d_B \quad (4)$$

In Equation 4, d_{AB} is the lattice parameter of the solid solution, whereas d_A and d_B are the lattice parameters of the individual components. The atomic percentage of metal A is denoted as a . It is known that Pt, Pt₃Fe, and PtFe₃ have face centered cubic crystal

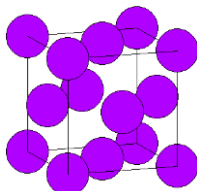
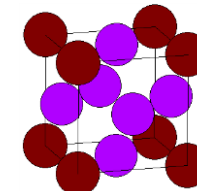
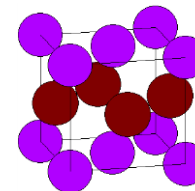
structures, whereas high temperature reduced PtFe has a face centered tetragonal crystal structure and Fe exhibits the body centered cubic crystal structure. Therefore, there is a proportionality between the lattice spacing shift and the amount of Fe in the alloy if we are comparing Pt to Pt₃Fe, but Vegard's law is not applicable if the Fe concentration is greater than 25% because of the change in crystal structure. Therefore, in our study, comparison of lattice spacings with standards is used as a fingerprinting technique instead of for determining metal ratios.

When comparing the Pt@mSiO₂ sample in Figure 4d to the Pt₅Fe@mSiO₂ and Pt₅Fe₂@mSiO₂ samples in Figures 4e and 4f, respectively, it can also be observed that the thin mSiO₂ shell present during the addition of the Fe is not etched away during synthesis, reduction, or calcination processes. Additionally, when using 700 °C as the reduction temperature no catalytic core sintering is observed, indicating that the high temperature stability of our system allows a large range of reduction temperatures to be utilized to determine the best reduction temperature when preparing Pt₅Fe_x bimetallic samples for cinnamaldehyde hydrogenation.

After synthesizing Pt₅Fe_x@mSiO₂ with different Fe/Pt ratios and reducing them at high temperatures to ensure Fe is incorporated into the core particle, the particle size increase should be proportional to volume changes in the unit cells of reported Pt-Fe alloys. A theoretical increase was calculated based on a volumetric changes after adding Fe to a Pt unit cell (Table 6). This was compared to the size increases observed in TEM and XRD after adding Fe to Pt@mSiO₂ samples, as seen in Figure 5, Table 7, and Table 8. When using linear interpolation to estimate the Fe content, the size increase of the particles observed with TEM underestimates the Fe content in the samples relative to

ICP-MS for all samples. However, the XRD crystallite size estimated Fe content was underestimated only in the Pt₅Fe₄@mSiO₂ sample.

Table 6. Theoretical expansion of Pt crystal structure after incorporating Fe into the lattice.

	Pt	Pt ₃ Fe	PtFe
Unit Cell ^a			
h (Å)	3.923	3.872	3.849
k (Å)	3.923	3.872	3.849
l (Å)	3.923	3.872	3.700
Unit Cell Volume (Å ³)	60.38	58.05	54.82
Scaled Cell Volume (Å ³) ^b	60.38	77.40	109.6
Ratio of Pt _x Fe _y /Pt Scaled Cell Volumes	1.000	1.282	1.816
Ratio of Pt _x Fe _y /Pt Scaled Cell Diameters ^c	1.000	1.086	1.220

^aUnit cell dimensions obtained from ICSD no. 76153 (Pt), 42588 (Pt₃Fe), and 659004 (PtFe). Structures were simulated using the Visualizer program available on FindIt software.⁵⁰ ^bVolume containing 4 Pt atoms after adding Fe. ^cCalculated from cube root of values in the "Ratio of Pt_xFe_y/Pt Scaled Cell Volumes" row.

There are a few reasons underestimation is possible. The large standard deviation during particle size counting is a result of systematic error associated with using an automatic counting technique. As a result, there could be no significant difference between the TEM and ICP-MS estimated Fe/Pt ratios. However, a different particle size could be observed if some of the Fe forms an iron-silicate structure with the mSiO₂ shell instead of alloying with the Pt core.⁵¹ Additionally, Fe might have oxidized and formed

oxides on the surface of the Pt core during TEM preparation. This would have a different contrast compared to the bimetallic core and influence the observed shell size during particle size counting.

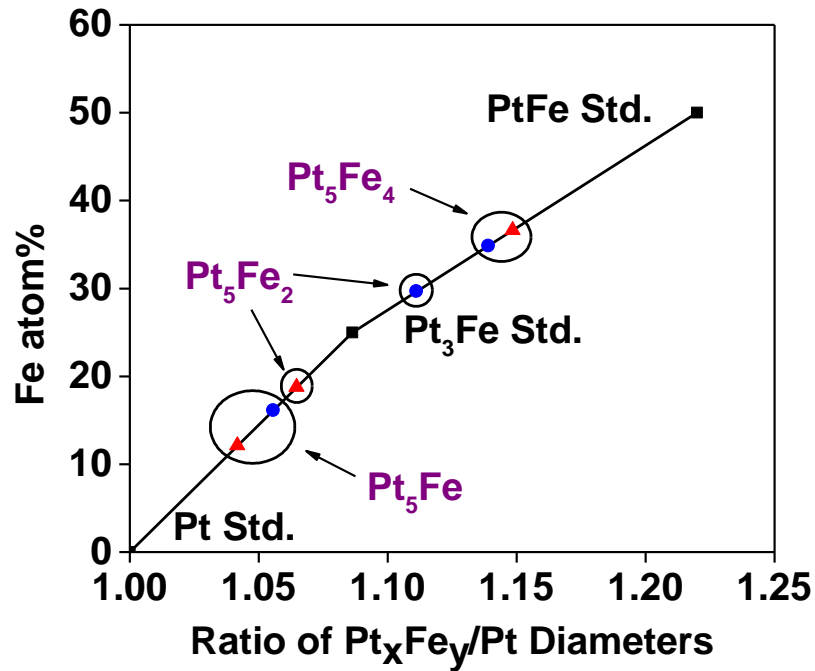


Figure 5. Calculation of the Fe content in $Pt_5Fe_x@mSiO_2$ samples based on particle size increases observed using TEM (▲) and calculated using the Scherrer equation after XRD analysis (●). Actual Fe/Pt ratios are determined using linear interpolation of Pt, Pt_3Fe , and PtFe standards (■).

Table 7. Fe/Pt ratios estimated by changes in particle size that is viewed using TEM.

Sample	Core Diameter (nm) ^a	Shell Thickness (nm)	Ratio of Diameter Increase	Calculated Fe atom% ^b	Estimated Fe/Pt Ratio	Calculated Fe/Pt Ratio ^b
Pt@mSiO ₂	13 ± 2	11 ± 2	-	-	-	-
Pt ₅ Fe@mSiO ₂	14 ± 2	12 ± 3	1.04	12	0.138	0.14/1
Pt ₅ Fe ₂ @mSiO ₂	14 ± 3	10 ± 3	1.06	19	0.231	0.23/1
Pt ₅ Fe ₄ @mSiO ₂	15 ± 1	11 ± 2	1.15	37	0.578	0.58/1

^aAt least 100 particles were counted. ^bCalculated from linear interpolation of the Fe content in the Pt, Pt_3Fe , and PtFe standards present in **Figure 5**.

Table 8. Fe/Pt ratios estimated by changes in crystallite size that is calculated using the Scherrer equation.

Sample	XRD Crystallite Size (nm)	Ratio of Diameter Increase ^a	Calculated Fe atom% ^b	Calculated Fe/Pt Ratio ^b
Pt@mSiO ₂	10.8 ± 0.2	1.00	-	-
Pt ₅ Fe@mSiO ₂	11.4 ± 0.2	1.06	16	0.19/1
Pt ₅ Fe ₂ @mSiO ₂	12.0 ± 0.3	1.11	30	0.42/1
Pt ₅ Fe ₄ @mSiO ₂	12.3 ± 0.2	1.14	35	0.54/1

^aCalculated by dividing the XRD crystallite size of Pt₅Fe_x@mSiO₂ samples by the XRD crystallite size of the Pt@mSiO₂ XRD sample listed in the first row. ^bCalculated from linear interpolation of the Fe content in the Pt, Pt₃Fe, and PtFe standards present in **Figure 5**.

Table 9. Summary of the Fe/Pt ratios corresponding to the Pt₅Fe_x core size increases observed.

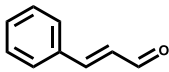
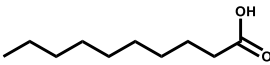
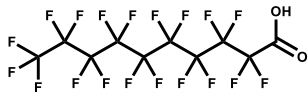
Sample	ICP Estimated Fe/Pt Ratio	TEM Core Size Estimated Fe/Pt Ratio	XRD Crystallite Size Estimated Fe/Pt Ratio (nm)	XRD Phase Suggested Fe/Pt Ratio
Pt@mSiO ₂	-	-	-	-
Pt ₅ Fe@mSiO ₂	(0.23 ± 0.01)/1	0.14/1	0.19/1	0.33/1
Pt ₅ Fe ₂ @mSiO ₂	(0.39 ± 0.04)/1	0.23/1	0.42/1	0.33/1
Pt ₅ Fe ₄ @mSiO ₂	(0.85 ± 0.08)/1	0.58/1	0.54/1	1.00/1

The ICP-MS estimated Fe/Pt content, TEM counted particle size increase, XRD crystallite size trend, and XRD phases observed have Fe content deviations dependent on the analysis method used, as summarized in Table 9. However, every method except the XRD phases observed suggest an increase in Fe content in the core Pt particle that correlates with the amount of Fe(acac)₃ used during the polyol addition Fe to the sample. Several publications discussing Fe modification of Pt particles for enhanced cinnamaldehyde hydrogenation activity and selectivity compare Fe/Pt ratios using ICP techniques, so this correlation of ICP-MS determined Fe/Pt ratios with selectivity and activity enhancement was made in the remainder of this chapter.

Organic Capping Agent and Reactant Accessibility to $Pt_5Fe_x@mSiO_2$ Catalyst Surfaces

In the first part of this chapter, the addition of Fe to the $Pt@mSiO_2$ structure was demonstrated using XRD, ICP-MS, and TEM. For the synthesis of Pt_5Fe_x alloys, it is possible that $Fe(acac)_3$ went through thermal decomposition and deposited on the $mSiO_2$ shell and will only form bimetallic structures after high temperature reduction. In contrast, organic capping agents and reactants must be on the catalyst surface when studying how attached ligands affect the catalytic reaction. Therefore, knowing the porosity and surface area of the $mSiO_2$ shell is important when discussing the organic capping agent and reactant accessibility of the catalytic core. It is also necessary to know the capping agent and reactant dimensions, which are listed in Table 10. The porosity of the $Pt@mSiO_2$, $Pt_5Fe@mSiO_2$, and $Pt_5Fe_2@mSiO_2$ samples after calcination was determined, but if they were reduced and left exposed to air after physisorption measurements their catalytic activity would change over time, possibly because of surface Fe oxidation in air. Therefore, we did not want to reduce a large quantity of catalyst for physisorption measurements, because the difference in the degree of crystal alloying would be unknown when comparing catalysts reduced a single time to catalysts reduced twice.

Table 10 Dimensions of the reactant and ligands used during cinnamaldehyde hydrogenation tests.^a

	Cinnamaldehyde	Decanoic Acid	Perfluorodecanoic Acid
Structure			
Length (nm)	0.876	1.384	1.553
Width (nm)	0.497	0.300	0.388

^aCalculated using Jmol software version 14.2.15.⁵² After drawing the structure, the minimize function was used until the length and width measurements stopped changing.

Static charges on the sample tubes would have resulted in higher percent errors if a small amount of sample was analyzed. Therefore, at least 75 mg of Pt@mSiO₂ and Pt₅Fe_x@mSiO₂ was used for each measurement to reduce the effects of analytical balance induced random error on surface area calculations. To circumvent the problem of having to anneal Pt@mSiO₂ and Pt₅Fe_x@mSiO₂ samples a second time after physisorption measurements to prepare it for catalytic reactions, MCM-41 was used as a model for the porosity of the mSiO₂ shell to examine changes after high temperature reduction conditions.

The results for porosity and surface area changes after high temperature calcination and reduction of the materials is presented in Figure 6. The sample with the smallest pores, MCM-41 calcined at 500 °C and reduced at 700 °C, has a pore size that is 1.4x larger than perfluorodecanoic acid, which is the longest capping agent utilized in this report. This leads us to believe the capping agents and reactant can freely diffuse into the pores of the Pt₅Fe_x@mSiO₂ samples during organic capping agent attachment processes and under reaction conditions. The capping agents are also dissolved in an acetone solution and added to the catalyst particles before introducing the dichloromethane solvent. Consequently, capillary forces should freely pull the ligand into the molecule during capping agent attachment processes. Additionally, the presence of the organic capping agent can affect the hydrophobicity of the support during reactions by making the pores more nonpolar without entirely blocking movement of the molecule. Contrariwise, the area on the surface of the catalyst may be more polar because of the higher concentration of carboxylic acid functionalities. The presence of polar functional groups may orient the C=O group in α,β -unsaturated aldehydes towards the intermetallic

surface, resulting in enhanced selectivity towards the alcohol product. Additionally, the presence of electron withdrawing F in perfluorodecanoic acid may influence the adsorbate bonding energy of C=O and C=C groups, and therefore affect the relative rates of their saturation. This results in an excellent system for studying the ligand effect on the cinnamaldehyde hydrogenation reaction.

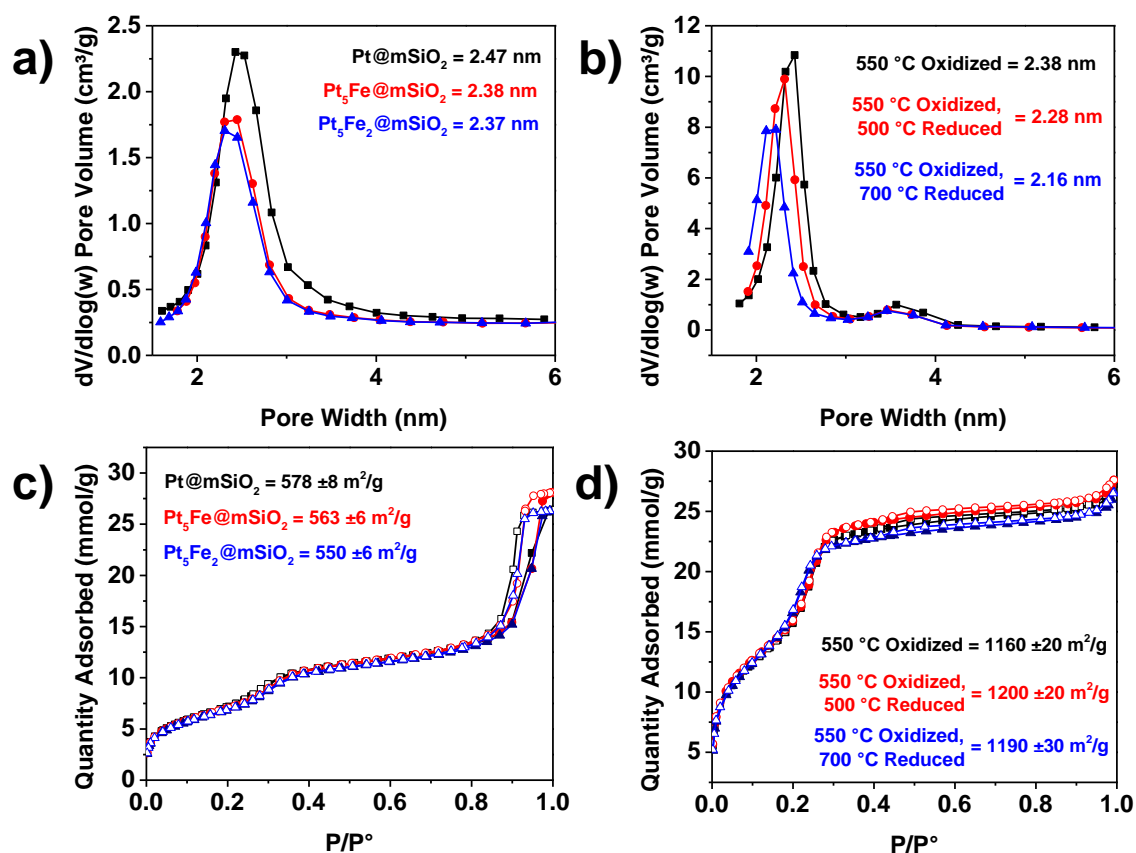


Figure 6. Plots of changes in pore volume with respect to changes in pore diameter (a, b) and BET isotherms (c, d) are displayed with sample average pore sizes and BET surface areas, respectively. a, c) Pt@mSiO₂, Pt₅Fe@mSiO₂, and Pt₅Fe₂@mSiO₂ calcined at 550 °C for 6 hrs. b, d) MCM-41 samples after 550 °C calcination for 6 hrs and, if applicable, temperature at which a 6 hr reduction treatment was completed.

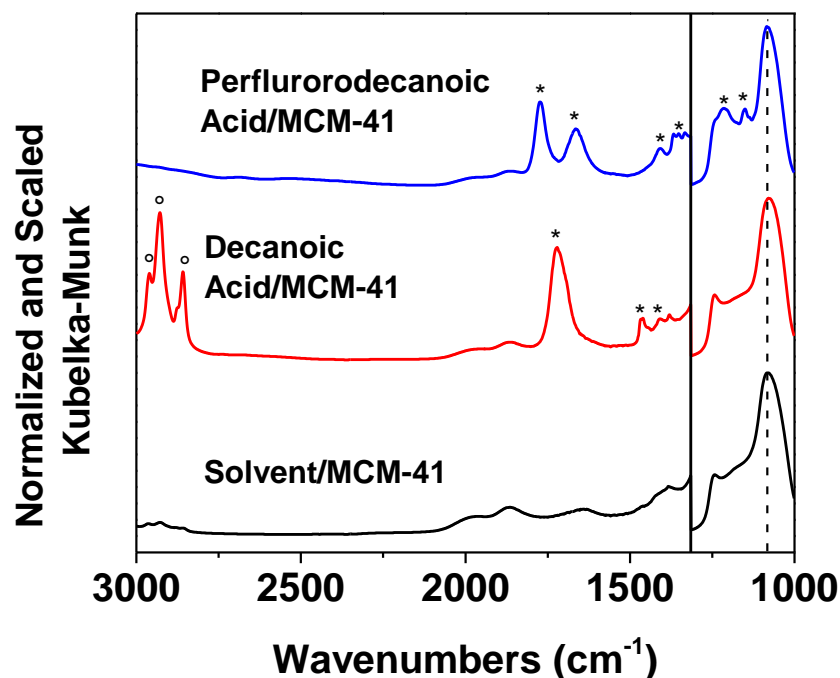


Figure 7. Vibrational spectra of the solvent (acetone and dichloromethane), decanoic acid, or perfluorodecanoic acid loaded onto MCM-41 after the degassing process is completed. Spectra are normalized based on peak located at the dashed line, and the data is further scaled 10x higher in the region from 3000 cm^{-1} to 1315 cm^{-1} .

To further prove the accessibility of the ligands to the catalytic surface and to understand the interaction decanoic and perfluorodecanoic acid have with the catalytic surface, DRIFTS studies were completed. The vibrational spectra of the perfluorodecanoic and decanoic acid molecules after loading them into the pores of MCM-41 can be observed in Figure 7. The results after reducing $\text{Pt}_5\text{Fe@mSiO}_2$ catalysts at $500\text{ }^\circ\text{C}$ for 6 hrs and subjecting them to ligand attachment and washing conditions are provided in Figures 8-10. Here, the observation of new or more intense peaks are listed with asterisks and degree signs, respectively. A full list of assignments of the observed peaks can be observed in Table A1 in the Appendix. The reflectance spectra listed in

Figures 7-12 are normalized to unity based on the peak at 1080 cm^{-1} labelled with the dashed line that corresponds to asymmetric Si-O-Si stretching vibrations. The peaks from 3000 cm^{-1} to 1315 cm^{-1} are furthermore scaled ten times to more easily view changes in peak intensities and shifts in this region and are separated from the non-scaled region by a solid black line.

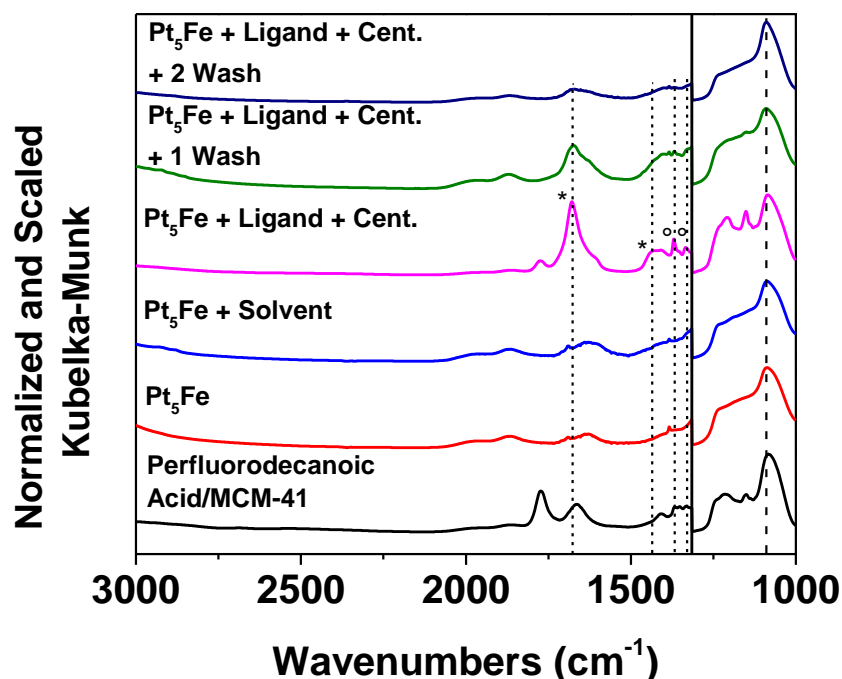


Figure 8. Perfluorodecanoic acid ligand loading and washing experiment. $\text{Pt}_5\text{Fe}@m\text{SiO}_2$ is listed as Pt_5Fe . The solvent consists of acetone and dichloromethane. When “ligand” is present, the ligand was introduced through ligand attachment processes in acetone and dichloromethane. “Cent.” indicates the sample was centrifuged after the ligand attachment process was completed and the supernatant was removed. Washing steps involved dispersing the catalyst in THF, centrifuging, and removing the supernatant. Spectra are normalized based on peak located at the dashed line, and the data is further scaled 10x higher in the region from 3000 cm^{-1} to 1315 cm^{-1} .

The ligand attachment process with only acetone and dichloromethane present was completed on MCM-41 to test if we could reduce the acetone concentration on the support until the sharp carbonyl peak at $\sim 1700\text{ cm}^{-1}$ disappeared. This is necessary to easily observe the shifts or intensity changes in carbonyl peaks characteristic of carboxylic acids in the attached ligands. After flowing He at a rate of 20 mL/min for 30

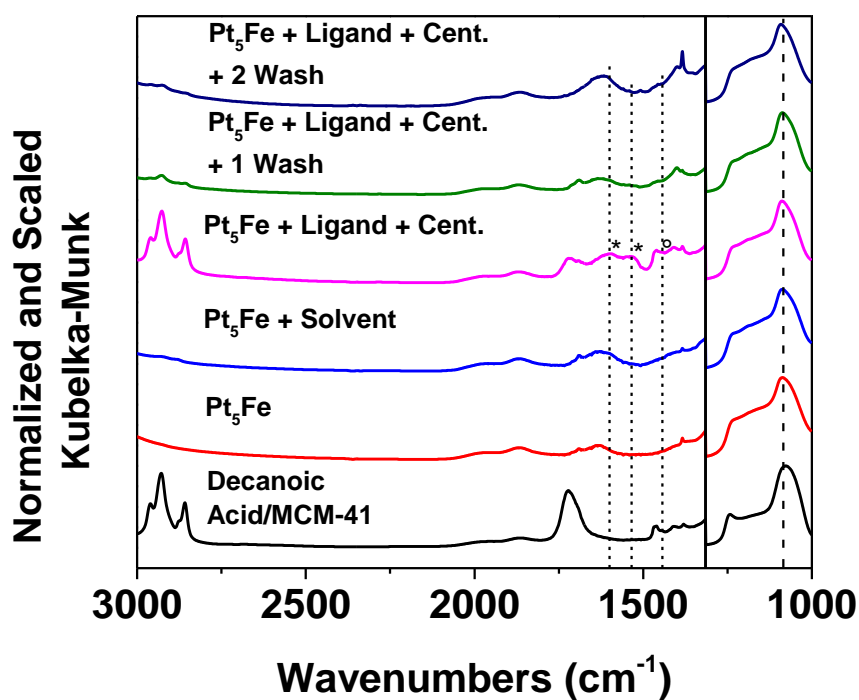


Figure 9. Decanoic acid ligand loading and washing experiment. $\text{Pt}_5\text{Fe}@m\text{SiO}_2$ is listed as Pt_5Fe . The solvent consists of acetone and dichloromethane. When “ligand” is present, the ligand was introduced through ligand attachment processes in acetone and dichloromethane. “Cent.” indicates the sample was centrifuged after the ligand attachment process was completed and the supernatant was removed. Washing steps involved dispersing the catalyst in acetone, centrifuging, and removing the supernatant. Spectra are normalized based on peak located at the dashed line, and the data is further scaled 10x higher in the region from 3000 cm^{-1} to 1315 cm^{-1} .

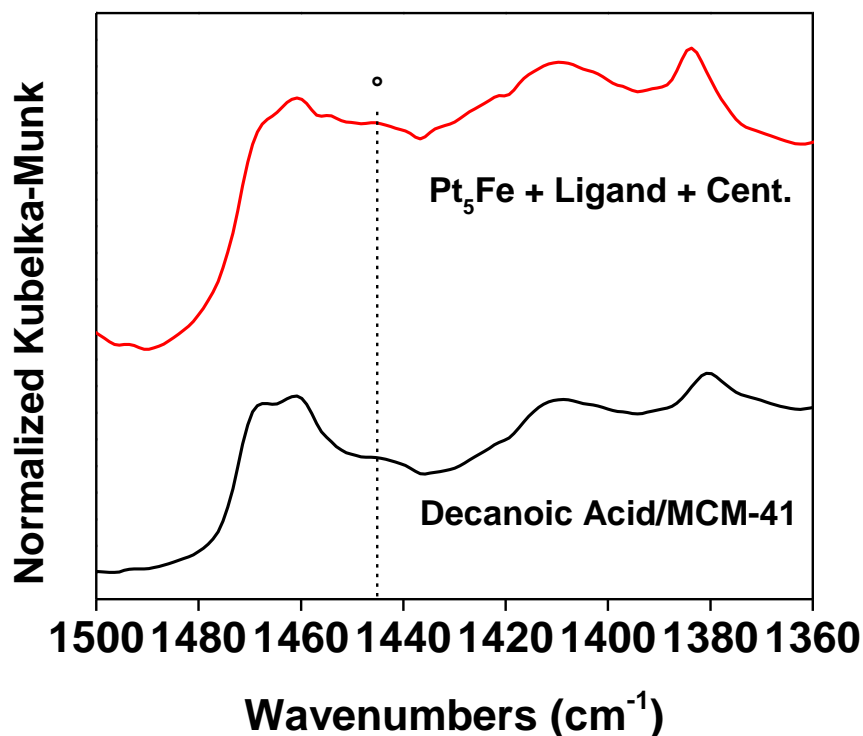


Figure 10. Enlarged image from 1500-1360 cm^{-1} for two spectra present in Figure 9. The change in peak intensities on the dotted line indicate the presence of decanoic acid adsorbed on $\text{Pt}_5\text{Fe@mSiO}_2$.

min through the sample while it is at 70 °C, the carbonyl peak characteristic of acetone at $\sim 1700 \text{ cm}^{-1}$ disappears. The C-H stretching vibrations from 2800-3000 cm^{-1} also are significantly reduced compared to decanoic acid loaded in MCM-41 after the degassing process. This indicates that acetone and dichloromethane can easily be removed to prevent the solvent from interfering with the DRIFTS analysis.

If perfluorodecanoic acid is loaded onto $\text{Pt}_5\text{Fe@mSiO}_2$, as depicted in Figure 8, shifts in C=O stretching vibrations relative to perfluorodecanoic acid loaded on MCM-41 can be observed at 1679 and 1434 cm^{-1} . These peaks have assignments of asymmetric and symmetric $-\text{COO}^-$ stretching vibrations, respectively. They have a $\Delta\tilde{\nu}$ value of 245

cm^{-1} , which corresponds to unidentate ligands bonding with the catalyst surface.

Additional peaks that increase in intensity relative to perfluorodecanoic acid loaded on MCM-41 can be observed at 1371 and 1336 cm^{-1} . These both can be assigned to $-\text{CF}_2$ stretching vibrations.

Another factor that could affect the catalytic reaction was the presence of free ligands, as observed from the peak at 1774 cm^{-1} . Therefore, washing steps with tetrahydrofuran (THF) were performed to remove the free ligand. However, the peak at 1434 cm^{-1} disappears and the peak at 1679 cm^{-1} decreases during this process. As a result, washing steps were avoided to maximize the presence of perfluorodecanoic acid at the catalyst surface. We plan on completing a control experiment in the future with only ligands and cinnamaldehyde present in solution to evaluate the effects of free ligands on the reaction.

Similar experiments were performed after loading decanoic acid onto $\text{Pt}_5\text{Fe@mSiO}_2$ surfaces, as seen in Figure 9. In this case, new peaks are observed at 1596 and 1445 cm^{-1} that can be respectively assigned to asymmetric and symmetric stretching vibrations of surface bound decanoic acid. Figure 10 is an enlarged region for comparison between decanoic acid adsorbed on $\text{Pt}_5\text{Fe@mSiO}_2$ surfaces and MCM-41 surfaces that shows the peak intensity changes when decanoic acid interacts with the catalyst surface. These peaks have a $\Delta\tilde{\nu}$ value of 151 cm^{-1} and can be assigned to bridging type bonding of decanoic acid with the surface of the catalyst. Additional peaks can be observed at 1533 cm^{-1} and are assigned to $-\text{CH}_2$ vibrations.

Additional catalyst washing studies were completed to see if free decanoic acid could be removed without losing decanoic acid adsorbed on the catalyst surface by

tracking the disappearance of the C=O peak at 1722 cm^{-1} . After washing the sample with acetone the peak disappears, but the adsorbed decanoic acid peaks at 1596, 1533, and 1445 cm^{-1} likewise disappear. Washing steps were also avoided for decanoic acid treated catalysts during cinnamaldehyde hydrogenation because of these results.

It was also anticipated that Pt surfaces would not have a strong affinity towards carboxylic acid groups, because FTIR studies of oleic acid protected Pt synthesized by Vu and coworkers show no peaks for organic groups bonding to the catalyst surface. Additionally, a previous study shows carboxylic acid is more prone to binding to Fe and thiol will bind to Pt when both functionalities are present over Pt-Fe surfaces.³⁸

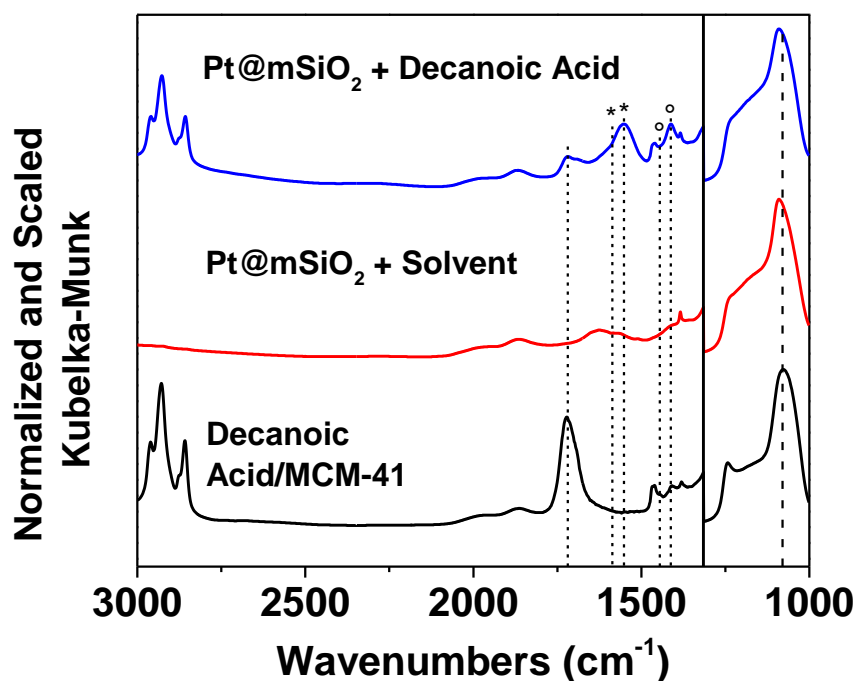


Figure 11. Decanoic acid modified Pt@mSiO₂ catalyst exhibiting shifted peaks and more intense peaks relative to other controls tested. Spectra are normalized based on peak located at the dashed line, and the data is further scaled 10x higher in the region from 3000 cm^{-1} to 1315 cm^{-1} .

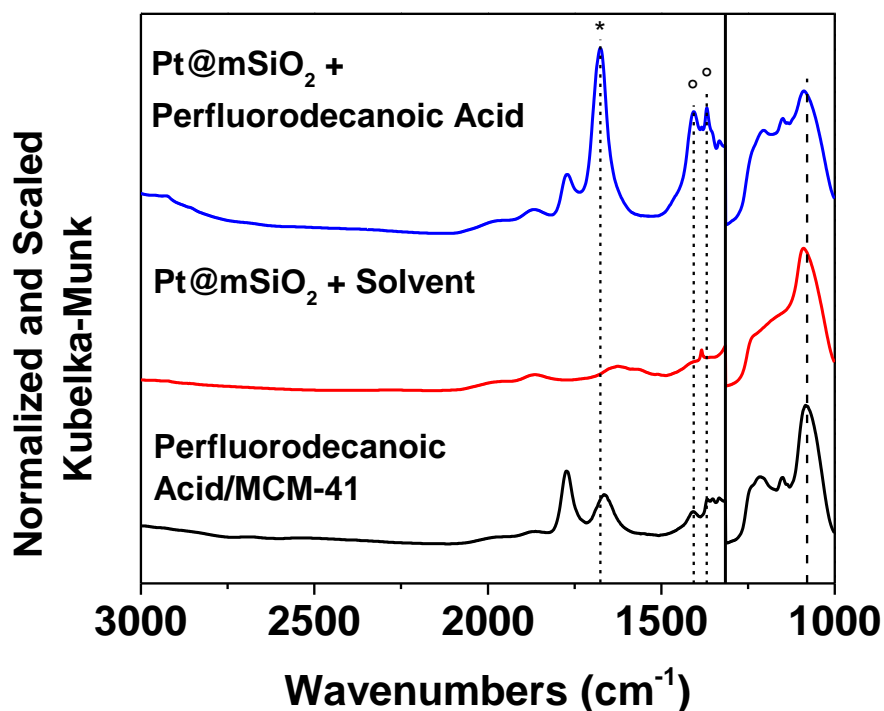


Figure 12. Perfluorodecanoic acid modified Pt@mSiO₂ catalyst exhibiting shifted peaks and more intense peaks relative to other controls analyzed. Spectra are normalized based on peak located at the dashed line, and the data is further scaled 10x higher in the region from 3000 cm⁻¹ to 1315 cm⁻¹.

However, carboxylic acid containing ligands have been used for shape controlled syntheses of Pt in the past,⁵³ therefore we collected FTIR spectra to determine how our Pt interacts with carboxylic acid containing capping agents. After completing DRIFTS studies of decanoic (Figure 11) and perfluorodecanoic (Figure 12) acid treated Pt@mSiO₂, we observed new peaks that are not present over Pt@mSiO₂ mixed with solvent or after adsorbing either decanoic or perfluorodecanoic acid onto MCM-41. The ligand-Pt interactions are therefore present, and major changes in activity and selectivity

may result from Fe presence on the catalyst surface when comparing Pt to its ligand-free or ligand-capped Pt₅Fe or Pt₅Fe₂ counterpart.

Understanding Pt₅Fe_x@mSiO₂ as a Cinnamaldehyde Hydrogenation Catalyst

Selective hydrogenation of cinnamaldehyde was subsequently tested over Pt@mSiO₂, Pt₅Fe@mSiO₂, and Pt₅Fe₂@mSiO₂ catalysts reduced at 300, 500, or 700 °C and treated with perfluorodecanoic acid, decanoic acid, or no capping agent, as listed in Table 11. Detailed reaction conditions are listed in the Materials and Methods section of this chapter. The calculation for conversion is as follows:

$$\text{Conv.} = (HCAL+HCOL+COL)/(CAL+HCAL+HCOL+COL) \times 100\% \quad (5)$$

where CAL, HCAL, HCOL, and COL are the moles of cinnamaldehyde, hydrocinnamaldehyde, hydrocinnamyl alcohol, and cinnamyl alcohol present after the reaction is complete, respectively. The selectivity towards cinnamyl alcohol was calculated using the following equations:

$$\text{Selectivity} = COL/(HCAL+HCOL+COL) \times 100\% \quad (6)$$

To calculate selectivity for HCAL or HCOL, the moles of these products are switched with the COL content in the numerator. Calculating the activity of catalysts allows for conversion comparisons based on the total catalytic metal present, and it is useful for comparing results from different catalysts that are used for the same reaction. The total amount of Pt present in Pt@mSiO₂, Pt₅Fe@mSiO₂, and Pt₅Fe₂@mSiO₂ was calculated using ICP-MS, and the amount of COL, HCAL, and HCOL synthesized after reaction was determined using GC. The activity was then calculated using the following equation:

$$\text{Activity} = (HCAL+HCOL+COL)/(\text{moles of Pt}) \quad (7)$$

Table 11. Dependence of cinnamaldehyde hydrogenation results on the nature of ligand modified Pt@mSiO₂, Pt₅Fe@mSiO₂, and Pt₅Fe₂@mSiO₂ surfaces.^a

Catalyst	Heat Treatment (°C)	Acid ^b	Conversion (%)	Selectivity (%)			Activity ^d	TON ^d
				COL ^c	HCAL ^c	HCOL ^c		
Pt@mSiO ₂	300	N	6.6	35.7	51.6	12.7	2	20
Pt ₅ Fe@mSiO ₂	300	N	22.1	84.2	15.4	0.4	7	87
Pt ₅ Fe ₂ @mSiO ₂	300	N	43.3	76.3	17.4	6.3	13	190
Pt@mSiO ₂	300	D	6.0	31.6	67.2	1.1	2	18
Pt ₅ Fe@mSiO ₂	300	D	4.1	86.6	8.2	5.2	1	16
Pt ₅ Fe ₂ @mSiO ₂	300	D	47.4	83.3	11.8	4.9	15	207
Pt@mSiO ₂	300	P	6.5	45.0	53.7	1.3	2	19
Pt ₅ Fe@mSiO ₂	300	P	70.4	72.1	12.4	15.5	24	284
Pt ₅ Fe ₂ @mSiO ₂	300	P	77.7	68.2	13.8	18.0	24	343
Pt@mSiO ₂	500	N	18.6	30.6	46.4	23.0	6	55
Pt ₅ Fe@mSiO ₂	500	N	1.7	73.6	11.3	15.1	1	7
Pt ₅ Fe ₂ @mSiO ₂	500	N	16.8	89.4	9.5	1.1	5	72
Pt@mSiO ₂	500	D	7.4	13.0	56.8	30.2	2	22
Pt ₅ Fe@mSiO ₂	500	D	24.8	89.4	10.0	0.6	8	96
Pt ₅ Fe ₂ @mSiO ₂	500	D	42.3	87.8	8.0	4.2	13	185
Pt@mSiO ₂	500	P	5.4	15.6	57.4	27.0	2	16
Pt ₅ Fe@mSiO ₂	500	P	90.1	77.2	3.2	19.5	29	353
Pt ₅ Fe ₂ @mSiO ₂	500	P	18.8	76.7	17.8	5.5	6	82
Pt@mSiO ₂	700	N	8.3	38.8	48.2	13.0	3	25
Pt ₅ Fe@mSiO ₂	700	N	69.2	92.4	3.8	3.8	23	275
Pt ₅ Fe ₂ @mSiO ₂	700	N	27.2	91.9	7.4	0.8	8	116
Pt@mSiO ₂	700	D	5.6	63.0	33.7	3.2	2	16
Pt ₅ Fe@mSiO ₂	700	D	46.4	86.5	8.4	5.1	15	180
Pt ₅ Fe ₂ @mSiO ₂	700	D	6.4	90.3	4.1	5.6	2	27
Pt@mSiO ₂	700	P	2.6	52.4	29.2	18.5	1	8
Pt ₅ Fe@mSiO ₂	700	P	48.3	91.4	4.5	4.2	16	188
Pt ₅ Fe ₂ @mSiO ₂	700	P	18.2	87.4	10.7	2.0	6	78

^aSubstrate/bulk metal ratio is 32. The dispersion of Pt was calculated to be 9.9% and the substrate/surface metal ratio is 324. ^bNo ligand (N), Decanoic acid (D), and Perfluorodecanoic acid (P). ^cCinnamyl alcohol (COL), hydrocinnamaldehyde (HCAL), and hydrocinnamyl alcohol (HCOL). ^dActivity and turnover number (TON) were calculated based on bulk Pt and surface Pt, respectively.

Turnover number (TON) calculations allow for the comparison of the amount of reactant consumed because of interactions with catalytic metals only in the surface of catalysts, and they are more useful for comparing results between fundamental studies. The

turnover number normalizes the activity of catalysts for comparisons between nanoparticles of different sizes and geometries. The following equation can be used to estimate TON:

$$\text{TON} = (\text{HCAL} + \text{HCOL} + \text{COL}) / (\text{moles of surface Pt}) \quad (8)$$

In our study, the amount of Pt in the surface was estimated using the method reported by Van Hardeveld and Hartog.⁵⁴ The diameter of the particles was estimated using TEM. We used a cubo-octahedron model for particles covered with (111) planes and a Pt-Pt distance of 0.2775 nm for the calculation. Since some Pt was replaced with Fe in this approximation, the surface atom percentage was then multiplied by 5/6 or 5/7 to obtain the surface Pt percentage for Pt₅Fe@mSiO₂ and Pt₅Fe₂@mSiO₂, respectively.

There are a few trends that can be observed when reviewing the data. Pt@mSiO₂ catalysts have lower cinnamyl alcohol selectivity compared to all other catalysts that contain added Fe. Pt@mSiO₂ catalysts also are not affected by the addition of decanoic or perfluorodecanoic acid as much as Pt₅Fe@mSiO₂ or Pt₅Fe₂@mSiO₂ are. We show in Figures 11-12 that carboxylic acid groups bond to Pt in our system, therefore, the ligand adsorption to a Pt surface does not influence the cinnamaldehyde adsorption energy enough to cause a large change in conversion or cinnamyl alcohol selectivity. Changes in cinnamaldehyde conversion are not as significant when comparing additions of capping agents on Pt surfaces to additions of capping agents to Pt₅Fe and Pt₅Fe₂ surfaces. Therefore, the presence of both a capping agent and Fe must play a vital role in enhancing the activity.

Pt₅Fe@mSiO₂ reduced at 500 °C and Pt₅Fe₂@mSiO₂ reduced at 300 °C tend to have increasing conversion with increasing capping agent hydrophobicity, which is in

agreement with Vu *et al.*'s results.² However, the cinnamyl alcohol selectivity of the reaction does not notably change when ligands are adsorbed to the surface. This is in agreement with other publications that discuss the enhancement in selectivity from added Fe and ascribe the enhancement to geometric and electronic modifications in the bulk and the surface.^{39, 55}

An additional trend to note is that Pt₅Fe@mSiO₂ and Pt₅Fe₂@mSiO₂ reduced at 700 °C and protected with perfluorodecanoic acid also have lower conversion and higher cinnamyl alcohol selectivity relative to their 300 °C and 500 °C reduced counterparts. It has been reported that the placement of Pt inside metal-organic frameworks (MOFs) induces more steric hindrance during cinnamaldehyde hydrogenation compared to the placement of particles on MOF surfaces.⁵⁶ This constraint forces cinnamaldehyde to interact with C=O groups perpendicular to Pt surfaces and prevents C=C bonds from interacting with the surface and becoming hydrogenated. Therefore, the enhancement in cinnamyl alcohol selectivity may result from decreases in pore size of the mSiO₂ shell inducing steric hindrance as modelled by the 700 °C reduced MCM-41 used for physisorption tests displayed in Figure 6. Additionally, treating silica at high temperatures has been shown to reduce its hydrophilicity.⁵⁷ Durndell and coworkers have shown that Pt supported on hydrophilic supports, such as SBA-15, have higher activity for cinnamaldehyde conversion than relatively hydrophobic fumed silica.⁵⁸ The reduction in conversion at higher temperatures might be attributable to the removal of Si-O-H groups from the channel walls and the loss of interactions between Si-O-H and polar cinnamaldehyde during reactions. If this is true, then the arene ring of cinnamaldehyde travels next to the nonpolar capping agent tail, whereas the carbonyl group is in contact

with the polar SiO₂ walls, and a balance between hydrophobicity and hydrophilicity is required for cinnamaldehyde to access the catalyst surface.

Surface studies were also conducted to understand how Pt and Fe ratios and oxidation states influence the catalytic results observed (Figure 13). Pt₅Fe@mSiO₂ was observed to have the best activity and cinnamyl alcohol selectivity,

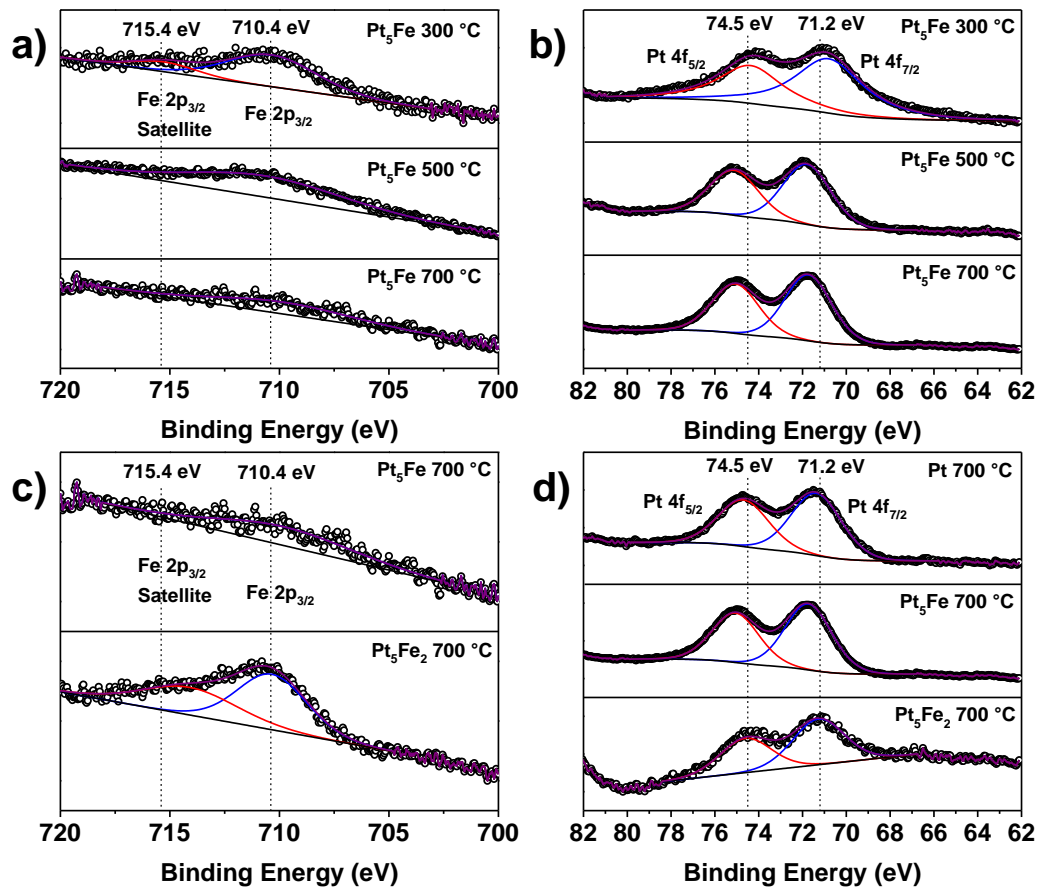


Figure 13. XPS spectra after calcining Pt@mSiO₂ and Pt₅Fe_x@mSiO₂ samples at 550 °C for 6 hrs and reducing them at 300, 500, or 700 °C for 6 hrs. a,b) XPS spectra of the Fe 2p_{3/2} and Pt 4f electrons, respectively, as a function of reduction temperature. c,d) XPS spectra of Fe 2p_{3/2} and Pt 4f electrons, respectively, as a function of increasing Fe content.

Table 12. Pt 4f_{7/2} and Fe 2p_{3/2} electron binding energies and element surface ratios in Pt₅Fe_x@mSiO₂ samples.

Sample	Pt 4f _{7/2} B.E. (eV)	Fe 2p _{3/2} B.E. (eV)	Fe 2p _{3/2} Satellite B.E. (eV)	Fe/Pt Ratio	Conversion (%)	COL Selectivity (%)
Pt 700 °C	71.1	-	-	-	8.3	38.8
Pt ₅ Fe 300 °C	71.3	710.6	715.5	0.55/1	22.1	84.2
Pt ₅ Fe 500 °C	71.4	710.3	-	1.29/1	1.7	73.6
Pt ₅ Fe 700 °C	71.3	710.1	-	0.22/1	69.2	92.4
Pt ₅ Fe ₂ 700 °C	71.5	711.1	715.4	4.37/1	27.2	91.9

therefore its X-ray photoelectron emission spectra were collected after treating it at different reduction temperatures. Complete lists of experimentally observed binding energies and reference binding energies are listed in Table A2 and Table A3 in the Appendix, respectively. It is expected that the Fe concentration on the surface decreases with increasing reduction temperature, because high temperatures are typically required to reduce and anneal iron oxides even in the presence of Pt,⁵⁹ which can readily adsorb and dissociate H₂.³² As anticipated, the observed peaks for Fe in Figure 13a decrease in intensity when the reduction temperature increases. However, as seen in Table 12, the Fe/Pt surface ratio increases when comparing the samples reduced at 300 °C and 500 °C. This could occur if small Fe₂O₃ clusters that nucleate on the mSiO₂ shell during the synthesis migrate and form a surface alloy with Pt at temperatures between 300 °C and 500 °C. To test this possibility, a TEM image after the synthesis of Pt₅Fe₄@mSiO₂ was collected as depicted in Figure 14. New clusters cannot easily be observed after the polyol addition of Fe, however, particles less than 1 nm cannot be resolved in TEM, so the presence of iron oxide clusters remains a possibility.

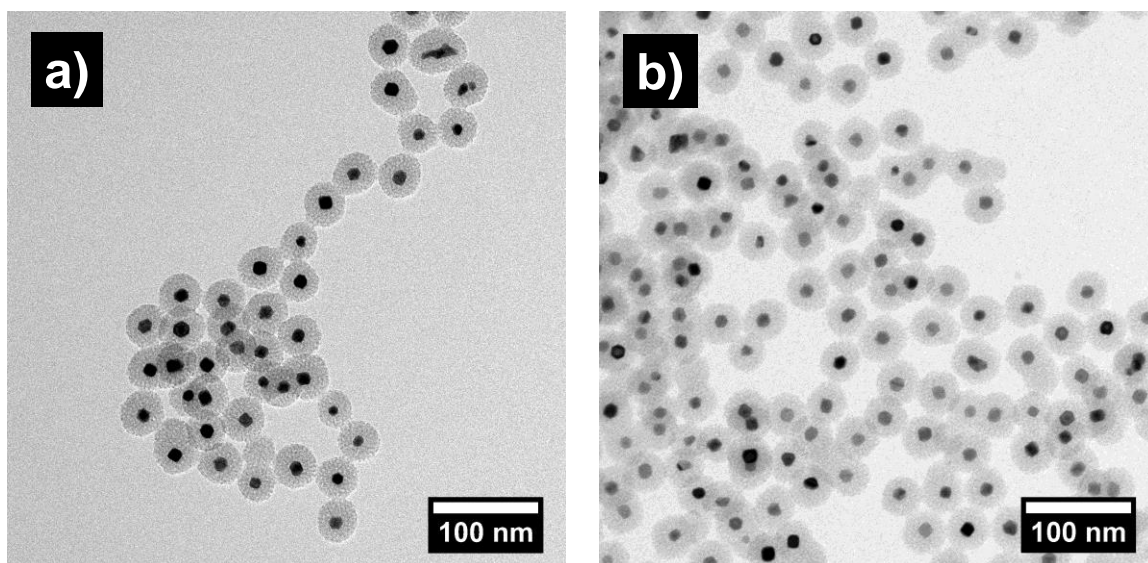


Figure 14. a) Pt@mSiO₂ used to synthesize b) Pt₅Fe₄@mSiO₂ at 200 °C. This image is after washing with acetone 3x.

Fe XPS spectra are typically complicated by the paramagnetic state of unpaired electrons. When an unpaired electron remains after the ejection of an s-type electron, it can couple with unpaired electrons in other orbitals. This creates an ion with several possible final state configurations and final energies and is observed as several small multiplet peaks with small shifts in binding energy forming a single broad peak in XPS spectra.⁶⁰ Additionally, when an electron is ejected from Fe present in the +2 or +3 oxidation states, some of the kinetic energy transfers to other electrons and moves them to an orbital with more energy. As a result, the ejected electron has a lower kinetic energy and is thus observed as having a higher binding energy. In this case, satellite peaks called shake up peaks are formed in addition to the main peaks observed for oxidized Fe.⁶⁰

All samples were exposed to air for 5-10 min during XPS sample preparation, which explains why the observed broad peak for Fe at all three reduction temperatures

contains characteristics of FeO, FeOOH, and Fe₂O₃ multiplet splitting peaks that form over a range of binding energies. Considering the rate at which Fe reacts with oxygen, contact with air likely removed all zerovalent Fe that was on the surface. It is possible that the sample mainly consists of FeO because the broad red peak at 715.4 – 715.5 eV is located in the characteristic position of Fe²⁺ satellite peaks. This XPS data also accurately represents the nanoparticle surfaces when preparing them for catalytic experiments because the samples are exposed to air briefly before completing the ligand attachment process.

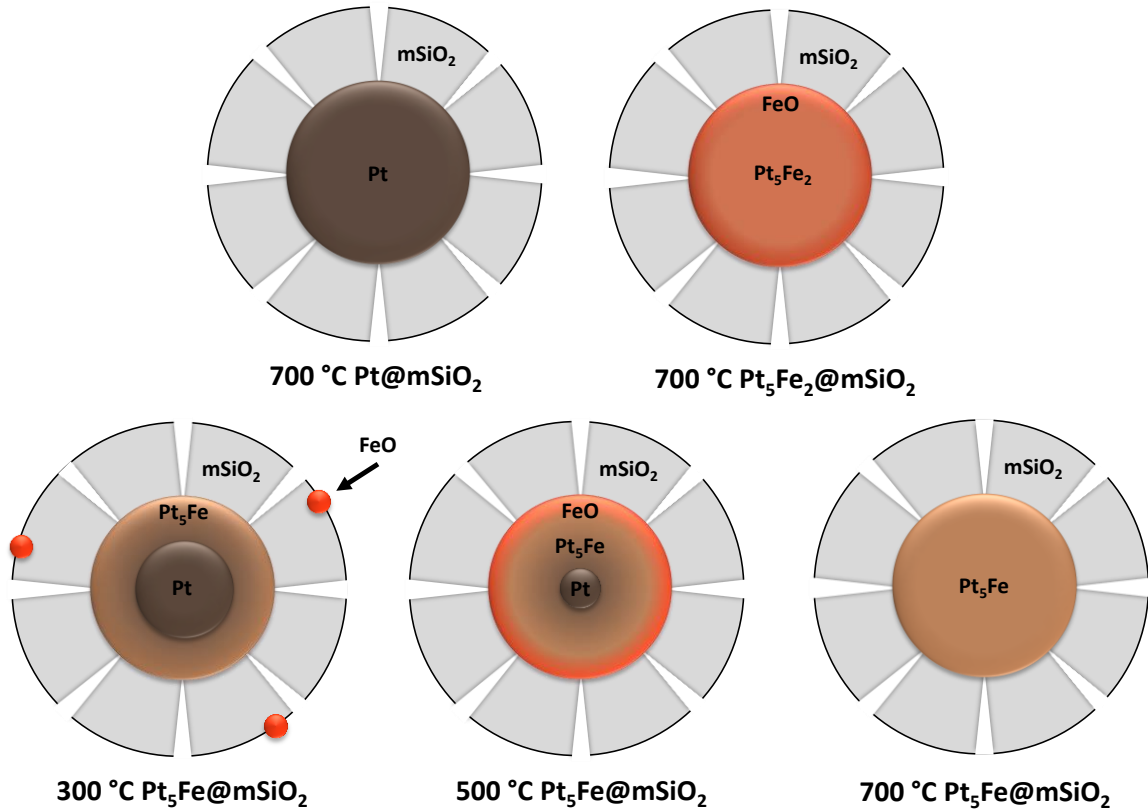
There does not seem to be a correlation between the Fe binding energy and the conversion and cinnamyl alcohol selectivity observed in these samples. There are trends present in Fe binding energy that correlate with the Fe/Pt composition and reduction temperature used, where lower reduction temperatures and higher Fe content result in higher Fe binding energies. This indicates that samples with higher Fe content and lower reduction temperatures have a higher ratio of oxidized/zerovalent Fe. However, the accuracy of the binding energies of the Pt₅Fe@mSiO₂ samples reduced at 500 and 700 °C is significantly affected by the reduction in signal intensity, which limits our understanding of the system.

It is also important to study Pt oxidation states to comprehend their effects on the reaction. As depicted in the Pt XPS spectrum in Figure 13b, the Pt₅Fe sample reduced at 300 °C has a larger full width at half maximum (FWHM) relative to the Pt peaks in other samples. This can be attributed to charging effects caused by the mSiO₂ and iron oxides present in the sample insulating the electron transfer between the metal core and the spectrometer.⁶¹ Charging effects cause all elements in the samples to have a net positive

charge during analysis, but the amount of charging is not homogeneous across the sample resulting in peak broadening.

The Pt binding energy in $\text{Pt}_5\text{Fe}@m\text{SiO}_2$ in Figure 13b is mainly closer to the range for zerovalent Pt compared to Pt-Si, Pt-oxide, and $\text{Pt}(\text{OH})_2$ bonds. This indicates that Pt in this sample does not have a very strong interaction with the $m\text{SiO}_2$ shell or iron oxide on the surface and is present in its reduced state. After annealing the sample at higher temperatures, the Pt binding energy remains constant, whereas the Fe binding energy decreases. The Fe/Pt ratio first increases, then decreases. As previously mentioned, this situation is possible if Fe nucleates on both the Pt surface and the outside of the SiO_2 shell. An image of what the structure might look like after different reduction treatments is visible in Scheme 2. Low reduction temperatures would only result in annealing of the Pt and Fe near the surface, causing surface Pt to have a binding energy corresponding to close interactions with Fe, whereas Pt near the center of the core would have a binding energy closer to zerovalent Pt. On the other hand, the Fe binding energy would decrease if it moves from the shell to the core during high temperature reduction treatments because of the change from iron oxides to zerovalent Fe. The Pt binding energy would also remain unchanged if the Fe concentration in Pt remained constant during this process. When the highest temperature is utilized in $\text{Pt}_5\text{Fe}@m\text{SiO}_2$ samples, the Fe/Pt ratio is also close to the Fe/Pt ratio determined with ICP-MS, therefore, the structure is uniform.

The XPS Pt emission spectra in Figure 13c and 13d show the results when changing the Fe content in $\text{Pt}_5\text{Fe}_x@m\text{SiO}_2$ samples reduced at 700 °C. Fe composition was studied at this temperature because selectivity to cinnamyl alcohol was higher on



Scheme 2. Diffusion of iron oxides into the Pt core after high temperature reduction treatments.

average compared to the 300 and 500 °C reduced samples. When comparing the Pt@mSiO₂ and Pt₅Fe_x@mSiO₂ samples, the Pt 4f_{7/2} electron binding energy shifts to higher energies as more Fe is added, likely because there is an increased Fe concentration on the surface that withdraws more electrons from Pt.⁶² The belief that there is a higher concentration of Fe on the surface relative to the bulk is supported by the relatively high Fe/Pt ratio on the surface in the 700 °C reduced Pt₅Fe₂@mSiO₂ sample observed through XPS studies and the lower activity observed in the Pt₅Fe₂@mSiO₂ relative to the 700 °C reduced Pt₅Fe@mSiO₂ sample. The increase in conversion in Pt₅Fe@mSiO₂ relative to Pt@mSiO₂ and Pt₅Fe₂@mSiO₂ is an indication that there is an ideal electron density

around Pt required for cinnamaldehyde hydrogenation, because Pt 4f_{7/2} electrons in Pt₅Fe@mSiO₂ have an intermediate binding energy relative to Pt 4f_{7/2} electrons in the other two samples. This is in agreement with the catalysis and XPS results reported by Mahata and coworkers³⁹ listed in Table 2, because they observed an increase in conversion at Pt 4f_{7/2} electron binding energies closer to the binding energies observed in our study. However, there are many differences between our system and theirs that could affect the comparison, such as Pt⁰/Pt²⁺ ratio and metal-support interactions.

Conclusions

Claims of enhanced cinnamaldehyde conversion towards cinnamyl alcohol in the presence of Fe, a capping agent, or both were elucidated throughout the discussion of our system. A mesoporous silica encapsulated Pt system was demonstrated as a thermally stable and porous starting material suitable for the addition of Fe that was utilized to understand the effects of capping agent addition, high temperature reduction, and base metal content on cinnamaldehyde hydrogenation over Pt₅Fe_x@mSiO₂ catalysts. We have demonstrated that decomposition of acetylacetonate precursors over Pt@mSiO₂ is an effective method to create intermetallic compounds. The successful addition of Fe to the system was validated using XRD, TEM, and ICP-MS, however, the yield of atomic Fe after reducing the samples was not 100%.

The attachment of ligands to the surface of Pt₅Fe@mSiO₂ and Pt@mSiO₂ was possible because of the presence of pores with diameters greater than 2 nm and proven through -COO⁻ frequency shifts upon capping agent adsorption. Cinnamaldehyde hydrogenation over ligand modified Pt₅Fe surfaces resulted in enhanced conversion

relative to ligand free surfaces, likely because of both the hydrophobic conditions induced and the presence of Fe modifying the adsorption energy of C=O bonds to the catalyst surface. This was observed over only the Pt₅Fe₂@mSiO₂ reduced at 300 °C and Pt₅Fe@mSiO₂ reduced at 500 °C. Higher reduction treatments might have increased the amount of Fe on the Pt₅Fe₂ surface and blocked active sites. The Pt₅Fe surface might have lacked enough Fe when lower reduction temperatures were used, and the differing electronic and geometric structure of the catalyst might have resulted in different trends. Additionally, when a 700 °C reduction temperature was used, the SiO₂ surface becomes more hydrophobic, which prevents the polar C=O tail from having an affinity towards a polar area in the mSiO₂ pores and reduces diffusion rates towards the core. On the other hand, cinnamyl alcohol selectivity was observed to increase mainly upon addition of Fe to the catalysts, but was further enhanced by utilizing higher reduction temperatures. The porosity of the silica shell can change during high temperature treatment and create steric hindrance induced cinnamyl alcohol selectivity. Overall, it is apparent that cinnamyl alcohol selectivity can be enhanced through addition of Fe, but enhancements in conversion are less predictable and can be affected by a variety of changes, including reduction temperature, ligand hydrophobicity, support hydrophobicity, and Fe/Pt ratios.

Materials and Methods

Materials. Decanoic acid (99%), HF (48-51% in H₂O), K₂PtCl₄ (46-47% Pt), mesitylene (99%), and perfluorodecalin (mix of cis and trans, 95%) were purchased from Acros Organics. NaBH₄ (98%), perfluorodecanoic acid (97%), tetraethylene glycol, and trans-cinnamaldehyde (98%) were purchased from Alfa Aesar. NaOH (99.0 – 100%) was

purchased from EMD. Tetrahydrofuran (contains 0.025% butylated hydroxytoluene), acetone (HPLC grade), acetone (Optima purity), CH_2Cl_2 (Optima purity), HCl (trace metal grade, 34 – 37%), HNO_3 (67-70%), methanol (ACS grade), and toluene (ACS grade) were purchased from Fisher Scientific. $\text{Fe}(\text{acac})_3$ was purchased from Lancaster Synthesis Ltd. Hexanes (95% n-hexane) was purchased from Macron. Ar (99.995%) and H_2 (99.99%) were purchased from Matheson. Oleylamine (Technical grade, 70%), tetradecyltrimethylammonium bromide ($\geq 99\%$), and tetraethyl orthosilicate (TEOS, reagent grade, 98%) were purchased from Sigma Aldrich. 3-phenyl-1-propanol (hydrocinnamyl alcohol, $\geq 98.0\%$), 3-phenylpropionaldehyde (hydrocinnamaldehyde, $\geq 90\%$), and cinnamyl alcohol ($\geq 97.0\%$) were purchased from TCI. Materials were used as received. A Millipore Milli-Q Plus was used to make the $18.2 \text{ M}\Omega \cdot \text{cm}$ ultrapure water.

Preliminary Reduction of Fe Precursors in Organic Solvents. In a 25 mL round bottom flask, 15 mL of TEG or oleylamine, 1.0×10^{-4} mol of Fe precursor, and 1 mL of solvent used to dissolve the precursor was added. The sample was then degassed at $100 \text{ }^\circ\text{C}$ under vacuum to remove the solvent used to dissolve the precursor for 1 hr while stirring. Ar was added to the sample and an Ar balloon was attached. The samples were heated to the boiling point of the solvent and observations were made approximately every $10 \text{ }^\circ\text{C}$. For samples that were transparent after the reaction, the TEG or oleylamine was mixed with 30 mL of acetone and centrifuged at 14,000 rpm for 15 min at $30 \text{ }^\circ\text{C}$ to confirm the absence of nucleated particles.

Synthesis of Pt Nanoparticles. The synthesis and coating of Pt particles was completed following a reported procedure.⁴⁴ In a 125 mL Erlenmeyer flask, 8.4 mg of tetradecyltrimethylammonium bromide (TTAB) was dissolved in 60 mL of ultrapure

water using sonication. In a 500 mL round bottom flask, 100 mg of K_2PtCl_4 was dissolved in 25 mL of ultrapure water. The TTAB solution was then poured into the K_2PtCl_4 solution while stirring and 150 mL of ultrapure water was added. The cloudy white solution was then heated with stirring at 750 rpm at 50 °C until the flask became transparent. Next, 285 mg of $NaBH_4$ was dissolved in 15 mL of ice cold water and immediately injected into the flask. A needle was inserted in the septum on the flask to relieve H_2 pressure for 20 min. The sample was stirred at 50 °C for 24 hrs. To remove larger Pt nanoparticles, the samples were distributed to 8 centrifuge tubes, then centrifuged at 3000 rpm for 30 min at 30 °C. Afterwards, the top layer was transferred to new centrifuge tubes. The purification process was repeated three more times.

Coating the Pt nanoparticles with Silica (Pt@SiO₂). The Pt was centrifuged at 12,000 rpm for 30 min at 30 °C. All but 1 mL of supernatant in each centrifuge tube was removed. The Pt nanoparticles were diluted with 192 mL of ultrapure water, transferred to a 500 mL round bottom flask, and sonicated for 10 seconds. While stirring at 600 rpm, 8 mL of 0.05 M NaOH was added to the round bottom flask and the sample was stirred for 10 min. Next, 3 mL of a 10 vol% tetraethyl orthosilicate (TEOS) in methanol solution was added dropwise to the solution over the course of 5 min. The sample was stirred at room temperature for 36 hrs and then centrifuged at 12,000 rpm for 30 min at 30 °C. The supernatant was removed and the sample was dispersed in 20 mL of deionized water.

TTAB Removal through Methanol Reflux (Pt@mSiO₂). The Pt nanoparticles were transferred to a 500 mL round bottom flask and diluted with 180 mL of methanol. Next, 15 mL of concentrated HCl was slowly added while swirling the flask to mix the solution. A large condenser with running water was attached and the sample was heated

with stirring at 90 °C overnight. After cooling to room temperature, the round bottom flask was removed from the condenser and the sample was centrifuged at 12,000 rpm for 30 min at 30 °C. The sample was washed with 20 mL of acetone 2x, then diluted to 40 mL with acetone and the exact amount of Pt in the batch was determined using ICP-MS.

Addition of Fe to Pt@mSiO₂ (Pt₅Fe_x@mSiO₂). In a typical synthesis, 3 batches of Pt@mSiO₂ centrifuged at 12,000 rpm for 30 min at 30 °C and a minimal amount of Optima purity acetone was used to transfer the samples to a 2-neck 250 mL round bottom flask. Fe(acac)₃ was added to a 5 mL vial and diluted to 15 mL/mg using acetone. The Fe(acac)₃/Pt ratios used during the synthesis were 1/3 and 1/2 for Pt₅Fe@mSiO₂ and Pt₅Fe₂@mSiO₂, respectively. The appropriate Fe(acac)₃ amount in Optima purity acetone was transferred to the 250 mL round bottom flask. Then, tetraethylene glycol (TEG) was added until the Pt/TEG ratio was 9.11 mg Pt/ 15 mL of TEG. The sample was then degassed at 100 °C under vacuum to remove acetone for 1 hr while stirring. Ar was added to the sample, an Ar balloon was attached, and the sample was heated to 170 °C over 28 min, then to 200 °C over 12 min, and then held at 200 °C for 2 hrs. The sample then cooled to room temperature. The sample was diluted using 2 mL of acetone per 1 mL of TEG used in the reaction and centrifuged at 10,000 rpm for 30 min at 30 °C. The sample was washed 3 more times with acetone, transferred to a 5 mL vial using acetone, and then dried using rotary evaporation.

Calcination and Reduction of Pt₅Fe_x@mSiO₂. The samples were first dried in air for 2 hrs at 100 °C, then heated to 550 °C in an oven using a ramping rate of 1 °C/min. The samples were reduced using 10% H₂/Ar at 300 and 500 °C in test tubes and at 700 °C in quartz boats immediately before the reaction when studying the effect of reduction

temperature. The samples were reduced using a ramping rate of 5 °C/min and then held at the desired reduction temperature for 6 hrs. The samples cooled to room temperature naturally. They were immediately treated with a ligand exchange process followed by cinnamaldehyde hydrogenation experiments.

Ligand (Organic Capping Agent) Attachment Conditions. In 100 μL of Optima purity acetone, 8.61 mg of decanoic or 25.70 mg of perfluorodecanoic acid were dissolved. This solution was used to wash each 700 °C reduced sample into a test tube, followed by washing with 1 mL of Optima purity dichloromethane. For the 300 and 500 °C reduced samples, the solutions were added to the test tubes directly. The test tubes were capped with septa and sonicated for 1 hr. Next, the samples were centrifuged at 3000 rpm for 10 min at 30 °C and the supernatant was removed.

Cinnamaldehyde Hydrogenation. Immediately after the ligand exchange process, 500 μL of n-hexane, 100 μL of perfluorodecalin, and 20 μL of cinnamaldehyde were added to the test tubes. The sample was capped with a septum and purged for 10 seconds using H_2 , then protected with an H_2 balloon. The samples were heated at 50 °C for 3 hrs while stirring. Next, 10 μL of mesitylene were added as the internal standard and the samples were then diluted with 1 mL of toluene. The samples were centrifuged at 3000 rpm for 10 min at 30 °C and the top layer was transferred to a GC vial for immediate analysis. The products were analyzed on a Agilent 6890 N Network GC System equipped with a HP-5 capillary column (30 m \times 0.320 mm \times 0.25 μm) with a flame ionization detectors and a Agilent 5975 inert gas mass selective detector equipped with a HP-5ms capillary column (30 m \times 0.250 mm \times 0.25 μm). The response factors of

each component were determined using standard samples and were used to calculate the conversion and selectivity.

Synthesis of MCM-41. Synthesis was adapted from a reported procedure.⁶³ A TTAB solution was made by dissolving 15.47 g of TTAB in 46.43 mL of ultrapure H₂O. In a 500 mL Erlenmeyer flask, 18.7 g of a 37% sodium silicate solution, 40 g of ultrapure H₂O, and 1.2 g of H₂SO₄ were sequentially added and stirred for 10 min. The TTAB solution was then added and the contents were stirred 30 min. Ultrapure water (20 mL) was then added and the contents were stirred for 10 min. The Erlenmeyer flask was then sealed with a septum and heated at 100 °C for 6 days. The product was washed with water 1x and ethanol 3x and dried at 100 °C for 3 hrs. The sample was then heated under flowing Ar at 100 °C for 2 hrs, then at 550 °C for 1 hr, then under flowing air for 6 hrs at 550 °C. A ramping rate of 1 °C/min was used.

Characterization. Inductively coupled plasma – mass spectroscopy (ICP-MS) measurements were performed using a Thermo Fisher Scientific XSeries 2 ICP-MS. To prepare samples for ICP-MS, samples were digested with 5 mL of aqua regia and 100 µL of HF for 1 hr. The samples were diluted to 50 mL with ultrapure water. For Pt ICP-MS measurements, 1 mL of this was transferred to a centrifuge tube and diluted to 50 mL with 2 wt.% HNO₃. For Fe content analysis, 1 mL of the ultrapure water diluted sample was diluted to 50 mL with 0.05 wt.% HNO₃ and analyzed using the cold plasma mode. Powder X-ray diffraction (XRD) patterns were collected at room temperature using a STOE Stadi P powder diffractometer equipped with an image plate and a CuK_{α1} radiation source ($\lambda = 1.54056 \text{ \AA}$). All XRD patterns were calibrated using a Si standard after measurements were complete. Transmission electron microscopy (TEM) samples were

prepared using the drop cast method⁶⁴⁻⁶⁵ and images were collected using a TECNAI G2 F20 instrument at an acceleration voltage of 200kV. The particle size distributions for all imaged particles was calculated using the Particle Size Analyzer macro⁶⁶ on ImageJ software⁶⁷ by measuring at least 100 randomly chosen particles. Physisorption analyses were performed using a Micromeritics 3Flex surface characterization analyzer at 77 K with N₂. Before analysis, the samples were degassed at 250 °C for 12 hrs under vacuum ($\sim 5 \times 10^{-5}$ Torr). At least 75 mg of Pt@mSiO₂, Pt₅Fe_x@mSiO₂, and MCM-41 were analyzed to reduce random error during sample measurement. The desorption branch of the isotherm was used to calculate the BJH pore sizes and BET surface areas. Diffuse reflectance infrared Fourier transform spectroscopy (DRIFTS) measurements were performed using an Agilent Cary 670 FTIR equipped with a linearized MCT detector, a Harrick diffuse reflectance accessory, and a Praying Mantis high-temperature reaction chamber. Before analysis, the samples were dried at 70 °C for 30 min under 20 mL/min He flow. X-ray photoelectron spectroscopy (XPS) was performed on a Kratos Amicus/ESCA 3400 instrument. The sample was irradiated with 240 W unmonochromated Mg *K* α x-rays ($\lambda = 1253.6$ eV), and photoelectrons emitted at 0° from the surface normal were energy analyzed using a DuPont type detector. The pass energy was set at 150 eV. An O reference energy of 532.9 eV for O 1s peaks in SiO₂ was used to calibrate the spectra. The credibility of using O as a reference peak was validated by the average value and low standard deviation of Si binding energies (103.71 ± 0.02 eV) and the proximity of the binding energy of 700 °C reduced Pt@mSiO₂ samples (71.1 eV) to the known value for zerovalent Pt 4f_{7/2} electrons (71.2 eV).

References

- (1) Taguchi, T.; Isozaki, K.; Miki, K., Enhanced Catalytic Activity of Self-Assembled-Monolayer-Capped Gold Nanoparticles. *Adv. Mater.* **2012**, *24*, 6462-6467.
- (2) Vu, K. B.; Bukhryakov, K. V.; Anjum, D. H.; Rodionov, V. O., Surface-Bound Ligands Modulate Chemoselectivity and Activity of a Bimetallic Nanoparticle Catalyst. *ACS Catal.* **2015**, 2529-2533.
- (3) Wu, B. H.; Huang, H. Q.; Yang, J.; Zheng, N. F.; Fu, G., Selective Hydrogenation of Alpha, Beta-Unsaturated Aldehydes Catalyzed by Amine-Capped Platinum-Cobalt Nanocrystals. *Angewandte Chemie-International Edition* **2012**, *51*, 3440-3443.
- (4) Yu, W. Y.; Wang, Y.; Liu, H. F.; Zheng, W., Preparation and Characterization of Polymer-Protected Pt/Co Bimetallic Colloids and Their Catalytic Properties in the Selective Hydrogenation of Cinnamaldehyde. *J. Mol. Catal. A-Chem.* **1996**, *112*, 105-113.
- (5) Li, G.; Jiang, D. E.; Kumar, S.; Chen, Y. X.; Jin, R. C., Size Dependence of Atomically Precise Gold Nanoclusters in Chemoselective Hydrogenation and Active Site Structure. *ACS Catal.* **2014**, *4*, 2463-2469.
- (6) Kahsar, K. R.; Schwartz, D. K.; Medlin, J. W., Liquid-and Vapor-Phase Hydrogenation of 1-Epoxy-3-Butene Using Self-Assembled Monolayer Coated Palladium and Platinum Catalysts. *Appl. Catal. A-Gen.* **2012**, *445*, 102-106.
- (7) Gonzalez-Galvez, D.; Nolis, P.; Philippot, K.; Chaudret, B.; van Leeuwen, P., Phosphine-Stabilized Ruthenium Nanoparticles: The Effect of the Nature of the Ligand in Catalysis. *ACS Catal.* **2012**, *2*, 317-321.
- (8) Ranu, B. C.; Dey, R.; Chatterjee, T.; Ahammed, S., Copper Nanoparticle-Catalyzed Carbon-Carbon and Carbon-Heteroatom Bond Formation with a Greener Perspective. *ChemSusChem* **2012**, *5*, 22-44.
- (9) Toshima, N.; Shiraiishi, Y.; Teranishi, T.; Miyake, M.; Tominaga, T.; Watanabe, H.; Brijoux, W.; Bonnemann, H.; Schmid, G., Various Ligand-Stabilized Metal Nanoclusters as Homogeneous and Heterogeneous Catalysts in the Liquid Phase. *Appl. Organomet. Chem.* **2001**, *15*, 178-196.
- (10) Niu, Z.; Li, Y., Removal and Utilization of Capping Agents in Nanocatalysis. *Chem. Mat.* **2013**, *26*, 72-83.
- (11) Lopez-Sanchez, J. A.; Dimitratos, N.; Hammond, C.; Brett, G. L.; Kesavan, L.; White, S.; Miedziak, P.; Tiruvalam, R.; Jenkins, R. L.; Carley, A. F.; Knight, D.; Kiely, C. J.; Hutchings, G. J. Facile Removal of Stabilizer-Ligands from Supported Gold Nanoparticles. *Nat. Chem.* **2011**, *3*, 551-556.

- (12) Aliaga, C.; Park, J. Y.; Yamada, Y.; Lee, H. S.; Tsung, C. K.; Yang, P. D.; Somorjai, G. A., Sum Frequency Generation and Catalytic Reaction Studies of the Removal of Organic Capping Agents from Pt Nanoparticles by UV-Ozone Treatment. *J. Phys. Chem. C* **2009**, *113*, 6150-6155.
- (13) Crespo-Quesada, M.; Andanson, J. M.; Yarulin, A.; Lim, B.; Xia, Y. N.; Kiwi-Minsker, L., UV-Ozone Cleaning of Supported Poly(Vinylpyrrolidone)-Stabilized Palladium Nanocubes: Effect of Stabilizer Removal on Morphology and Catalytic Behavior. *Langmuir* **2011**, *27*, 7909-7916.
- (14) Liu, Z. F.; Shamsuzzoha, M.; Ada, E. T.; Reichert, W. M.; Nikles, D. E., Synthesis and Activation of Pt Nanoparticles with Controlled Size for Fuel Cell Electrocatalysts. *J. Power Sources* **2007**, *164*, 472-480.
- (15) Li, D.; Wang, C.; Tripkovic, D.; Sun, S.; Markovic, N. M.; Stamenkovic, V. R., Surfactant Removal for Colloidal Nanoparticles from Solution Synthesis: The Effect on Catalytic Performance. *ACS Catal.* **2012**, *2*, 1358-1362.
- (16) Deutsch, D. S.; Siani, A.; Fanson, P. T.; Hirata, H.; Matsumoto, S.; Williams, C. T.; Amiridis, M. D., FT-IR Investigation of the Thermal Decomposition of Poly(Amidoamine) Dendrimers and Dendrimer-Metal Nanocomposites Supported on Al₂O₃ and ZrO₂. *J. Phys. Chem. C* **2007**, *111*, 4246-4255.
- (17) Mazumder, V.; Sun, S. H., Oleylamine-Mediated Synthesis of Pd Nanoparticles for Catalytic Formic Acid Oxidation. *J. Am. Chem. Soc.* **2009**, *131*, 4588-+.
- (18) Wu, J. B.; Zhang, J. L.; Peng, Z. M.; Yang, S. C.; Wagner, F. T.; Yang, H., Truncated Octahedral Pt₃Ni Oxygen Reduction Reaction Electrocatalysts. *J. Am. Chem. Soc.* **2010**, *132*, 4984-+.
- (19) Naresh, N.; Wasim, F. G. S.; Ladewig, B. P.; Neergat, M., Removal of Surfactant and Capping Agent from Pd Nanocubes (Pd-Ncs) Using Tert-Butylamine: Its Effect on Electrochemical Characteristics. *Journal of Materials Chemistry A* **2013**, *1*, 8553-8559.
- (20) Marshall, S. T.; O'Brien, M.; Oetter, B.; Corpuz, A.; Richards, R. M.; Schwartz, D. K.; Medlin, J. W., Controlled Selectivity for Palladium Catalysts Using Self-Assembled Monolayers. *Nat. Mater.* **2010**, *9*, 853-858.
- (21) Kwon, S. G.; Krylova, G.; Sumer, A.; Schwartz, M. M.; Bunel, E. E.; Marshall, C. L.; Chattopadhyay, S.; Lee, B.; Jellinek, J.; Shevchenko, E. V., Capping Ligands as Selectivity Switchers in Hydrogenation Reactions. *Nano Lett.* **2012**, *12*, 5382-5388.

- (22) Ofir, Y.; Samanta, B.; Arumugam, P.; Rotello, V. M., Controlled Fluorination of FePt Nanoparticles: Hydrophobic to Superhydrophobic Surfaces. *Adv. Mater.* **2007**, *19*, 4075-+.
- (23) Kulkarni, S. A.; Ogale, S. B.; Vijayamohanan, K. P., Tuning the Hydrophobic Properties of Silica Particles by Surface Silanization Using Mixed Self-Assembled Monolayers. *J. Colloid Interface Sci.* **2008**, *318*, 372-379.
- (24) Kamegawa, T.; Mizuno, A.; Yamashita, H., Hydrophobic Modification of SO₃H-Functionalized Mesoporous Silica and Investigations on the Enhanced Catalytic Performance. *Catal. Today* **2015**, *243*, 153-157.
- (25) Mbaraka, I. K.; Shanks, B. H., Design of Multifunctionalized Mesoporous Silicas for Esterification of Fatty Acid. *J. Catal.* **2005**, *229*, 365-373.
- (26) Wang, L.; Wang, H.; Liu, F. J.; Zheng, A. M.; Zhang, J.; Sun, Q.; Lewis, J. P.; Zhu, L. F.; Meng, X. J.; Xiao, F. S., Selective Catalytic Production of 5-Hydroxymethylfurfural from Glucose by Adjusting Catalyst Wettability. *ChemSusChem* **2014**, *7*, 402-406.
- (27) Chen, C.; Shi, S.; Wang, M.; Ma, H.; Zhou, L. P.; Xu, J., Superhydrophobic SiO₂-Based Nanocomposite Modified with Organic Groups as Catalyst for Selective Oxidation of Ethylbenzene. *Journal of Materials Chemistry A* **2014**, *2*, 8126-8134.
- (28) Nakatsuka, K.; Mori, K.; Okada, S.; Ikurumi, S.; Kamegawa, T.; Yamashita, H., Hydrophobic Modification of Pd/SiO₂@Single-Site Mesoporous Silicas by Triethoxyfluorosilane: Enhanced Catalytic Activity and Selectivity for One-Pot Oxidation. *Chem.-Eur. J.* **2014**, *20*, 8348-8354.
- (29) Oduro, W. O.; Cailuo, N.; Yu, K. M. K.; Yang, H. W.; Tsang, S. C., Geometric and Electronic Effects on Hydrogenation of Cinnamaldehyde over Unsupported Pt-Based Nanocrystals. *Phys. Chem. Chem. Phys.* **2011**, *13*, 2590-2602.
- (30) Delbecq, F.; Sautet, P., Electronic and Chemical Properties of the Pt₈₀Fe₂₀(111) Alloy Surface: A Theoretical Study of the Adsorption of Atomic H, Co, and Unsaturated Molecules. *J. Catal.* **1996**, *164*, 152-165.
- (31) Taniya, K.; Hara, T.; Imai, T.; Ichihashi, Y.; Nishiyama, S., Preparation of Silica-Coated SnPt Bimetallic Nanoparticle Catalysts for the Selective Hydrogenation of Cinnamaldehyde. *J. Chem. Eng. Jpn.* **2014**, *47*, 130-135.
- (32) Taniya, K.; Jinno, H.; Kishida, M.; Ichihashi, Y.; Nishiyama, S., Preparation of Sn-Modified Silica-Coated Pt Catalysts: A New Pt-Sn Bimetallic Model Catalyst for Selective Hydrogenation of Crotonaldehyde. *J. Catal.* **2012**, *288*, 84-91.

- (33) Wang, G.-H.; Hilgert, J.; Richter, F. H.; Wang, F.; Bongard, H.-J.; Spliethoff, B.; Weidenthaler, C.; Schüth, F., Platinum–Cobalt Bimetallic Nanoparticles in Hollow Carbon Nanospheres for Hydrogenolysis of 5-Hydroxymethylfurfural. *Nat. Mater.* **2014**, *13*, 293-300.
- (34) Gallezot, P.; Richard, D., Selective Hydrogenation of Alpha, Beta-Unsaturated Aldehydes. *Catal. Rev.-Sci. Eng.* **1998**, *40*, 81-126.
- (35) Saudan, L. A., Hydrogenation Processes in the Synthesis of Perfumery Ingredients. *Accounts Chem. Res.* **2007**, *40*, 1309-1319.
- (36) Joback, K. G.; Reid, R. C., Estimation of Pure-Component Properties from Group-Contributions. *Chem. Eng. Commun.* **1987**, *57*, 233-243.
- (37) Chemeo High Quality Chemical Properties Database. <https://www.chemeo.com/> (accessed 8/18/15).
- (38) Bagaria, H. G.; Ada, E. T.; Shamsuzzoha, M.; Nikles, D. E.; Johnson, D. T., Understanding Mercapto Ligand Exchange on the Surface of FePt Nanoparticles. *Langmuir* **2006**, *22*, 7732-7737.
- (39) Mahata, N.; Goncalves, F.; Pereira, M. F. R.; Figueiredo, J. L., Selective Hydrogenation of Cinnamaldehyde to Cinnamyl Alcohol over Mesoporous Carbon Supported Fe and Zn Promoted Pt Catalyst. *Appl. Catal. A-Gen.* **2008**, *339*, 159-168.
- (40) Galvagno, S.; Donato, A.; Neri, G.; Pietropaolo, R.; Pietropaolo, D., Hydrogenation of Cinnamaldehyde over Platinum Catalysts - Influence of Addition of Metal Chlorides. *Journal of Molecular Catalysis* **1989**, *49*, 223-232.
- (41) Richard, D.; Ockelford, J.; Giroirfendler, A.; Gallezot, P., Composition and Catalytic Properties in Cinnamaldehyde Hydrogenation of Charcoal-Supported, Platinum Catalysts Modified by FeCl₂ Additives. *Catalysis Letters* **1989**, *3*, 53-58.
- (42) Zheng, R. Y.; Porosoff, M. D.; Weiner, J. L.; Lu, S. L.; Zhu, Y. X.; Chen, J. G. G., Controlling Hydrogenation of C=O and C=C Bonds in Cinnamaldehyde Using Silica Supported Co-Pt and Cu-Pt Bimetallic Catalysts. *Appl. Catal. A-Gen.* **2012**, *419*, 126-132.
- (43) Pei, Y.; Maligal-Ganesh, R. V.; Xiao, C.; Goh, T.-W.; Brashler, K.; Gustafson, J. A.; Huang, W., An Inorganic Capping Strategy for the Seeded Growth of Versatile Bimetallic Nanostructures. *Nanoscale* **2015**, *7*, 16721-16728.
- (44) Joo, S. H.; Park, J. Y.; Tsung, C. K.; Yamada, Y.; Yang, P. D.; Somorjai, G. A., Thermally Stable Pt/Mesoporous Silica Core-Shell Nanocatalysts for High-Temperature Reactions. *Nat. Mater.* **2009**, *8*, 126-131.

- (45) Cable, R. E.; Schaak, R. E., Low-Temperature Solution Synthesis of Nanocrystalline Binary Intermetallic Compounds Using the Polyol Process. *Chem. Mat.* **2005**, *17*, 6835-6841.
- (46) Schaak, R. E.; Sra, A. K.; Leonard, B. M.; Cable, R. E.; Bauer, J. C.; Han, Y. F.; Means, J.; Teizer, W.; Vasquez, Y.; Funck, E. S., Metallurgy in a Beaker: Nanoparticle Toolkit for the Rapid Low-Temperature Solution Synthesis of Functional Multimetallic Solid-State Materials. *J. Am. Chem. Soc.* **2005**, *127*, 3506-3515.
- (47) Hoene, J. V.; Charles, R. G.; Hickam, W. M., Thermal Decomposition of Metal Acetylacetonates: Mass Spectrometer Studies. *The Journal of Physical Chemistry* **1958**, *62*, 1098-1101.
- (48) Charles, R. G.; Hickam, W. M.; Vonhoene, J., The Pyrolysis of Acetylacetone. *J. Phys. Chem.* **1959**, *63*, 2084-2085.
- (49) Okamoto, H., *Fe-Pt (Iron-Platinum)*, II ed., 1990; Vol. 2.
- (50) *FindIt 1.9.3*, Fachinformationszentrum Karlsruhe, Germany, and the National Institute of Standards and Technology, United States: 2013.
- (51) Zhang, C. H.; Wan, H. J.; Yang, Y.; Xiang, H. W.; Li, Y. W., Study on the Iron-Silica Interaction of a Co-Precipitated Fe/SiO₂ Fischer-Tropsch Synthesis Catalyst. *Catal. Commun.* **2006**, *7*, 733-738.
- (52) Jmol: An Open-Source Java Viewer for Chemical Structures in 3D. <http://www.jmol.org/> (accessed 8/12/15).
- (53) Petroski, J.; El-Sayed, M. A., FTIR Study of the Adsorption of the Capping Material to Different Platinum Nanoparticle Shapes. *J. Phys. Chem. A* **2003**, *107*, 8371-8375.
- (54) Van Hardeveld, R.; Hartog, F., The Statistics of Surface Atoms and Surface Sites on Metal Crystals. *Surf. Sci.* **1969**, *15*, 189-230.
- (55) Liu, Z.; Tan, X. L.; Li, J.; Lv, C., Easy Synthesis of Bimetal PtFe-Containing Ordered Mesoporous Carbons and Their Use as Catalysts for Selective Cinnamaldehyde Hydrogenation. *New J. Chem.* **2013**, *37*, 1350-1357.
- (56) Guo, Z. Y.; Xiao, C. X.; Maligal-Ganesh, R. V.; Zhou, L.; Goh, T. W.; Li, X. L.; Tesfagaber, D.; Thiel, A.; Huang, W. Y., Pt Nanoclusters Confined within Metal Organic Framework Cavities for Chemoselective Cinnamaldehyde Hydrogenation. *ACS Catal.* **2014**, *4*, 1340-1348.

- (57) Rimola, A.; Costa, D.; Sodupe, M.; Lambert, J. F.; Ugliengo, P., Silica Surface Features and Their Role in the Adsorption of Biomolecules: Computational Modeling and Experiments. *Chem. Rev.* **2013**, *113*, 4216-4313.
- (58) Durndell, L. J.; Parlett, C. M. A.; Hondow, N. S.; Isaacs, M. A.; Wilson, K.; Lee, A. F., Selectivity Control in Pt-Catalyzed Cinnamaldehyde Hydrogenation. *Sci. Rep.* **2015**, *5*, #9425.
- (59) Jia, J. F.; Shen, J. Y.; Lin, L. W.; Xu, Z. S.; Zhang, T.; Liang, D. B., A Study on Reduction Behaviors of the Supported Platinum-Iron Catalysts. *J. Mol. Catal. A-Chem.* **1999**, *138*, 177-184.
- (60) Moulder, J. F. S., W. F.; Sobol, P. E.; Bomben, K. D., *Handbook of X-Ray Photoelectron Spectroscopy: A Reference Book of Standard Spectra for Identification and Interpretation of XPS Data*; Physical Electronics Division, Perkin-Elmer Corp.: Eden Prairie, Mn, 1992.
- (61) Cros, A., Charging Effects in X-Ray Photoelectron-Spectroscopy. *J. Electron Spectrosc. Relat. Phenom.* **1992**, *59*, 1-14.
- (62) Kim, M. S.; Lee, D. W.; Chung, S. H.; Hong, Y. K.; Lee, S. H.; Oh, S. H.; Cho, I. H.; Lee, K. Y., Oxidation of Ammonia to Nitrogen over Pt/Fe/ZSM5 Catalyst: Influence of Catalyst Support on the Low Temperature Activity. *J. Hazard. Mater.* **2012**, *237*, 153-160.
- (63) Beck, J. S.; Vartuli, J. C.; Roth, W. J.; Leonowicz, M. E.; Kresge, C. T.; Schmitt, K. D.; Chu, C. T. W.; Olson, D. H.; Sheppard, E. W.; McCullen, S. B.; Higgins, J. B.; Schlenker, J. L., A New Family of Mesoporous Molecular-Sieves Prepared with Liquid-Crystal Templates. *J. Am. Chem. Soc.* **1992**, *114*, 10834-10843.
- (64) Huang, W. Y.; Qian, W.; El-Sayed, M. A., Coherent Vibrational Oscillation in Gold Prismatic Monolayer Periodic Nanoparticle Arrays. *Nano Lett.* **2004**, *4*, 1741-1747.
- (65) Huang, W. Y.; Qian, W.; El-Sayed, M. A., The Optically Detected Coherent Lattice Oscillations in Silver and Gold Monolayer Periodic Nanoprism Arrays: The Effect of Interparticle Coupling. *J. Phys. Chem. B* **2005**, *109*, 18881-18888.
- (66) Sperling, R. Particle Size Analyzer Macro for ImageJ. <http://code.google.com/p/psa-macro/> (accessed 8/11/15).
- (67) Schneider, C. A.; Rasband, W. S.; Eliceiri, K. W., NIH Image to ImageJ: 25 Years of Image Analysis. *Nat. Methods* **2012**, *9*, 671-675.

CHAPTER 3

**WATER-IN-OIL MICROEMULSION PRODUCED SILICA NANOCAPSULES
FOR A TWO STEP SYNTHESIS OF ALLOY NANOPARTICLES
ENCAPSULATED IN MESOPOROUS SILICA**

Kyle Brashler, Jeff Gustafson, and Wenyu Huang

*Department of Chemistry, U.S. DOE Ames Laboratory, Iowa State University, Ames, IA
50011-3111***Abstract**

Creating easily scalable and monodisperse intermetallic compounds encapsulated in mesoporous silica using the water-in-oil microemulsion method with easily identifiable crystal phases is an important goal that our group is seeking to achieve. We have utilized a recently reported SiO₂ synthesis, a mesoporous SiO₂ coating, and a basic etching strategy to create a mesoporous shell around small PdAg particles. Organic modifiers were added in the synthesis of the core and shell, respectively, to enhance the loading efficiency of metals. This is a general method to stabilize metals during etching processes because of the affinity certain functional groups, including amides, carboxylic acids, and sulfonic acids, have towards metals. Further characterization including ICP-MS, UV-Vis, DRIFTS, XRD, physisorption tests, and catalytic studies are necessary to learn more about the structure and find applications for the yolk-shell system. Nevertheless, we have provided an excellent groundwork for future syntheses of easily scalable yolk-shell structures with tunable metal ratios.

Introduction

Silica encapsulated metals synthesized using the water-in-oil (W/O) microemulsion technique have garnered much interest because core-shell metal@SiO₂

structures can be synthesized in one step and utilized for catalytic processes.¹ Common metals that have been encapsulated for high temperature gas phase reactions include Au,¹ Ni,²⁻⁴ and Co.⁵⁻⁶ Gaseous reactants diffuse through the micropores that are inherently present to reach the catalytic core. However, catalysts that are utilized in liquid phase reactions require etching strategies to create mesopores in the structure and allow access of the reactants to the catalytic core.⁷

There have been several reported etching procedures for converting Stöber synthesized SiO₂ into mesoporous structures, such as the use of polyvinyl pyrrolidone (PVP) to stabilize surface silanol groups⁸⁻¹⁰ and selectively etch below the surface,¹¹⁻¹⁵ using cetyltrimethylammonium bromide (CTAB) as a soft template,¹⁶⁻²⁰ or using template free approaches such as etching with water,^{12, 21} salt solutions,²²⁻²³ or NaBH₄.²⁴ This has been a very useful technique for tailoring particles around 200 nm in diameter to the desired application, but it has been reported that the results of etching change drastically when decreasing the silica particle size to less than 100 nm.²⁵ This has been attributed to differences in silica porosity between large and small particles.²⁵ Therefore, etching strategies that are successful for Stöber synthesized particles can result in over-etching of the shell in W/O microemulsion synthesized silica.

There have only been a few reports on etching strategies that convert W/O microemulsion synthesized silica from microporous to mesoporous. Most of these have been published by Mou's research group.^{7, 26-27} Their strategy utilizes water as a green and ubiquitous etchant, but the catalyst does not allow access of all liquid substrates to the core, as evidenced in control experiments with meso-2,3-dimercaptosuccinic acid,⁷ which has a length and width of 0.762 nm and 0.404 nm, respectively, when modelled

using Jmol software.²⁸ Creating mesoporous channels is essential for providing bulkier reactants access to the catalytic core for use in liquid phase reactions, such as in biomass conversion reactions.

These reported etching techniques also focus on creating yolk-shell Au@SiO₂ structures because it has been reported that Au can be efficiently encapsulated with SiO₂ by the introduction of SiO₂ precursors containing amino groups during the synthesis of the shell.²⁹ Amino groups complex strongly with noble metals during synthesis steps, etching, and high temperature processes and therefore help during the encapsulation of noble metals with silica,³⁰ prevent leaching during etching,³¹ and hinder sintering.^{1, 32} On the other hand, to the best of our knowledge, there have been no reports on silica etching strategies where base metals (Co, Cu, Ni, Sn, Bi) have shown to be stable during the process.

After recognizing these areas that can be improved upon in reported water-in-oil microemulsion procedures, we searched for methods to synthesize monodisperse yolk-shell intermetallic compounds with mesoporous shells that can easily be characterized using XRD. This chapter discusses challenges we have encountered when researching and applying strategies to synthesize W/O microemulsion core-shell metal@SiO₂ structures, stabilize metals to prevent leaching, and create a mesoporous shell for biomass conversion reactions. The results from this study do not provide conditions for the synthesis of a pragmatic system readily transferable to the chemical industry, however, we have laid the groundwork for the creation of an easily scalable yolk-shell system with tunable metal ratios that could be pragmatic after some modifications. A recommendation

is given in the conclusions section for future methods to attempt to improve our final synthesized structures.

Results and Discussion

Bimetallic Alloy Formation with the Initial System

During the initial syntheses in this project a previous report for the encapsulation of Au and Pt in SiO₂ (Au@SiO₂ and Pt@SiO₂) was repeated.¹ This structure is stabilized at higher temperatures because of the addition of amino groups in the synthesis through the addition of 3-aminopropyltrimethoxy silane, and high temperature CO oxidation studies were reported by Zhang *et al.* using the particles seen in Figure 1a and 1d. The authors also demonstrated the utility of this technique with Pt as the core (Figure 1b and 1e) and we thought this would be an excellent system for the synthesis of high temperature stable Pt-based bimetallic particles.

After repeating their synthesis, high yields of the core-shell structure product (600 – 700 mg) were observed. The process results in 4.0 ± 0.2 nm Au and 4.6 ± 0.2 nm Pt, as calculated using the Scherrer equation (Figure 1f). After counting 100 Au@SiO₂ core-shell structures observed in TEM, the overall particle size was determined to be 23 ± 4 nm (Figure 1c). The Au core is slightly larger and the shell thickness is less homogeneous relative to the reported Au@SiO₂ structure, but we observed no Au particles outside of the core after employing a 200 °C oxidation treatment in air to create the TEM sample. Additionally, the Au and Pt crystallite sizes calculated from the XRD patterns indicate that the majority of the particles were protected under the high temperature conditions employed in the original paper.

After obtaining these results, we proceeded to synthesize core-shell PtM@SiO₂ (M = Cu, Ni, Co). As observed in Figure 2, PtCu, PtNi, and PtCo alloys were successfully obtained after reducing the samples at 600 °C for 1 hr. Furthermore, after employing an oxidation treatment in air for 6 hrs at 400 °C, the pattern for PtCo particles shifts back towards the Pt phase, possibly because of the formation of cobalt silicates.

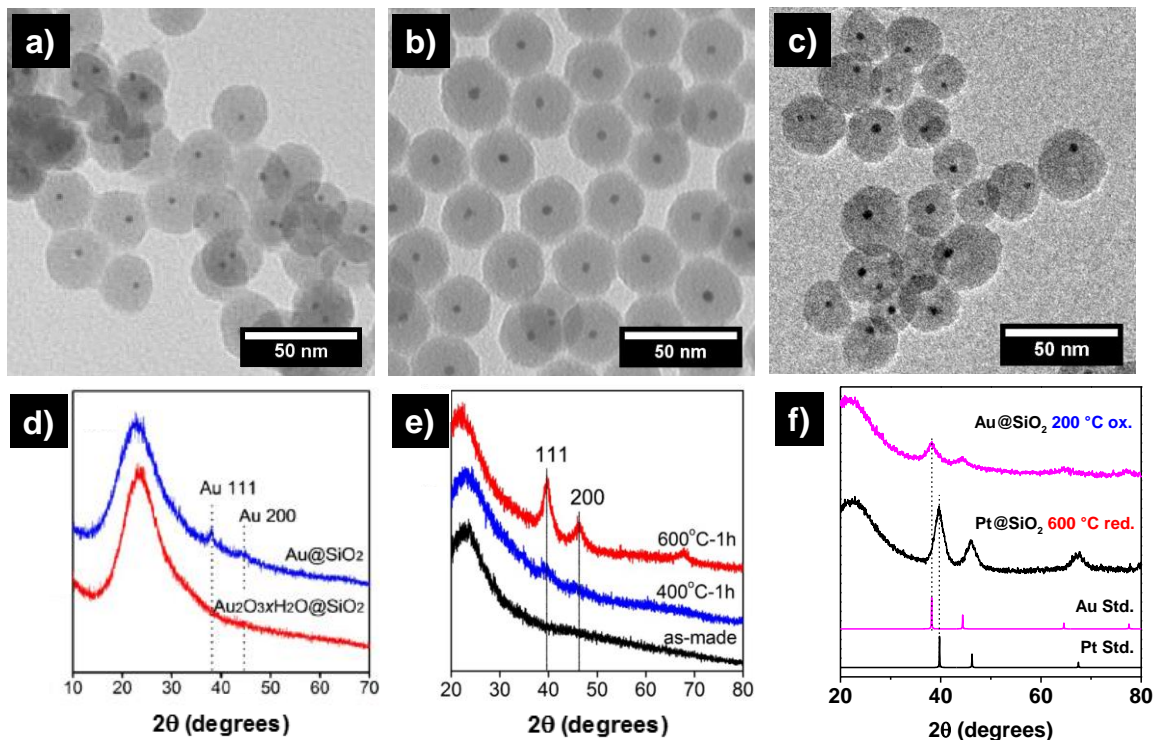


Figure 1. Comparison between published syntheses of Au@SiO₂ and Pt@SiO₂ and our attempts to repeat reported results. Au particles were oxidized in air for 2 hrs at 200 °C, and Pt was reduced in 10% H₂/Ar for 1 hr at 600 °C. a-b) TEM images of reported Au@SiO₂ and Pt@SiO₂, respectively. c) TEM image of our synthesis of Au@SiO₂. d-e) XRD patterns of reported Au@SiO₂ and Pt@SiO₂, respectively. f) XRD patterns of our syntheses of Au@SiO₂ and Pt@SiO₂.

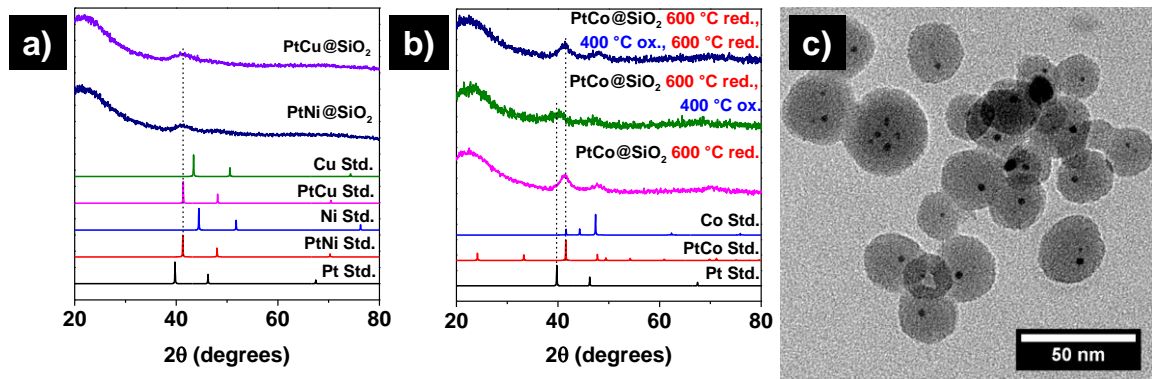


Figure 2. High temperature treated W/O microemulsion synthesized PtM@SiO_2 ($M = \text{Cu, Ni, Co}$). Reduction treatments were for 1 hr. Oxidation treatments were for 6 hrs. a) PtNi@SiO_2 and PtCu@SiO_2 after reducing the samples at 600 °C. b) PtCo@SiO_2 after high temperature oxidation and reduction treatments. c) TEM image of PtCo@SiO_2 PtCo@SiO_2 after the treatment with iterant ROR processes (PtCo@SiO_2 , 600 °C red., 400 °C ox., 600 °C red.)

After completing an additional reduction treatment, the pattern is characteristic of the PtCo phase again. This iterant reduction-oxidation-reduction (ROR) treatment shows that the PtCo phase can form if oxidation treatments are necessary to remove coke that builds up during biomass conversion reactions. In the TEM images observed in Figure 2c, however, there are multicores in the silica after the reaction is complete, and a large particle has formed outside of the silica shell. This indicated that the synthesis needed to be modified to prevent large particles from forming during iterant ROR treatments.

Meanwhile, we attempted the synthesis of PtSn@SiO_2 . Figure 3 shows the results after reducing the PtSn@SiO_2 catalyst for 1 hr at four reduction temperatures. When higher temperatures are utilized the peak that aligns with Pt shifts in the direction of the

PtSn phase, but the peak remains too broad to create claims about the intermetallic phase responsible for enhanced activity or selectivity if this was used for catalysis studies. To circumvent this problem, the Pt and Sn concentrations in the synthesis were doubled and sharp peaks characteristic of the PtSn phase were visible. However, after observing TEM images of the sample, it is apparent that the sharp peaks are from large PtSn particles and several small, unidentifiable particles remain in the silica shell.

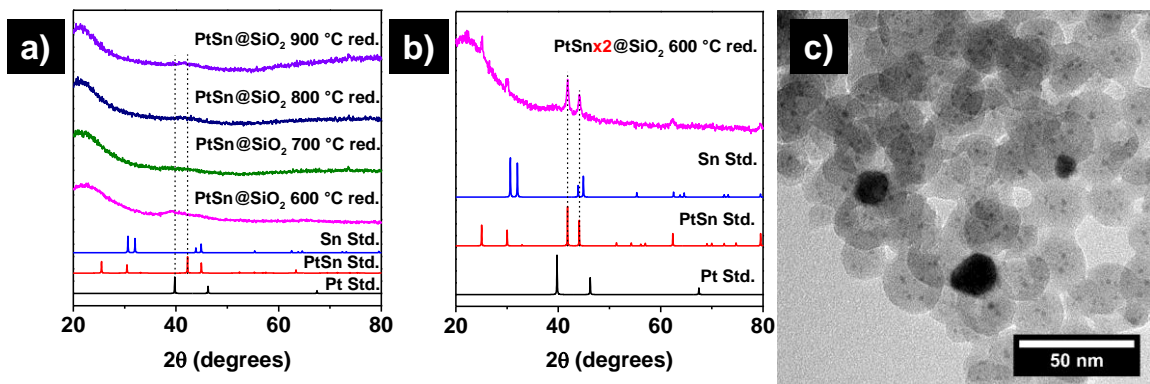


Figure 3. Attempts at synthesizing high temperature stable PtSn@SiO₂ samples. All particles shown were reduced for 1 hr. a) Shifts from Pt to PtSn phase in XRD patterns as temperature is increased. b-c) XRD and TEM results after doubling the concentration of Pt and Sn when repeating the synthesis of PtSn@SiO₂ particles.

Ni@SiO₂ as a Model Nanostructure to Improve the Initial System

It is apparent from these preliminary studies that modifications to this system were necessary to create high temperature stable ordered alloys whose phases can be identified using XRD. As observed in Figure 1, the Au@SiO₂ structures we synthesized were less homogeneous relative to the reported Au@SiO₂ and Pt@SiO₂ size distributions. Improving the size distribution would also improve high temperature

stability, because the cores would need to diffuse farther to leave the SiO₂ shell. We used Ni particles as a model for the improvement of the homogeneity of the particle size because it is less expensive than Au and Pt, but still acts as a catalyst for several reactions.²⁻⁴

We managed to improve the size distribution of the core-shell particles by varying the times between the additions of NH₄OH, 3-aminopropyltrimethoxy silane (APTMS), and tetraethyl orthosilicate (TEOS) as seen in Figure 4. When following the reported procedure (Figures 4a-c), we used an initial wait time of 2 min between additions of NH₄OH and APTMS and a final wait time of 2 min between additions of APTMS and TEOS. We tested the effects of lengthening the initial wait time to 30 min while keeping the final wait time at 2 min (Figures 4d-f) and tried keeping the initial wait time at 2 min while extending the final wait time to 30 min (Figures 4g-i). When comparing Figures 4c and 4f, it is apparent that the particle size distribution decreases and the average size of the particles increases when using a longer initial wait time. This change in size distribution likely occurs because the NH₄OH is an aqueous solution and needs to stabilize with the aqueous phase containing the Ni precursor. If the APTMS and TEOS interact with water and NH₄OH too early, they quickly react with the emulsion droplets and form SiO₂ particles before the aqueous emulsion droplets are homogeneous in volume. The heterogeneity of the particle size further increases when a long wait time is present between additions of APTMS and TEOS. It is possible that APTMS condenses quickly in the H₂O emulsion droplets and creates large seeds for the nucleation of TEOS after it is added.

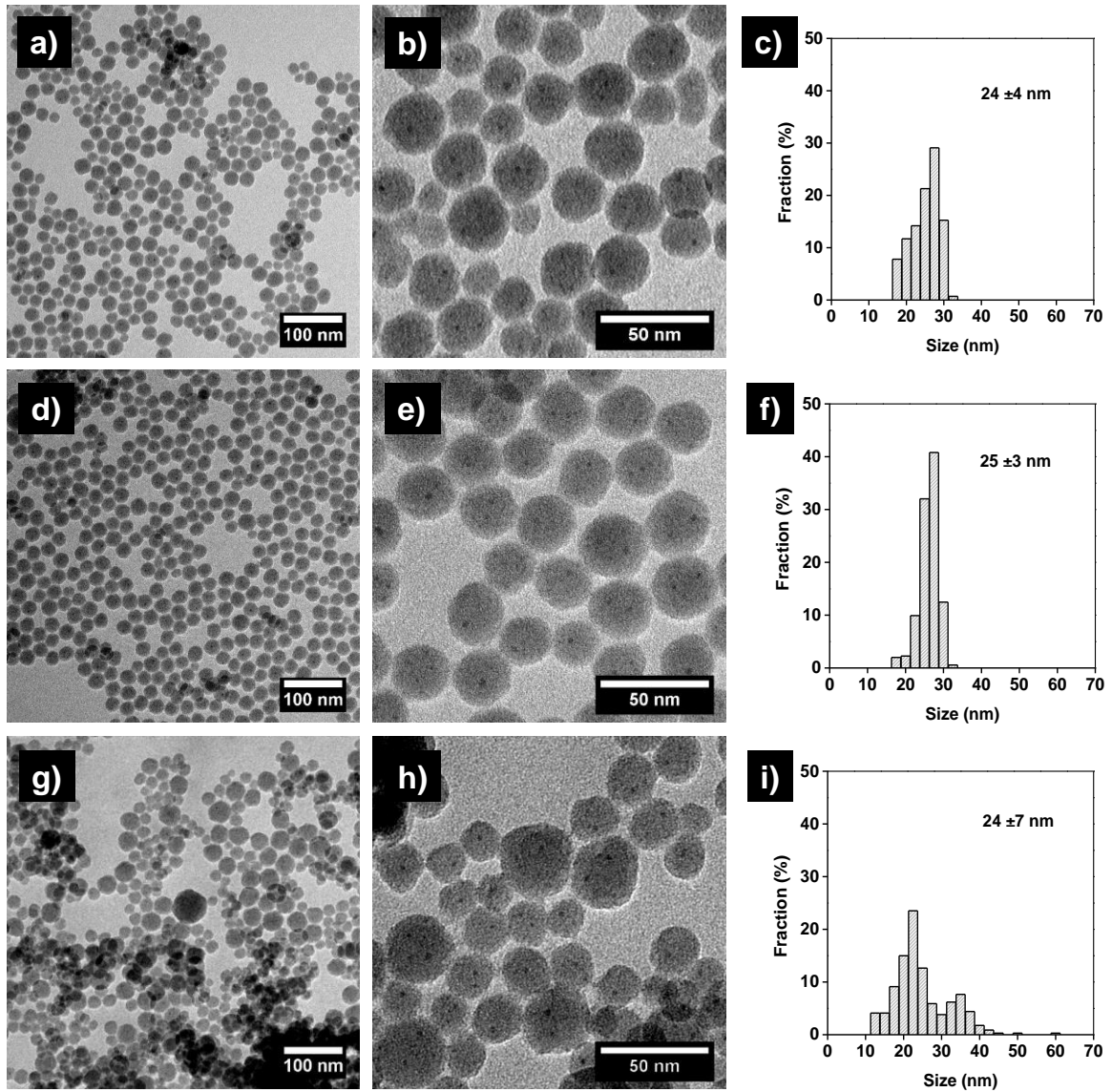


Figure 4. Changes in particle size standard deviation with modified wait times between sequential addition of NH_4OH , APTMS, and TEOS. a-c) Added NH_4OH , waited 2 min, added APTMS, waited 2 min, added TEOS. d-f) Added NH_4OH , waited 30 min, added APTMS, waited 2 min, added TEOS. g-j) Added NH_4OH , waited 2 min, added APTMS, waited 30 min, added TEOS. At least 250 particles were counted to create size distribution histograms.

After the particle size distributions were improved, the concentrations of Ni in the samples were scaled up to see if we could identify the phases present more easily by making larger Ni cores. Figure 5 shows the results after doubling ($\text{Ni}_{x2}@\text{SiO}_2$) and quadrupling ($\text{Ni}_{x4}@\text{SiO}_2$) the Ni content. Here, it is observed that XRD patterns for particles with twice as much Ni have more easily observable Ni phases, but quadrupling the content does not cause a further size increase. To understand more about how increasing Ni concentration affects the particle size, the wt.% of Ni in the three samples was estimated using ICP-MS. As observed in Table 1, the Ni wt.% increases almost proportionally to the increase in Ni content during the synthesis, as expected.

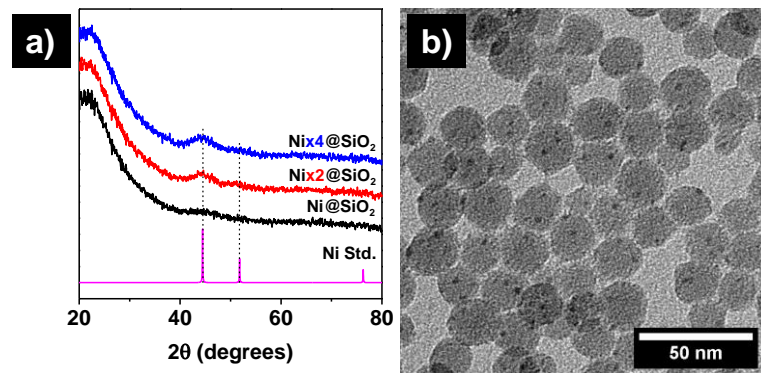


Figure 5. a) XRD pattern peaks for $\text{Ni}@\text{SiO}_2$ samples after scaling up the concentration of Ni in the synthesis. b) TEM image of $\text{Ni}_{x4}@\text{SiO}_2$. All samples were reduced at 600 °C for 1 hr.

	$\text{Ni}@\text{SiO}_2$	$\text{Ni}_{x2}@\text{SiO}_2$	$\text{Ni}_{x4}@\text{SiO}_2$
wt. %	1.80	4.35	6.76
Ni wt. % Increase Relative to $\text{Ni}@\text{SiO}_2$	1.00	2.42	3.76
XRD Crystallite Size	-	2.2 ± 0.4	2.0 ± 0.2

TEM was completed to understand why the Ni crystallite sizes did not change significantly between the Ni_x2@SiO₂ and Ni_x4@SiO₂ samples. The TEM image in Figure 5b shows the presence of multi-core particles in Ni_x4@SiO₂. When the concentration gets high, it is possible that Ni particles that form have a lower surface energy and are stabilized from sintering under the reduction conditions utilized. It is also possible that the formation of nickel silicates helps stabilize the particles.³ Some Ni is also observed on the edges of the SiO₂. It is apparent that creating monodisperse particles is not enough of an enhancement to keep particles in the center of the spheres, therefore, a different W/O microemulsion synthesis was tested as a method to synthesize particles useful for our group's goals.

Coating and Etching Ni@SiO₂ Nanocapsules

As mentioned in the introduction, etching strategies for W/O microemulsion synthesized particles do not result in particles that are porous enough to permit molecules less than one nm in length to access the core. A recent publication by Cai's research group shows that it is possible to coat 50 nm SiO₂ spheres synthesized using the W/O microemulsion method with a 7.5 nm mesoporous silica (mSiO₂) shell.¹⁶ Afterwards, the core can be etched away in the same step using Na₂CO₃. The authors also follow a well cited paper published by Osseo-Asare and Arriagada³³ to synthesize the SiO₂ spheres using the W/O microemulsion method (Figure 6a), but this process does not add water in a step separate from the addition of aqueous NH₄OH.

We decided to modify this procedure to stabilize metals using this method. As made W/O microemulsion silica samples and silica coated and etched samples are

henceforth designated “I-SiO₂” and “I-mSiO₂,” respectively, and the “I” designation is from the use of a different surfactant, Igepal CO-520, during the synthesis. Initially, the results in the original paper were repeated, and our synthesized I-mSiO₂ was slightly smaller than the published results, as seen in Figures 6b and 6c. To modify Osseo-Asare and Arriagada’s method of making I-SiO₂ spheres, we substituted 56 μL of ultrapure H₂O for some of the aqueous NH₄OH with the intention of dissolving metals in the ultrapure H₂O in future experiments, and then we added the remaining aqueous NH₄OH. As depicted in Figure 6d, there is no visible difference in the final product when 56 μL of aqueous NH₄OH is replaced with ultrapure H₂O during the synthesis.

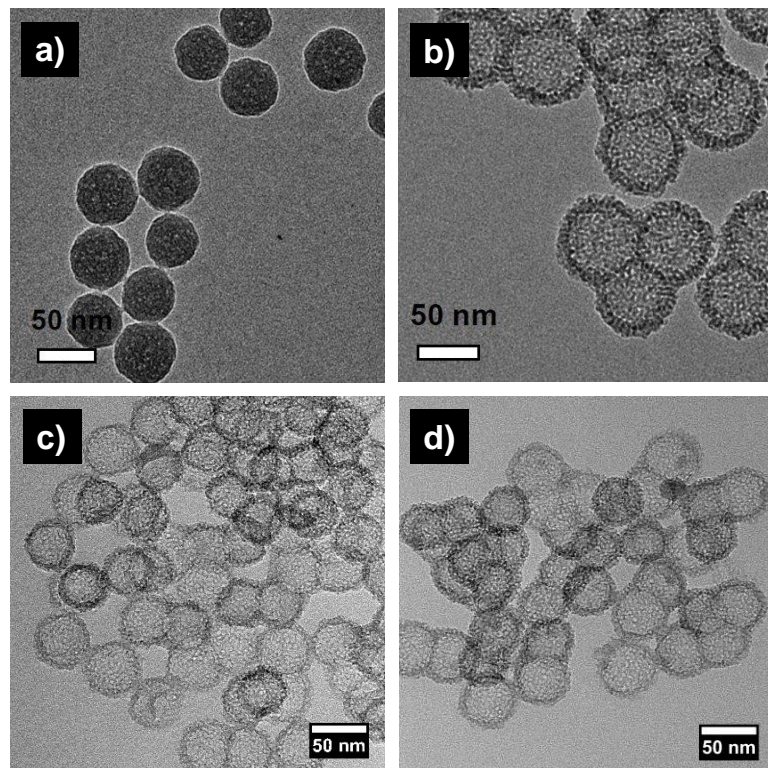
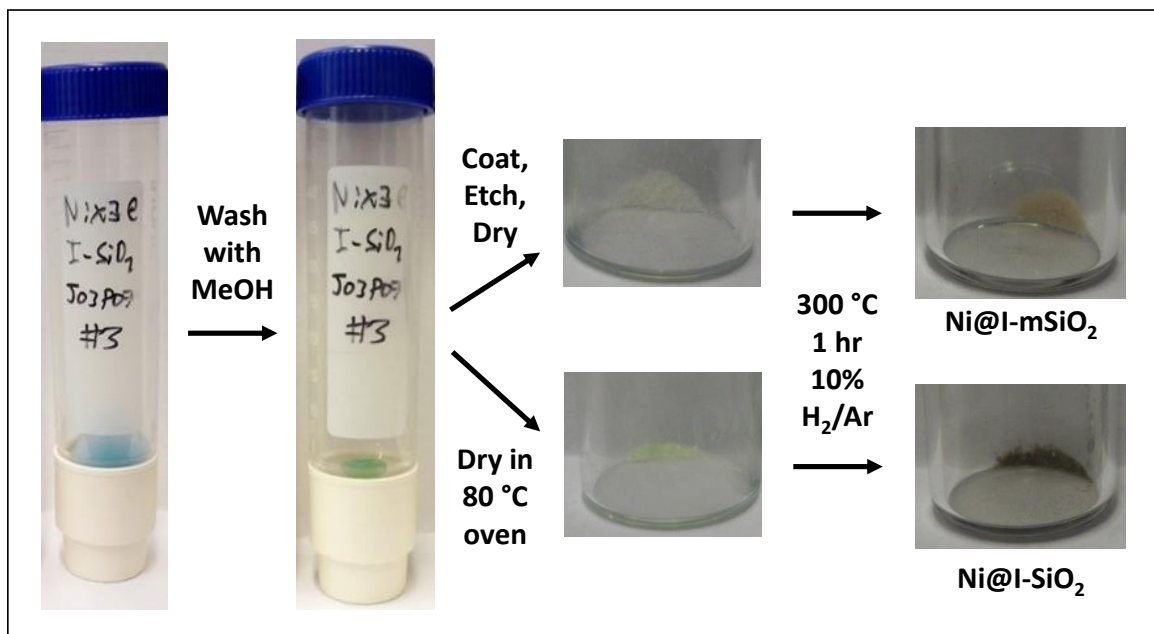


Figure 6. a) Reported solid SiO₂ spheres and b) mSiO₂ spheres. c) Repeated synthesis of Figure 6b. d) Modified synthesis of the sample in Figure 6b, where 0.56 μL of H₂O and 0.224 μL of NH₄OH was used instead of 0.28 μL of NH₄OH.

The next step involved adding Ni precursors to the H₂O layer to see if Ni(OH)₂ would precipitate out after the addition of NH₄OH and remain insoluble during the coating and etching steps. As seen in Scheme 1, the starting sample is a blue color, likely from the formation of Ni-ammine complexes. After washing with methanol, the ammonia is removed and Ni(OH)₂ remains in the sample, as evidenced from the green color present. Next, the sample was coated with mSiO₂, the core was etched, and the sample was dried and subjected to reduction treatments. When comparing Ni@I-mSiO₂ to Ni@I-SiO₂ after reduction treatments, it is apparent that a large quantity of Ni was lost during the coating and etching processes as evidenced through the relatively lighter color of the Ni@I-mSiO₂ sample.



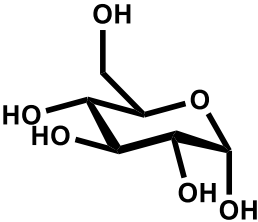
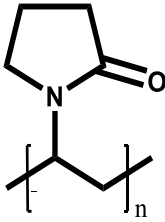
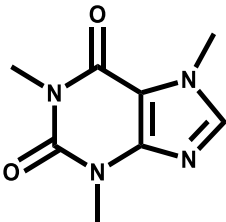
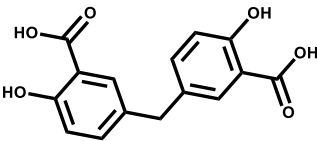
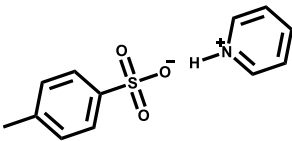
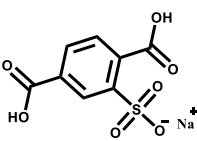
Scheme 1. Changes in Ni@I-SiO₂ samples during washing, coating, etching, drying, and reduction steps.

Organic Additives for Enhanced Metal Loading

The original hypothesis that hydroxides would remain insoluble during coating and etching steps was incorrect, and further modifications were made to increase metal loading after the transformation to yolk-shell structures. Glucose was tested as an additive that has been shown to reduce $\text{Pd}(\text{NO}_3)_2$ ³⁴ and AgNO_3 ³⁵⁻³⁶ to form PdAg, which is a catalyst commonly used for acetylene hydrogenation.³⁷ Glucose also can adsorb on the surface of the catalyst and provide steric hindrance that helps prevent passage of PdAg nanoparticles through the mesoporous shell during etching treatments. Other additives were also tested as bulky molecules that form complexes with Pd and Ag ions, as seen in Table 2.

As discussed in the synthesis section of this chapter, $\text{Pd}(\text{NO}_3)_2$ and AgNO_3 were dissolved in 20 μL of ultrapure water, then mixed with glucose dissolved in 36 μL of ultrapure water with a ratio of metals/glucose equal to 1/2. The samples were stirred for 30 min before the addition of aqueous NH_4OH . Later, TEOS was added, the sample was stirred for 2 days, and it was washed with methanol and water. The as-made PdAg-glucose@I-SiO₂ particles were coated with a mSiO₂ shell, etched, and dried, and the resulting PdAg-glucose@I-mSiO₂ was compared to the as made PdAg-glucose@I-SiO₂ nanocapsule sample after high temperature reduction treatments (Scheme 2). It was observed that the PdAg-glucose@I-mSiO₂ was much lighter in color compared to PdAg-glucose@I-SiO₂, indicating that some metal loss still occurred during the coating and etching processes. The high temperature reduced core was also dispersed in solution, coated, etched, and dried to see if reducing the particles before coating would create a

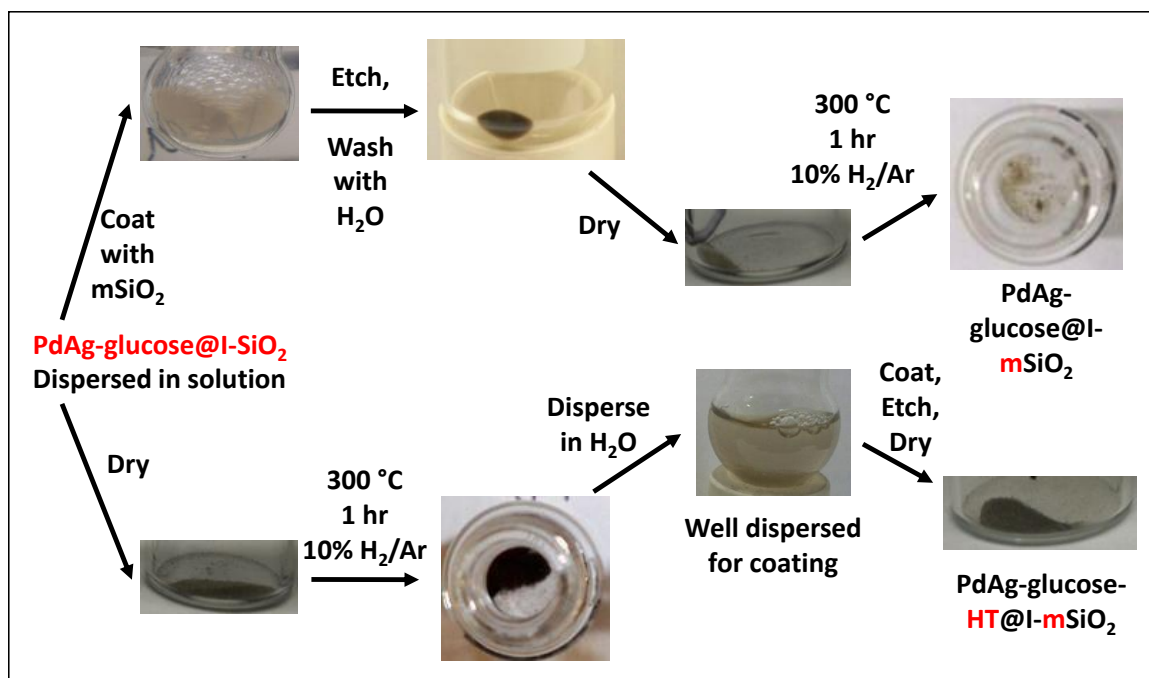
Table 2. Structures of organic additives present during synthesis of core-shell particles.

Additive Name	Glucose	Polyvinyl Pyrrolidone	Caffeine
Abbreviation	Glucose	PVP	Caffeine
Structure			
Length (nm) ^a	0.814	11.211 ^b	0.784
Additive Name	5,5'-methylenedisalicylic acid	Pyridinium p-toluenesulfonate	Monosodium 2-sulfoterephthalate
Abbreviation	MDSA	PPTS	MSSTP
Structure			
Length (nm) ^a	1.284	0.693 (p-toluenesulfonate), 0.500 (pyridinium)	0.741

^aCalculated using Jmol software version 14.2.15.²⁸After drawing the structure, the minimize function was used until the longest distance in the molecule stopped changing. ^bEstimated using a C-C bond length of 0.1246 nm.

sample that would remain dark in color. The resulting PdAg-glucose-HT@I-mSiO₂ turned slightly lighter in color compared to directly after high temperature reduction, indicating that some metal loss still occurred.

TEM characterization was completed on the three products (Figure 7). In the PdAg-glucose@I-SiO₂ sample, a single core can be observed in most of the core-shell particles. However, there are several particles present on the outside of the SiO₂ shells.



Scheme 2. Reactions with glucose as a bulky reducing agent.

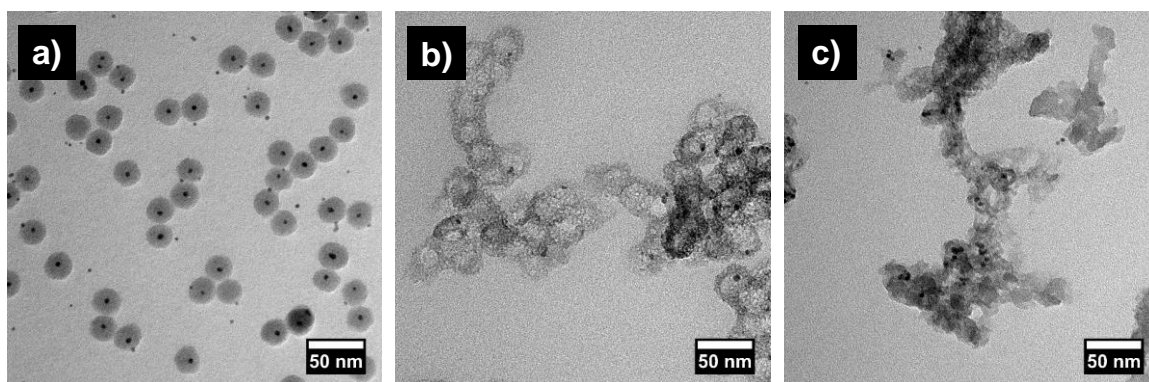


Figure 7. PdAg-glucose@I-SiO₂ based samples. a) High temperature reduced PdAg-glucose@I-SiO₂. b) High temperature reduced PdAg-glucose@I-mSiO₂. c) As synthesized PdAg-glucose-HT@I-mSiO₂.

This could be caused by hydrocarbon chains in the metal-complexed glucose having an affinity towards the non-polar cyclohexane layer resulting in transport of metals across

the cyclohexane-water interface. After adding the mSiO₂ shell and etching away the core, several yolk-shell and empty shell particles can be observed. Some particles were successfully encapsulated in the mSiO₂, but the encapsulation fraction was not high. Additionally, these particles are smaller in diameter relative to control samples with no metals or glucose present. It is apparent that either metal or glucose addition affects the final particle size, likely because of their effect on the micelle size distribution during the synthesis of PdAg-glucose@I-SiO₂. The results from applying high temperature reduction treatments before the coating process are structures that do not have a hollow area where pre-formed PdAg-glucose@I-SiO₂ particles may have existed. It is possible that the cetyltrimethylammonium chloride (CTAC) that adsorbs to the surface of the SiO₂ core and creates porous channels during the synthesis of the mSiO₂ shell did not have the same interaction after high temperature treatments were employed because of the removal of surface hydroxyl groups.³⁸

Other bulky complexing agents used to attempt to enhance the Pd and Ag loading efficiency include polyvinyl pyrrolidone (PVP), caffeine, 5,5'-methylenebisalicylic acid (MDSA), monosodium 2-sulfoterephthalate (MSSTP), and pyridinium p-toluenesulfonate (PPTS). PVP and caffeine were considered as potential loading enhancers because of the amide group presence in the polymer chain, which complexes strongly to noble metals by N and O electron donation from lone pairs.³⁹⁻⁴¹ MDSA, MSSTP, and PPTS were also considered because they contain carboxylic acid and sulfonic acid functional groups, which have been utilized in ion exchange resins.⁴²

The results after coating, etching, drying, and reducing W/O microemulsion synthesized SiO₂ are present in Figure 8, and Figure 8a shows the samples after the drying process. All 5 samples remain dark after the drying process indicating that metals

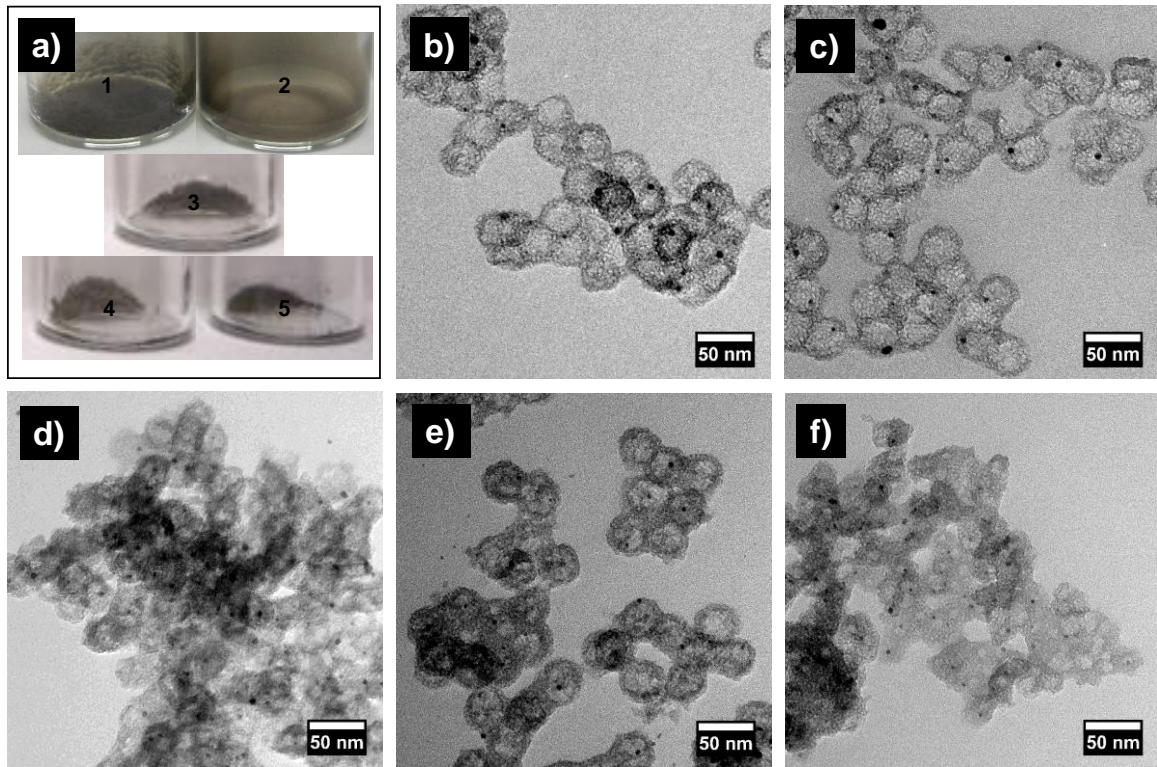


Figure 8. Samples with additives present during synthesis of the core. TEM images are after coating, etching, and drying. a) Dried samples after etching and before high temperature reduction. Images 1-5 correspond to TEM samples with b) PVP, c) caffeine, d) MDSA, e) PPTS, and f) MSSTP additives, respectively.

are still present after the coating and etching steps. TEM images in Figures 8b-f show particles that form after high temperature reduction. Samples that contain PVP, caffeine, and PPTS seem to be more successful syntheses because larger hollow areas can be observed. However, there are small PdAg particles outside of the mSiO₂ shell in the

PPTS sample, and more empty shells are observed in the sample with PVP present as an additive compared to the sample synthesized in the presence of caffeine.

The particle size distributions of the particles before the coating and etching processes were also determined using DLS as seen in Figure 9. The average particle sizes and their standard deviations are displayed in Table 3. From DLS, it can be seen that addition of Pd and Ag decreased the particle size distributions from 50 to 20 nm, whereas adding organic reagents reduces the effect that Pd and Ag addition have on the final particle size. Additionally, the starting core-shell materials containing PVP and caffeine have the greatest influence on maintaining the largest particle size distributions. These effects are important because larger starting core-shell structures should also have larger metal yolks after the etching process is complete, allowing the particles to be more easily characterized using XRD.

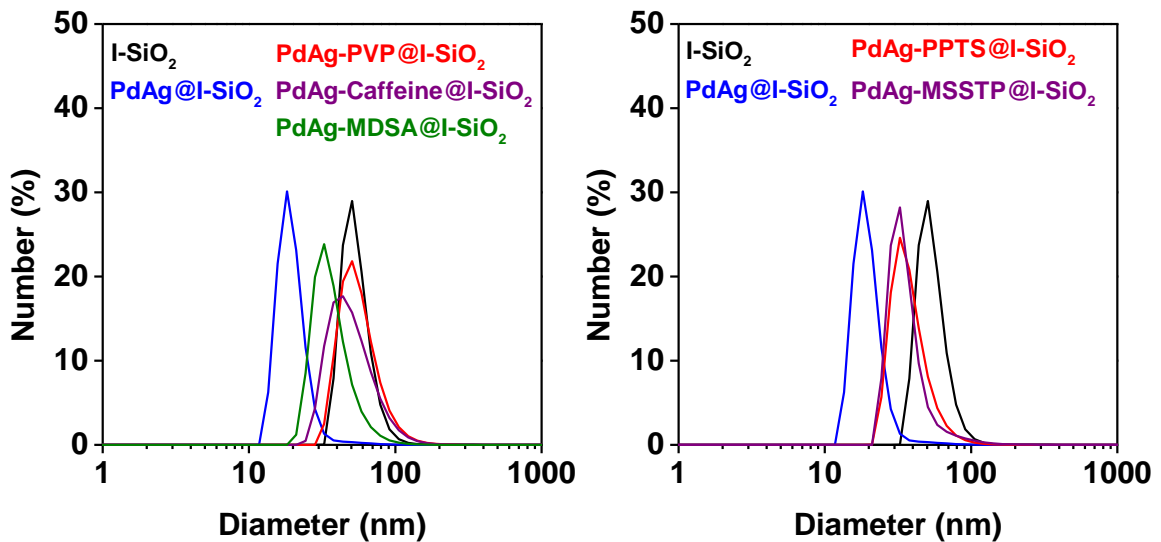


Figure 9. Size distributions of I-SiO₂ particles when including Pd(NO₃)₂, AgNO₃, and organic additives during the synthesis.

Table 3. DLS determined particle sizes of core-shell structures

Sample Name	I-SiO ₂	PdAg@ I-SiO ₂	PdAg- PVP@ I-SiO ₂	PdAg- Caffeine@ I-SiO ₂	PdAg- MDSA@ I-SiO ₂	PdAg- PPTS@ I-SiO ₂	PdAg- MSSTP@ I-SiO ₂
Particle Size (nm)	50 ± 20	20 ± 6	60 ± 20	50 ± 20	40 ± 10	40 ± 10	40 ± 20

Shell Modifications for Enhanced Metal Loading

We also attempted to add sulfonic acid functional groups to the mSiO₂ shell during the coating process instead of having it present on organic additives in the core during etching steps. This eliminated the possibility of metal ions coordinating to organic additives that are small enough to diffuse through the pores. The oxidation is necessary because thiol is known to poison Pd catalysts.⁴³⁻⁴⁴ Additionally, enhanced selectivity towards cyclohexane during the conversion of methycyclopentane has been observed in the presence of sulfonic acid in metal-organic framework supported catalysts.⁴⁵

To complete the oxidation process, 3-mercaptopropyl trimethoxysilane (MPTMS) was mixed with TEOS in MPTMS/TEOS ratios of 1/4 and 2/3 and the solution was coated on PdAg@I-SiO₂ particles to synthesize samples designated PdAg@I-SF20-mSiO₂ and PdAg@I-SF40-mSiO₂, respectively. “SF” indicates that sulfonic acid is present, and “20” and “40” indicate the percent of MPTMS in MPTMS-TEOS precursor solutions. The samples were treated at 80 °C for 1 hr to condense the precursors on the SiO₂ surface in the presence of CTAC, cooled to room temperature, and the thiol group was oxidized using 30 % H₂O₂ over a 24 hr period. A third sample with a MPTMS/TEOS ratio of 2/3 only had half of the moles of SiO₂ precursors present during the addition process, reacted for 1 hr at 80 °C, then had a pure TEOS solution added to create a sulfonic acid-free mSiO₂ shell, and lastly reacted another 1 hr at 80 °C. This sample is

designated as PdAg@SF40@I-mSiO₂. The purpose was to increase the concentration of metals on the inside of the mSiO₂ to prevent the precursors from forming metal particles on the outside of the mSiO₂. An additional sample synthesized with pure TEOS in the shell (PdAg@I-mSiO₂) was stirred for 24 hrs without any H₂O₂ added to see the effects MPTMS has on the final sample relative to pure TEOS containing samples.

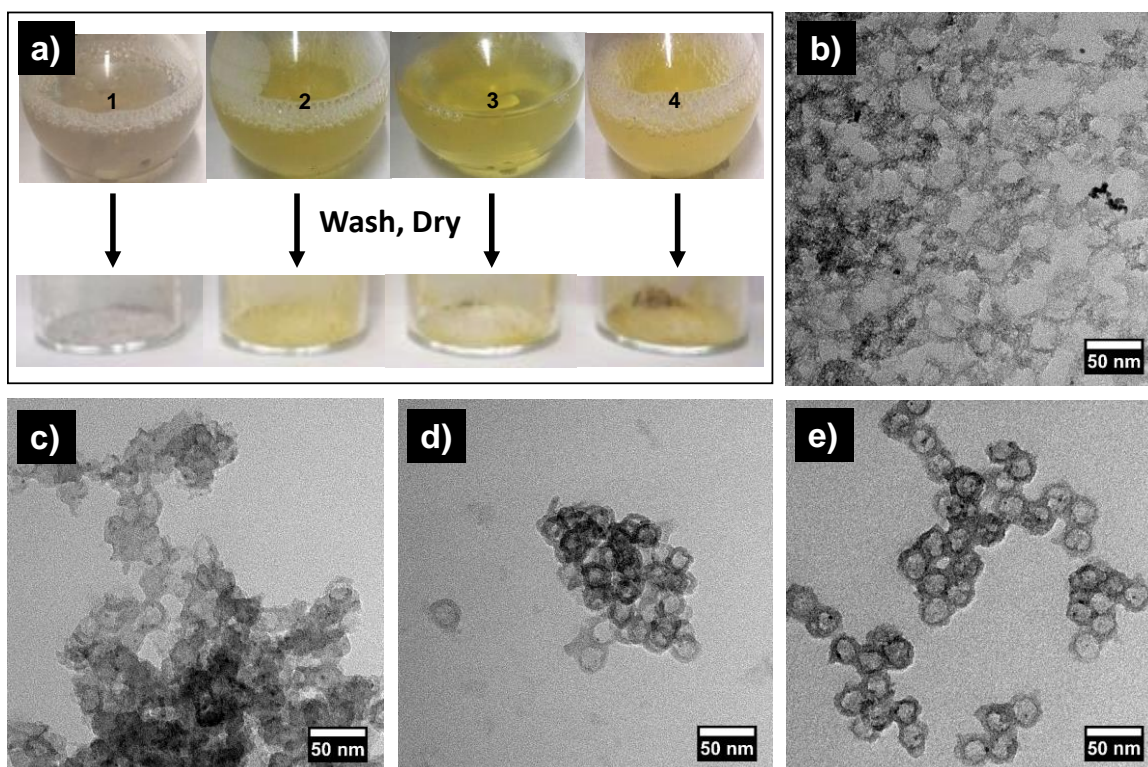


Figure 10. Coated and etched PdAg@I-SiO₂ samples synthesized with MPTMS as an additive in the shell. a) Images in flasks are after etching with Na₂CO₃. Samples 1-4 correspond to b) PdAg@I-mSiO₂, c) PdAg@I-SF20-mSiO₂, d) PdAg@I-SF40-mSiO₂, and e) PdAg@SF40@I-mSiO₂, respectively.

Images of the samples after the coating and etching processes are visible in Figure 10a. The particles with no MPTMS present during the synthesis have a visibly different color from the other 3 samples. It is possible that the MPTMS in the other samples did not oxidize to sulfonic acid groups. Additionally, the results after a 200 °C reduction treatment are visible in Figures 10b-e. It is possible that the sulfonic acid is reduced to a thiol during this process, however, it is unlikely because -OH is a poor leaving group when bonded to sulfonyl groups.⁴⁶ A report on high temperature reduction of sulfonyl groups focuses on sulfonamide and sulfonyl chloride because they are more reactive than sulfonic acid, yet they still require temperatures in the range of 160 – 210 °C and use formates as a reducing agents.⁴⁶ One-pot reduction processes to convert sulfonic acids to thiols have also been reported, but these utilize reactants that are in excess or expensive, including trifluoroacetic anhydride – tetrabutylammonium iodide mixtures,⁴⁷ and triphenylphosphine with an iodine catalyst.⁴⁸⁻⁴⁹ To the best of our knowledge, there have been no reports on the use of H₂ as a reducing agent to convert sulfonic acids to thiols, and we believe that sulfonic acid is still present in our system. However, this still needs to be confirmed using DRIFT spectroscopy. Figure 10b shows PdAg@I-mSiO₂ after the reduction process is complete. The mSiO₂ are loosely connected and PdAg particles form away from the mSiO₂ shell, showing that the shells synthesized with TEOS are not stable for long times in the presence of basic media. However, adding MPTMS improves the stability of the shells, as observed in Figures 10c-e. PdAg@SF40@I-mSiO₂ samples look as if they have a higher PdAg content compared to the PdAg@I-SF20-mSiO₂ and PdAg@I-SF40-mSiO₂ samples, and the yield of these particles is higher than the other two samples, as visible in the dried samples in Figure 10a.

Conclusions

Particles synthesized using the W/O microemulsion method can be stabilized by increasing the etching time between the addition of the aqueous components and the SiO₂ precursors. The Ni metal content is easily tunable by increasing the concentration of metal precursors in the aqueous layer when modifying the synthesis reported by Zhang and coworkers, and it may be limited by the solubility of the metal salts in the aqueous layer as evidenced by visible Ni particles on the outside of the SiO₂ core when higher Ni concentrations are used. Organic additives were also present during the synthesis of PdAg@I-SiO₂. TEM results suggest that including caffeine as an additive improves the loading efficiency of Pd and Ag relative to PVP and PPTS containing samples and furthermore improves the homogeneity of the starting solid core relative to MDSA and MSSTP containing samples. MPTMS was also tested as an additive during the synthesis of the shell to improve the loading efficiency of PdAg. PdAg@SF40@I-mSiO₂ appears to have a higher fraction of shells with metal particles present on the inside relative to the other samples synthesized in the presence of MPTMS. More particles need to be counted and the ratio of yolk-shell to empty shell structures needs to be evaluated in each sample to make a solid conclusion about the best synthesis method to proceed with.

Further characterization needs to be done on PdAg@I-mSiO₂, PdAg-caffeine@I-mSiO₂, and PdAg@SF40@I-mSiO₂ to confirm the loading efficiency of PdAg is improved through the addition of organic additives. To do this, the synthesis will need to be scaled back up to the quantities used in the reported paper. ICP-MS needs to be completed to test for leaching and changes in metal loading efficiency. Additionally, DRIFTS studies should be done to confirm that the thiol groups present in MPTMS have

been successfully converted to sulfonic acid groups after the addition of H_2O_2 . Physisorption studies should be completed while completing DRIFTS and ICP-MS tests to ensure the shell can be turned mesoporous through removal of the CTAC without damaging the sulfonic acid groups if using high temperature oxidation or etching the metal core if using acid reflux. An alternative method would be to complete extractions using mild extracting agents, such as acetic acid or NaCl. MPTMS can also be added to the shell while coating PdAg-caffeine@I-SiO₂ to see if a synergistic improvement of PdAg loading efficiency can be obtained when using both caffeine and MPTMS during the synthesis. Lastly, the Pd(NO₃)₂ and AgNO₃ concentrations during the PdAg-caffeine@I-SiO₂ can be increased to increase the particle size and make it easier to characterize metal phases present using XRD. Overall, these initial results provide an excellent foundation towards the synthesis of scalable yolk-shell systems with easily tunable metal ratios.

Materials and Methods

Materials. 5,5'-methylenedisalicylic acid (MDSA, 95%), H₂PtCl₆ (40% Pt), and H₂AuCl₄·3H₂O (ACS grade) were purchased from Acros Organics. Pyridinium p-toluenesulfonate (PPTS, ≥98%) was purchased from Alfa Aesar. Cyclohexane (ACS grade) was purchased from BDH. Na₂CO₃ (≥99.5%) and NH₄OH (14.8 M) were purchased from EMD Millipore. AgNO₃ (Certified ACS), dextrose (d-glucose, anhydrous, certified ACS), and H₂O₂ (30%) were purchased from Fisher Scientific. CoCl₂·6H₂O (99.6%) was purchased from JT Baker Chemical Co. Ar (99.995%) and H₂ (99.99%) were purchased from Matheson. Pd(NO₃)₂ was purchased from PCR Research

Chemicals. 3-aminopropyl trimethoxysilane (APTMS, 97%), 3-mercaptopropyl trimethoxysilane (MPTMS, 98%), Brij C10 (Average Mn = ~683), Igepal CO-520 (Average Mn = 441), Ni(NO₃)₂·6H₂O (≥97%), polyvinyl pyrrolidone (PVP, 10,000 MW), SnCl₄·5H₂O (98%), triethylamine (TEA, ≥99%), and tetraethyl orthosilicate (TEOS, reagent grade, 98%) were purchased from Sigma Aldrich.

Cetyltrimethylammonium chloride (CTAC, ≥95.0%) and monosodium sulfoterephthalate (MSSTP, ≥98.0%) were purchased from TCI. Materials were used as received. A Millipore Milli-Q Plus was used to make the 18.2 MΩ·cm ultrapure water.

Synthesis of Au@SiO₂ and Pt@SiO₂. In a 25 mL rbf, 4.25 g of Brij C10 and 7.5 mL of cyclohexane were added and stirred for 30 min at 50 °C. A solution containing 1.25x10⁻⁴ mol of HAuCl₄·3H₂O or H₂PtCl₆ was dissolved in 0.5 mL of ultrapure water, added to the round bottom flask dropwise with a plastic pipette, and the round bottom flask was stirred for 7 min. Then, 0.8 mL of 14.8 M NH₄OH was added dropwise and stirred for 2 min. Next, 0.150 mL 3-aminopropyl trimethoxysilane was added dropwise and stirred for 2 min. A syringe pump was used to add 2 mL of tetraethyl orthosilicate and the samples were stirred for 2 hrs. To disrupt the microemulsion, 5 mL of ethanol was added. The sample was centrifuged at 3000 rpm 10 min and washed 3x with ethanol. The sample was dried using rotary evaporation. Au@SiO₂ was oxidized in air at 200 °C for 2 hrs and a ramping rate of 1 °C/min was used. Pt@SiO₂ was additionally dried at 80 °C in an oven overnight, then reduced in 10% H₂/Ar at 600 °C for 1 hr after ramping to 600 °C using a rate of 5 °C/min.

Synthesis of PtM@SiO₂ (M = Ni, Cu, Co, Sn). Procedure is the same as the synthesis of Pt@SiO₂, with a modification. Instead of adding 1.25x10⁻⁴ mol of H₂PtCl₆ to

the Brij C10 and cyclohexane, 6.25×10^{-4} mol of H_2PtCl_6 and 6.25×10^{-4} mol of a second metal precursor [$\text{Ni}(\text{NO}_3)_2 \cdot 6\text{H}_2\text{O}$, $\text{CuCl}_2 \cdot 2\text{H}_2\text{O}$, $\text{CoCl}_2 \cdot 6\text{H}_2\text{O}$, or $\text{SnCl}_4 \cdot 5\text{H}_2\text{O}$] were mixed together and added to the organic solution simultaneously.

Creating Monodisperse Ni@SiO₂. In 2, 5 mL round bottom flasks, 0.85 g of Brij C10 and 1.5 mL of cyclohexane were added and stirred for 30 min at 50 °C. A solution containing 2.5×10^{-5} mol of $\text{Ni}(\text{NO}_3)_2 \cdot 6\text{H}_2\text{O}$ was dissolved in 0.1 mL of ultrapure water and added to the round bottom flasks dropwise with a plastic pipette and then stirred for 20 min. Then, 0.16 mL of 14.8 M NH_4OH was added dropwise and stirred for a variable time (2 or 30 min). Next, 0.030 mL of 3-aminopropyl trimethoxysilane was added dropwise and stirred for 2 min. A syringe pump was used to add 0.4 mL of tetraethyl orthosilicate and the samples were stirred for 2 hrs. To disrupt the microemulsion, 1 mL of ethanol was added. The sample was centrifuged at 3000 rpm for 10 min and washed 3x with ethanol. The samples were dried using rotary evaporation and then reduced at 600 °C for 1 hr after using a ramping rate of 5 °C/min to reach 600 °C.

Creating Ni@SiO₂ with Larger Ni Cores (Nix₂@SiO₂ and Nix₄@SiO₂). The above procedure, where the variable time of 30 min between the addition of NH_4OH and APTMS, was utilized with a modified $\text{Ni}(\text{NO}_3)_2 \cdot 6\text{H}_2\text{O}$ concentration. To synthesize Nix₂@SiO₂ and Nix₄@SiO₂, respectively, 5.0×10^{-5} mol and 1.0×10^{-4} mol of $\text{Ni}(\text{NO}_3)_2 \cdot 6\text{H}_2\text{O}$ was dissolved in ultrapure water to create the Ni precursor solutions.

Synthesis of Silica Cores (I-SiO₂). In 2, 100 mL round bottom flasks, 1.99 g of Igepal CO-520 and 40 mL of cyclohexane was added and stirred at room temperature for 5 min. To repeat the reported procedure, 0.280 mL of 14.8 M NH_4OH was injected and stirred for 30 min. To modify the procedure to allow for addition of metal precursors, 56

μL of H_2O was added dropwise and stirred for 20 min, then 0.224 mL of 14.8 M NH_4OH was injected and stirred for 30 min. Lastly, 350 μL of TEOS was injected and stirred for 48 hrs. To disrupt the microemulsion, 40 mL of MeOH was added and the samples were centrifuged at 12000 rpm for 30 min at 30 °C. The samples were washed 1x with methanol at 12000 rpm for 30 min at 30 °C, then washed 1x with ice cold ultrapure H_2O at 12000 rpm for 30 min at 20 °C. The samples were dispersed in 20 mL of ice cold ultrapure H_2O and stored in the fridge until use.

One-pot Coating and Etching of Silica Cores (I-mSiO₂). In 5 mL round bottom flasks, 200 mg of cetyltrimethylammonium chloride (CTAC) was dissolved in 2 mL of ultrapure water using sonication. Next, 2.755 μL of triethylamine (TEA) and a small stir bar were added and the flasks were stirred at room temperature for 1 hr. Afterwards, 1 mL of I-SiO₂ dispersed in water was added and stirred for 1 hr. Next, 15 μL of TEOS was added and the sample was heated in an 80 °C water bath for 1 hr. The water bath was then cooled to 50 °C over 30 min. The stir speed was adjusted to 1500 rpm, 63.6 mg of Na_2CO_3 was added, and the samples were stirred at 750 rpm for 30 min. The samples were removed from heat, washed 3x with H_2O and 1x with ethanol, and stored in the fridge.

Modification of I-SiO₂ synthesis to accommodate Ni addition (Ni@I-mSiO₂). Instead of adding 56 μL of ultrapure H_2O during the synthesis of the core, 56 μL of ultrapure water containing 3.0×10^{-4} mol of $\text{Ni}(\text{NO}_3)_2 \cdot 6\text{H}_2\text{O}$ was added. The same conditions were used to coat and etch the core as was used for synthesizing I-mSiO₂. The samples were dried using a rotary evaporator. The samples were further dried under 10%

H₂/Ar at 100 °C for 1 hr, and then the temperature was increased to 300 °C for 1 hr using a ramping rate of 1 °C/min to reduce the catalyst.

***In situ* Reduction of Pd(NO₃)₂ and AgNO₃ with Glucose (PdAg-glucose@I-mSiO₂).** In a 100 mL round bottom flask, 1.99 g of Igepal CO-520 and 40 mL of cyclohexane was added and stirred at room temperature for 5 min. A solution of 2.5x10⁻⁵ mol of Pd(NO₃)₂ and 2.5x10⁻⁵ mol of AgNO₃ dissolved in 20 μL of ultrapure water was added dropwise and stirred for 20 min. Next, 1.0x10⁻⁴ mol of glucose dissolved in 36 μL of H₂O was added dropwise and stirred for 30 min. Afterwards, 0.224 mL of 14.8 M NH₄OH was injected and stirred for 30 min. Lastly, 350 μL of TEOS was injected and stirred for 48 hrs. To disrupt the microemulsion, 40 mL MeOH was added and the samples were centrifuged at 12000 rpm for 30 min at 30 °C. The samples were washed 1x with methanol at 12000 rpm for 30 min at 30 °C, then washed 1x with ice cold ultrapure H₂O at 12000 rpm 30 min 20 °C. The samples were dispersed in 20 mL ice cold ultrapure H₂O and stored in the fridge until use. The samples synthesized at this point are designated PdAg-glucose@I-SiO₂. The same conditions were used to coat and etch the core as was used for synthesizing I-mSiO₂. The same conditions were used to reduce and dry the catalyst as was used for Ni@I-mSiO₂. Additionally, a PdAg-glucose@I-SiO₂ sample was reduced at 300 °C before completing the coating and etching conditions described for Ni@SiO₂.

Synthesis of PdAg-additive@I-mSiO₂ [Additive = Polyvinyl Pyrrolidone (PVP), 5,5'-methylenedisalicylic acid (MDSA), Pyridinium p-toluenesulfonate (PPTS), or Monosodium 2-sulfoterephthalate (MSSTP). Core synthesis is the same as PdAg-glucose@I-mSiO₂, but contains different additives. In all cases, 2.5x10⁻⁵ mol of

$\text{Pd}(\text{NO}_3)_2$ and AgNO_3 were used in the precursor solution. When PVP was the additive, 11.11 mg of PVP (1.0×10^{-4} mol of vinylpyrrolidone monomers) was used as the additive. When MDSA, PPTS, or MSSTP was the additive, 1.0×10^{-4} mol of the additive was present. A control with no additive present was also synthesized (PdAg@I-SiO_2). For the one-pot coating and etching process in this procedure the scale was 2x higher (e.g. 400 mg of CTAC was used) compared to the synthesis of $\text{PdAg-glucose@I-mSiO}_2$. The etched samples were dried for 3 hrs in an 80°C oven and reduced at 200°C for 2 hrs.

One-pot Coating and Etching of PdAg@I-mSiO_2 in the Presence of 3-mercaptopropyl Trimethoxysilane (MPTMS). The control PdAg@I-SiO_2 synthesized with no additive in the previous procedure was used in this synthesis. In 4, 10 mL round bottom flasks, 400 mg of cetyltrimethylammonium chloride (CTAC) was dissolved in 4 mL of ultrapure water using sonication. Next, 5.51 μL of triethylamine (TEA) and a small stir bar were added and the flasks and were stirred at room temperature for 1 hr. Afterwards, 2 mL of PdAg@I-SiO_2 dispersed in water was added and stirred for 1 hr. Next, 30 μL of TEOS (PdAg@I-mSiO_2), 24 μL of TEOS and 5.03 μL of MPTMS ($\text{PdAg@I-SF20-mSiO}_2$), 18 μL of TEOS and 10.06 μL of MPTMS ($\text{PdAg@I-SF40-mSiO}_2$), or 9 μL of TEOS and 5.03 μL of MPTMS ($\text{PdAg@SF40@I-mSiO}_2$) was added and the sample was heated in an 80°C water bath for 1 hr. For the sample with 9 μL of TEOS and 5.03 μL of MPTMS, an additional 15 μL of TEOS was added after the 1 hr at 80°C was completed and it was stirred at 80°C for 1 more hr. The samples were cooled to room temperature, and 30% H_2O_2 was added so the volume ratio of MPTMS/ H_2O_2 solution was 0.25/1.00. These samples were stirred at room temperature for 24 hr. The water bath was then heated to 50°C over 30 min. The stir speed was adjusted to 1500

rpm, 127.2 mg of Na_2CO_3 was added, and the samples were stirred at 750 rpm for 30 min. The samples were removed from heat, washed 3x with H_2O and 1x with ethanol, and stored in the fridge. The etched samples were dried 3 hrs in an 80 °C oven and reduced at 200 °C for 2 hrs.

Characterization. Inductively coupled plasma – mass spectroscopy (ICP-MS) measurements were performed using a Thermo Fisher Scientific XSeries 2 ICP-MS. To prepare samples for ICP-MS, samples were digested with 2 mL of aqua regia and 100 μL of HF at 110 °C. The samples were diluted to 50 mL with ultrapure water, then 1 mL of this was transferred to a centrifuge tube and diluted to 50 mL with 2 wt.% HNO_3 . Powder X-ray diffraction (XRD) patterns were collected at room temperature using a STOE Stadi P powder diffractometer equipped with an image plate and a $\text{CuK}_{\alpha 1}$ radiation source ($\lambda = 1.54056 \text{ \AA}$). All XRD patterns were calibrated using a Si standard after measurements were complete. All transmission electron microscopy (TEM) samples were prepared using the drop cast method⁵⁰⁻⁵¹ with the exception of PdAg based samples. These samples were prepared by sonicating 0.10 mg of sample in 250 μL of ethanol and adding the sample dropwise to a TEM grid. TEM images were collected using a TECNAI G2 F20 instrument at an acceleration voltage of 200kV. The particle size distributions for all imaged particles was calculated using the Particle Size Analyzer macro⁵² on ImageJ software⁵³ by measuring at least 100 randomly chosen particles. Dynamic light scattering (DLS) measurements were collected with a Malvern Zetasizer Nano ZS90 after diluting the as synthesized particles with 20 mL of ultrapure water. When designing the method, SiO_2 was the material, water was the dispersant, refractive indices used corresponded to these materials at 25 °C, and the absorbance was set at 0.200. During the measurements,

1 mL of each sample was transferred to a plastic cuvette, and a 633 nm laser was used to complete the analysis.

References

- (1) Zhang, T. T.; Zhao, H. Y.; He, S. N.; Liu, K.; Liu, H. Y.; Yin, Y. D.; Gao, C. B., Unconventional Route to Encapsulated Ultrasmall Gold Nanoparticles for High-Temperature Catalysis. *ACS Nano* **2014**, *8*, 7297-7304.
- (2) Takenaka, S.; Umabayashi, H.; Tanabe, E.; Matsune, H.; Kishida, M., Specific Performance of Silica-Coated Ni Catalysts for the Partial Oxidation of Methane to Synthesis Gas. *J. Catal.* **2007**, *245*, 392-400.
- (3) Li, Z. W.; Mo, L. Y.; Kathiraser, Y.; Kawi, S., Yolk-Satellite-Shell Structured Ni-Yolk@Ni@SiO₂ Nanocomposite: Superb Catalyst toward Methane CO₂ Reforming Reaction. *ACS Catal.* **2014**, *4*, 1526-1536.
- (4) Takenaka, S.; Orita, Y.; Umabayashi, H.; Matsune, H.; Kishida, M., High Resistance to Carbon Deposition of Silica-Coated Ni Catalysts in Propane Stream Reforming. *Applied Catalysis A: General* **2008**, *351*, 189-194.
- (5) Takenaka, S.; Orita, Y.; Matsune, H.; Tanabe, E.; Kishida, M., Structures of Silica-Supported Co Catalysts Prepared Using Microemulsion and Their Catalytic Performance for the Formation of Carbon Nanotubes through the Decomposition of Methane and Ethylene. *J. Phys. Chem. C* **2007**, *111*, 7748-7756.
- (6) Song, H.; Tan, B.; Ozkan, U. S., Novel Synthesis Techniques for Preparation of Co/CeO₂ as Ethanol Steam Reforming Catalysts. *Catalysis Letters* **2009**, *132*, 422-429.
- (7) Wu, S. H.; Tseng, C. T.; Lin, Y. S.; Lin, C. H.; Hung, Y.; Mou, C. Y., Catalytic Nano-Rattle of Au@Hollow Silica: Towards a Poison-Resistant Nanocatalyst. *J. Mater. Chem.* **2011**, *21*, 789-794.
- (8) Stuart, M. A. C.; Fleer, G. J.; Bijsterbosch, B. H., The Adsorption of Polyvinyl Pyrrolidone) onto Silica 1. Adsorbed Amount. *J. Colloid Interface Sci.* **1982**, *90*, 310-320.
- (9) Stuart, M. A. C.; Fleer, G. J.; Bijsterbosch, B. H., Adsorption of Polyvinyl Pyrrolidone) on Silica. 2. The Fraction of Bound Segments, Measured by a Variety of Techniques. *J. Colloid Interface Sci.* **1982**, *90*, 321-334.

- (10) Nelson, A.; Jack, K. S.; Cosgrove, T.; Kozak, D., NMR Solvent Relaxation in Studies of Multicomponent Polymer Adsorption. *Langmuir* **2002**, *18*, 2750-2755.
- (11) Zhang, Q.; Zhang, T. R.; Ge, J. P.; Yin, Y. D., Permeable Silica Shell through Surface-Protected Etching. *Nano Lett.* **2008**, *8*, 2867-2871.
- (12) Hu, Y. X.; Zhang, Q.; Goebel, J.; Zhang, T. R.; Yin, Y. D., Control over the Permeation of Silica Nanoshells by Surface-Protected Etching with Water. *Phys. Chem. Chem. Phys.* **2010**, *12*, 11836-11842.
- (13) Zhang, T. R.; Zhang, Q.; Ge, J. P.; Goebel, J.; Sun, M. W.; Yan, Y. S.; Liu, Y. S.; Chang, C. L.; Guo, J. H.; Yin, Y. D., A Self-Templated Route to Hollow Silica Microspheres. *J. Phys. Chem. C* **2009**, *113*, 3168-3175.
- (14) Yu, Q. Y.; Hui, J. F.; Wang, P. P.; Wang, X., Anion-Exchange-Driven Disassembly of a SiO₂/CTAB Composite Mesophase: The Formation of Hollow Mesoporous Silica Spheres. *Inorg. Chem.* **2012**, *51*, 9539-9543.
- (15) Zhang, H. N.; Zhou, Y.; Li, Y. R.; Bandosz, T. J.; Akins, D. L., Synthesis of Hollow Ellipsoidal Silica Nanostructures Using a Wet-Chemical Etching Approach. *J. Colloid Interface Sci.* **2012**, *375*, 106-111.
- (16) Chen, F.; Hong, H.; Shi, S. X.; Goel, S.; Valdovinos, H. F.; Hernandez, R.; Theuer, C. P.; Barnhart, T. E.; Cai, W. B., Engineering of Hollow Mesoporous Silica Nanoparticles for Remarkably Enhanced Tumor Active Targeting Efficacy. *Sci. Rep.* **2014**, *4*, 10.
- (17) Fang, X. L.; Chen, C.; Liu, Z. H.; Liu, P. X.; Zheng, N. F., A Cationic Surfactant Assisted Selective Etching Strategy to Hollow Mesoporous Silica Spheres. *Nanoscale* **2011**, *3*, 1632-1639.
- (18) Wu, C. Z.; Lim, Z. Y.; Zhou, C.; Wang, W. G.; Zhou, S. H.; Yin, H. F.; Zhu, Y. J., A Soft-Templated Method to Synthesize Sintering-Resistant Au-Mesoporous-Silica Core-Shell Nanocatalysts with Sub-5 nm Single-Cores. *Chem. Commun.* **2013**, *49*, 3215-3217.
- (19) Chen, J. C.; Zhang, R. Y.; Han, L.; Tu, B.; Zhao, D. Y., One-Pot Synthesis of Thermally Stable Gold@Mesoporous Silica Core-Shell Nanospheres with Catalytic Activity. *Nano Research* **2013**, *6*, 871-879.
- (20) Joo, S. H.; Park, J. Y.; Tsung, C. K.; Yamada, Y.; Yang, P. D.; Somorjai, G. A., Thermally Stable Pt/Mesoporous Silica Core-Shell Nanocatalysts for High-Temperature Reactions. *Nat. Mater.* **2009**, *8*, 126-131.
- (21) Teng, Z. G.; Su, X. D.; Zheng, Y. Y.; Sun, J.; Chen, G. T.; Tian, C. C.; Wang, J. D.; Li, H.; Zhao, Y. N.; Lu, G. M., Mesoporous Silica Hollow Spheres with Ordered

- Radial Mesochannels by a Spontaneous Self-Transformation Approach. *Chem. Mat.* **2013**, *25*, 98-105.
- (22) Wu, M.; Chen, Y.; Zhang, L.; Li, X.; Cai, X.; Du, Y.; Zhang, L.; Shi, J., A Salt-Assisted Acid Etching Strategy for Hollow Mesoporous Silica/Organosilica for pH-Responsive Drug and Gene Co-Delivery. *Journal of Materials Chemistry B* **2015**, *3*, 766-775.
- (23) Yildirim, A.; Bayindir, M., A Porosity Difference Based Selective Dissolution Strategy to Prepare Shape-Tailored Hollow Mesoporous Silica Nanoparticles. *Journal of Materials Chemistry A* **2015**.
- (24) Zhang, T. R.; Ge, J. P.; Hu, Y. X.; Zhang, Q.; Aloni, S.; Yin, Y. D., Formation of Hollow Silica Colloids through a Spontaneous Dissolution-Regrowth Process. *Angewandte Chemie-International Edition* **2008**, *47*, 5806-5811.
- (25) Park, S. J.; Kim, Y. J.; Park, S. J., Size-Dependent Shape Evolution of Silica Nanoparticles into Hollow Structures. *Langmuir* **2008**, *24*, 12134-12137.
- (26) Lin, Y. S.; Wu, S. H.; Tseng, C. T.; Hung, Y.; Chang, C.; Mou, C. Y., Synthesis of Hollow Silica Nanospheres with a Microemulsion as the Template. *Chem. Commun.* **2009**, 3542-3544.
- (27) Lin, C. H.; Liu, X. Y.; Wu, S. H.; Liu, K. H.; Mou, C. Y., Corking and Uncorking a Catalytic Yolk-Shell Nanoreactor: Stable Gold Catalyst in Hollow Silica Nanosphere. *J. Phys. Chem. Lett.* **2011**, *2*, 2984-2988.
- (28) Jmol: An Open-Source Java Viewer for Chemical Structures in 3D. <http://www.jmol.org/> (accessed 8/12/15).
- (29) Han, Y.; Jiang, J.; Lee, S. S.; Ying, J. Y., Reverse Microemulsion-Mediated Synthesis of Silica-Coated Gold and Silver Nanoparticles. *Langmuir* **2008**, *24*, 5842-5848.
- (30) Wang, H. L.; Schaefer, K.; Moeller, M., In Situ Immobilization of Gold Nanoparticle Dimers in Silica Nanoshell by Microemulsion Coalescence. *J. Phys. Chem. C* **2008**, *112*, 3175-3178.
- (31) Zhang, Z. Y.; Xiao, F.; Xi, J. B.; Sun, T.; Xiao, S.; Wang, H. R.; Wang, S.; Liu, Y. Q., Encapsulating Pd Nanoparticles in Double-Shelled Graphene@Carbon Hollow Spheres for Excellent Chemical Catalytic Property. *Sci. Rep.* **2014**, *4*, 5.
- (32) Yadav, M.; Akita, T.; Tsumori, N.; Xu, Q., Strong Metal-Molecular Support Interaction (SMMSI): Amine-Functionalized Gold Nanoparticles Encapsulated in Silica Nanospheres Highly Active for Catalytic Decomposition of Formic Acid. *J. Mater. Chem.* **2012**, *22*, 12582-12586.

- (33) Osseo-Asare, K.; Arriagada, F. J., Growth Kinetics of Nanosize Silica in a Nonionic Water-in-Oil Microemulsion: A Reverse Micellar Pseudophase Reaction Model. *J. Colloid Interface Sci.* **1999**, *218*, 68-76.
- (34) Xu, L.; Wu, X. C.; Zhu, J. J., Green Preparation and Catalytic Application of Pd Nanoparticles. *Nanotechnology* **2008**, *19*, 6.
- (35) Kheybari, S.; Samadi, N.; Hosseini, S. V.; Fazeli, A.; Fazeli, M. R., Synthesis and Antimicrobial Effects of Silver Nanoparticles Produced by Chemical Reduction Method. *Daru* **2010**, *18*, 168-172.
- (36) Chou, K. S.; Lu, Y. C.; Lee, H. H., Effect of Alkaline Ion on the Mechanism and Kinetics of Chemical Reduction of Silver. *Mater. Chem. Phys.* **2005**, *94*, 429-433.
- (37) Pei, G. X.; Liu, X. Y.; Wang, A. Q.; Lee, A. F.; Isaacs, M. A.; Li, L.; Pan, X. L.; Yang, X. F.; Wang, X. D.; Tai, Z. J.; Wilson, K.; Zhang, T., Ag Alloyed Pd Single-Atom Catalysts for Efficient Selective Hydrogenation of Acetylene to Ethylene in Excess Ethylene. *ACS Catal.* **2015**, *5*, 3717-3725.
- (1) Rimola, A.; Costa, D.; Sodupe, M.; Lambert, J. F.; Ugliengo, P., Silica Surface Features and Their Role in the Adsorption of Biomolecules: Computational Modeling and Experiments. *Chem. Rev.* **2013**, *113*, 4216-4313.
- (2) Xiong, Y. J.; Washio, I.; Chen, J. Y.; Cai, H. G.; Li, Z. Y.; Xia, Y. N., Poly(Vinyl Pyrrolidone): A Dual Functional Reductant and Stabilizer for the Facile Synthesis of Noble Metal Nanoplates in Aqueous Solutions. *Langmuir* **2006**, *22*, 8563-8570.
- (3) Huang, H. H.; Ni, X. P.; Loy, G. L.; Chew, C. H.; Tan, K. L.; Loh, F. C.; Deng, J. F.; Xu, G. Q., Photochemical Formation of Silver Nanoparticles in Poly(N-Vinylpyrrolidone). *Langmuir* **1996**, *12*, 909-912.
- (4) Zhang, Z. T.; Zhao, B.; Hu, L. M., Pvp Protective Mechanism of Ultrafine Silver Powder Synthesized by Chemical Reduction Processes. *J. Solid State Chem.* **1996**, *121*, 105-110.
- (5) Hubicki, Z. K. s., D., *Selective Removal of Heavy Metal Ions from Waters and Waste Waters Using Ion Exchange Methods, Ion Exchange Technologies*, 2012.
- (6) Itoh, T.; Mase, T., Practical Thiol Surrogates and Protective Groups for Arylthiols for Suzuki-Miyaura Conditions. *J. Org. Chem.* **2006**, *71*, 2203-2206.
- (7) Zeysing, B.; Gosch, C.; Terfort, A., Protecting Groups for Thiols Suitable for Suzuki Conditions. *Org. Lett.* **2000**, *2*, 1843-1845.

- (8) Choi, K. M.; Na, K.; Somorjai, G. A.; Yaghi, O. M., Chemical Environment Control and Enhanced Catalytic Performance of Platinum Nanoparticles Embedded in Nanocrystalline Metal-Organic Frameworks. *J. Am. Chem. Soc.* **2015**, *137*, 7810-7816.
- (9) Zhou, S. D.; Qian, C.; Chen, X. Z., Solvent-Free Synthesis of Thiophenol Using Uncatalyzed Transfer Hydrogenation. *Synth. Commun.* **2012**, *42*, 2432-2439.
- (10) Numata, T.; Awano, H.; Oae, S., Direct Reduction of Sulfonic-Acid to the Corresponding Thiol with Trifluoroacetic Anhydride-Tetrabutylammonium Iodide System. *Tetrahedron Lett.* **1980**, *21*, 1235-1238.
- (11) Fujimori, K.; Togo, H.; Oae, S., Iodine Catalyzed Reduction of Arenesulfonic Acid to the Arenethiol with Triphenylphosphine. *Tetrahedron Lett.* **1980**, *21*, 4921-4924.
- (12) Oae, S.; Togo, H., Reduction of Sulfonic-Acids and Related Organosulfur Compounds with Triphenylphosphine-Iodine System. *Bull. Chem. Soc. Jpn.* **1983**, *56*, 3802-3812.
- (13) Huang, W. Y.; Qian, W.; El-Sayed, M. A., Coherent Vibrational Oscillation in Gold Prismatic Monolayer Periodic Nanoparticle Arrays. *Nano Lett.* **2004**, *4*, 1741-1747.
- (14) Huang, W. Y.; Qian, W.; El-Sayed, M. A., The Optically Detected Coherent Lattice Oscillations in Silver and Gold Monolayer Periodic Nanoprism Arrays: The Effect of Interparticle Coupling. *J. Phys. Chem. B* **2005**, *109*, 18881-18888.
- (15) Sperling, R. Particle Size Analyzer Macro for ImageJ. <http://code.google.com/p/psa-macro/> (accessed 8/11/15).
- (16) Schneider, C. A.; Rasband, W. S.; Eliceiri, K. W., NIH Image to ImageJ: 25 Years of Image Analysis. *Nat. Methods* **2012**, *9*, 671-675.

CHAPTER 4

CONCLUSIONS AND FUTURE OPPORTUNITIES

Previous publications have demonstrated enhanced activity and α,β -alcohol selectivity in the presence of Pt-Fe alloys¹ or capping agent protected Pt-Fe alloys.² The latter has claimed that capping agents alone enhance activity and cinnamyl alcohol selectivity over Pt-Fe alloys during cinnamaldehyde hydrogenation. These controversial results have generated the need to elucidate the extent that capping agents and Fe contribute to enhancements in activity and cinnamyl alcohol selectivity over Pt catalysts.

We successfully synthesized $\text{Pt}_5\text{Fe}_x@\text{mSiO}_2$ samples with Fe/Pt ratios of 1/2.5 and 1/5 and a control catalyst with only Pt present to determine the effects of adding a base metal on cinnamaldehyde hydrogenation reactions. The trends for Fe inclusion into the Pt core were observed through increases in XRD crystallite size and particle size increases in TEM, and this was confirmed using ICP-MS. It was found that selectivity for this reaction can be enhanced by adding Fe alone, which is in agreement with previous reports.^{1, 3-4} Enhanced selectivity during cinnamaldehyde hydrogenation is more likely from changes in electronic effects compared to changes in geometric effects, because the Pt $4f_{7/2}$ electron binding energy was more closely correlated with cinnamyl alcohol selectivity than the Fe/Pt ratio. The slightly higher selectivity observed for the 700 °C reduced catalysts compared to the 300 °C and 500 °C reduced catalysts could result from smaller mesopores increasing steric hindrance,⁵⁻⁶ which prevents the C=C bond from interacting with the catalyst surface.

In contrast, enhanced activity during the cinnamaldehyde hydrogenation reactions was found to be correlated with increasing hydrophobicity of ligands present only when using Pt_5Fe_2 reduced at 300 °C and Pt_5Fe reduced at 500 °C during the reactions.

Physisorption studies were completed to test if ligands and reactants could theoretically reach the catalyst surface, and it was found that the pore size remained greater than 2 nm in diameter after the harshest high temperature treatment applied. The longest ligand, perfluorodecanoic acid, is approximately 70% of the pore diameter, indicating that ligands can theoretically diffuse easily to the core. After submersing $\text{Pt}_5\text{Fe}@m\text{SiO}_2$ and $\text{Pt}@m\text{SiO}_2$ in solutions containing decanoic and perfluorodecanoic acid capping agents, DRIFTS studies were completed and it was proven that bonds were present between the acids and the catalyst surface. The enhancement in activity upon addition of hydrophobic ligands might occur because the conjugated double bonds present in cinnamaldehyde cause the molecule to be more non-polar than the n-hexane solvent. Noncovalent interactions would therefore draw the molecule into the mesoporous channels. However, the observed enhancements in conversion are less predictable than enhancements observed in cinnamyl alcohol selectivity. Enhancements in conversion are likely affected by a variety of changes, including reduction temperature, ligand hydrophobicity, support hydrophobicity, and Fe/Pt ratios.

Even though perfluorinated capping agents have been shown to provide enhanced catalytic activity compared to saturated ligands and bare surfaces, their presence in the pores might still increase diffusion times for the transport of reactants in the pores by introducing steric hindrance. Additionally, the presence of free acids during reactions could affect the pH during the reaction. To test if steric hindrance and acidity affects the

reaction, hydrophobic silica precursors such as triethoxyfluorosilane (TEFS) can be utilized during coating processes to create hydrophobic Si-F bonds, which are stable above 500 °C⁷ and have been utilized in separation⁷ and liquid phase⁸⁻¹⁰ catalytic systems. Since TEFS can be mixed with tetraethyl orthosilicate before introducing the precursors, this has the benefit of decreasing the number of steps in the catalytic process, too. We plan to add TEFS to the mesoporous shell during the Pt coating process, convert Pt to Pt₅Fe, and reduce it at 500 °C, because the perfluorinated ligand capped catalyst with this composition and reduction temperature was found to have the highest activity and cinnamyl alcohol selectivity.

We have also laid the groundwork for a scalable two-pot synthesis of yolk-shell intermetallic compounds encapsulated with mesoporous SiO₂ with easily tunable metal ratios. It is believed that the loading efficiency of metals has been improved through the addition of organic compounds containing amide, carboxylic acid, and sulfonic acid functional groups because of the retention in color (an indication of the preservation of metal ions) after etching processes are complete. Additionally, adding sulfonic acid groups to the shell during coating processes might also help with metal retention during etching processes. However, several improvements and much characterization needs to be made before this can be turned into an industrial catalyst.

We believe that the addition of caffeine during the synthesis of the nanocapsules in the first step and the addition of sulfonic acid groups during the coating in the second step can enhance the metal retention during etching processes based on our TEM results in Figures 8c and 10e in Chapter 3. However, to test this idea, the synthesis needs to be scaled up, ICP-MS measurements of the solid and UV-vis measurements of the

supernatant after washing need to be completed, and the ratio of yolk-shell to empty shell particles needs to be determined for each sample. Additionally, when 3-mercaptopropyl trimethoxysilane is added to the shell, the degree of cetyltrimethylammonium chloride (CTAC) templating in the shell is unknown. As a result, extraction of CTAC using acetic acid or NaCl may be necessary to create a mesoporous structure. The porosity of the structure must therefore be determined by using the desorption branch of the BET isotherm to calculate BJH pore sizes.

The color of the PdAg@SF40@I-mSiO₂ samples after oxidizing the thiol groups with H₂O₂ also does not change over a 24 hr period, and DRIFTS studies must also be done to confirm this conversion is complete. Otherwise, thiol is expected to act as a catalyst poison when using Pd as a catalyst,¹¹ and low activity would be anticipated when using this structure for reactions. If the sulfonic acid groups are indeed present we will move on to complete catalytic reactions, because thiol groups would be below the detection limit and might not significantly poison catalyst surfaces. When developing these catalysts for reactions, the core size will need to be increased through the addition of more metal precursor during the synthesis of the nanocapsule in the first step to create a larger intermetallic core that can be more easily characterized with XRD. This will allow us to correlate enhanced activity and selectivity with a specific crystal phase present in intermetallic catalysts. The metal ratios will also be tuned to test which crystal phases correspond to the highest activity and selectivity during reactions.

References

- (1) Mahata, N.; Goncalves, F.; Pereira, M. F. R.; Figueiredo, J. L., Selective Hydrogenation of Cinnamaldehyde to Cinnamyl Alcohol over Mesoporous Carbon Supported Fe and Zn Promoted Pt Catalyt. *Appl. Catal. A-Gen.* **2008**, *339*, 159-168.
- (2) Vu, K. B.; Bukhryakov, K. V.; Anjum, D. H.; Rodionov, V. O., Surface-Bound Ligands Modulate Chemoselectivity and Activity of a Bimetallic Nanoparticle Catalyst. *ACS Catal.* **2015**, 2529-2533.
- (3) Gallezot, P.; Richard, D., Selective Hydrogenation of Alpha, Beta-Unsaturated Aldehydes. *Catal. Rev.-Sci. Eng.* **1998**, *40*, 81-126.
- (4) Lee, J.; Kim, Y. T.; Huber, G. W., Aqueous-Phase Hydrogenation and Hydrodeoxygenation of Biomass-Derived Oxygenates with Bimetallic Catalysts. *Green Chem.* **2014**, *16*, 708-718.
- (5) Durndell, L. J.; Parlett, C. M. A.; Hondow, N. S.; Isaacs, M. A.; Wilson, K.; Lee, A. F., Selectivity Control in Pt-Catalyzed Cinnamaldehyde Hydrogenation. *Sci. Rep.* **2015**, *5*, #9425.
- (6) Guo, Z. Y.; Xiao, C. X.; Maligal-Ganesh, R. V.; Zhou, L.; Goh, T. W.; Li, X. L.; Tesfagaber, D.; Thiel, A.; Huang, W. Y., Pt Nanoclusters Confined within Metal Organic Framework Cavities for Chemoselective Cinnamaldehyde Hydrogenation. *ACS Catal.* **2014**, *4*, 1340-1348.
- (7) Kosinov, N.; Sripathi, V. G. P.; Hensen, E. J. M., Improving Separation Performance of High-Silica Zeolite Membranes by Surface Modification with Triethoxyfluorosilane. *Microporous Mesoporous Mat.* **2014**, *194*, 24-30.
- (8) Nakatsuka, K.; Mori, K.; Okada, S.; Ikurumi, S.; Kamegawa, T.; Yamashita, H., Hydrophobic Modification of Pd/SiO₂@Single-Site Mesoporous Silicas by Triethoxyfluorosilane: Enhanced Catalytic Activity and Selectivity for One-Pot Oxidation. *Chem.-Eur. J.* **2014**, *20*, 8348-8354.
- (9) Kamegawa, T.; Mizuno, A.; Yamashita, H., Hydrophobic Modification of SO₃H-Functionalized Mesoporous Silica and Investigations on the Enhanced Catalytic Performance. *Catal. Today* **2015**, *243*, 153-157.
- (10) Wang, L.; Wang, H.; Liu, F. J.; Zheng, A. M.; Zhang, J.; Sun, Q.; Lewis, J. P.; Zhu, L. F.; Meng, X. J.; Xiao, F. S., Selective Catalytic Production of 5-Hydroxymethylfurfural from Glucose by Adjusting Catalyst Wettability. *ChemSusChem* **2014**, *7*, 402-406.

- (11) Marshall, S. T.; O'Brien, M.; Oetter, B.; Corpuz, A.; Richards, R. M.; Schwartz, D. K.; Medlin, J. W., Controlled Selectivity for Palladium Catalysts Using Self-Assembled Monolayers. *Nat. Mater.* **2010**, *9*, 853-858.

APPENDIX

SUPPLEMENTAL INFORMATION FOR CHAPTER 2

Table A1. Assignment of vibrational frequencies associated with peaks observed in DRIFTS spectra in Figures 7 - 11 in Chapter 2.

Sample ^a	Vibrational Frequency (cm ⁻¹)	Assignment	Reference
MCM-41 + Solvent	1083	Asymmetric Si-O-Si (TO ₃ Mode) in silica	2, 3, 4
MCM-41 + Solvent	1247	LO ₃ shoulder of TO ₃ mode in silica	3, 4
MCM-41 + DA	2960	Asymmetric CH ₃	1
MCM-41 + DA	2929	Asymmetric CH ₂	1, 8
MCM-41 + DA	2859	Symmetric CH ₂	1, 8
MCM-41 + DA	1721	C=O stretch, Symmetric C=O stretching	1, 13
MCM-41 + DA	1467	In-plane C-O-H	13
MCM-41 + DA	1461	In-plane C-O-H	1, 8
MCM-41 + DA	1410	In-plane C-O-H	13
MCM-41 + DA	1381	In-plane C-O-H	13
MCM-41 + PFDA	1773	C=O stretch	9
MCM-41 + PFDA	1368	Axial Stretch CF ₂	7
MCM-41 + PFDA	1333	Axial Stretch CF ₂	7
MCM-41 + PFDA	1233	Asymmetric Stretch CF ₂	7, 10
MCM-41 + PFDA	1214	C-C and C-C-C stretching and bending modes	10
MCM-41 + PFDA	1152	Symmetric CF ₂	7, 10
Pt ₅ Fe@mSiO ₂ + Solvent	1959	SiO ₂ Overtone	12
Pt ₅ Fe@mSiO ₂ + Solvent	1865	SiO ₂ Overtone	12
Pt ₅ Fe@mSiO ₂ + Solvent	1631	H ₂ O Bending	12
Pt ₅ Fe@mSiO ₂ + DA	1596	Asymmetric -COO ⁻	6
Pt ₅ Fe@mSiO ₂ + DA	1533	CH ₂ vibration	5, 6
Pt ₅ Fe@mSiO ₂ + DA	1445	Symmetric -COO ⁻	8
Pt ₅ Fe@mSiO ₂ + PFDA	1680	Asymmetric -COO ⁻ in adsorbed acid	11
Pt ₅ Fe@mSiO ₂ + PFDA	1604	Asymmetric -COO ⁻ in adsorbed acid	11
Pt ₅ Fe@mSiO ₂ + PFDA	1434	Symmetric -COO ⁻ in adsorbed acid	1, 11
Pt ₅ Fe@mSiO ₂ + PFDA	1371	Axial CF ₂ Stretch	7
Pt ₅ Fe@mSiO ₂ + PFDA	1336	Axial CF ₂ Stretch	7
Pt@mSiO ₂ + DA	1720	C=O stretch, Symmetric C=O stretching	1, 13, 14
Pt@mSiO ₂ + DA	1586	Asymmetric -COO ⁻	6, 14
Pt@mSiO ₂ + DA	1553	CH ₂ vibration	5, 6
Pt@mSiO ₂ + DA	1445	Symmetric -COO ⁻	8
Pt@mSiO ₂ + DA	1412	Symmetric -COO ⁻ /CH ₂ Wag	14

^aDecanoic acid (DA), and perfluorodecanoic acid (PFDA)

Table A2. Binding energies of all elements in Pt@mSiO₂ and Pt₅Fe_x@mSiO₂ samples.

	Pt 4f _{7/2} B.E. (eV)	Fe 2p _{3/2} B.E. (eV)	Fe 2p _{3/2} Satellite B.E. (eV)	O 1s ^a	Si 2p	C 1s 1 st Peak	C 1s 2 nd Peak
Pt 700 °C	71.08	-	-	532.90	103.74	285.77	283.48
Pt ₅ Fe 300 °C	71.30	710.62	715.51	532.90	103.72	284.22	-
Pt ₅ Fe 500 °C	71.35	710.26	-	532.90	103.70	284.82	282.92
Pt ₅ Fe 700 °C	71.34	710.05	-	532.90	103.70	284.34	-
Pt ₅ Fe ₂ 700 °C	71.53	711.05	715.37	532.90	103.71	284.29	-

^aSpectra were calibrated to an O binding energy of 532.9 eV in SiO₂.

Table A3. Reference XPS electron emission peak locations.

Compound Type	Binding Energy Range (eV)	Reference
Pt	71.1 - 71.2	15
PtSi	72.8 - 73.3	15
Pt ₂ Si	72.3 - 72.7	15
PtCl ₂	73.4 - 73.8	15
Pt-Oxides	73.8 - 75.0	15
Pt(OH) ₂	72.4 - 72.8	15
Fe	706.7 - 707.2	15
FeO	709.2 - 709.6	15
Fe ₂ O ₃	710.7 - 710.9	15
FeOOH	711.3 - 711.8	15
O in SiO ₂	532.5 - 533.3	16
Si in SiO ₂	103.2 - 103.8	16
Carbide	280.7 - 283.0	15
Advantageous C	284.2 - 285.1	15
C with N	285.3 - 288.4	15
C with S	285.4 - 287.5	15
C with Cl	285.5 - 290.7	15
Satellite Type	Reported Binding Energies (eV)	Reference
Fe ²⁺	714.5, 715.0, 715.5	17, 18, 19
Fe ³⁺	719.0, 719.8, 718.8	17, 18, 19

References

- (1) Vu, K. B.; Bukhryakov, K. V.; Anjum, D. H.; Rodionov, V. O., Surface-Bound Ligands Modulate Chemoselectivity and Activity of a Bimetallic Nanoparticle Catalyst. *ACS Catal.* **2015**, 2529-2533.

- (2) Primeau, N.; Vautey, C.; Langlet, M., The Effect of Thermal Annealing on Aerosol-Gel Deposited SiO₂ Films: A FTIR Deconvolution Study. *Thin Solid Films* **1997**, *310*, 47-56.
- (3) Innocenzi, P., Infrared Spectroscopy of Sol-Gel Derived Silica-Based Films: A Spectra-Microstructure Overview. *J. Non-Cryst. Solids* **2003**, *316*, 309-319.
- (4) Almeida, R. M.; Pantano, C. G., Structural Investigation of Silica-Gel Films by Infrared-Spectroscopy. *Journal of Applied Physics* **1990**, *68*, 4225-4232.
- (5) Klokkenburg, M.; Hilhorst, J.; Erne, B. H., Surface Analysis of Magnetite Nanoparticles in Cyclohexane Solutions of Oleic Acid and Oleylamine. *Vib. Spectrosc.* **2007**, *43*, 243-248.
- (6) Abrahamson, H. B.; Lukaski, H. C., Synthesis and Characterization of Iron Stearate Compounds. *J. Inorg. Biochem.* **1994**, *54*, 115-130.
- (7) Gao, X. D.; Chorover, J., Adsorption of Perfluorooctanoic Acid and Perfluorooctanesulfonic Acid to Iron Oxide Surfaces as Studied by Flow-through ATR-FTIR Spectroscopy. *Environ. Chem.* **2012**, *9*, 148-157.
- (8) Shukla, N.; Liu, C.; Jones, P. M.; Weller, D., FTIR Study of Surfactant Bonding to FePt Nanoparticles. *Journal of Magnetism and Magnetic Materials* **2003**, *266*, 178-184.
- (9) Jouet, R. J.; Warren, A. D.; Rosenberg, D. M.; Bellitto, V. J.; Park, K.; Zachariah, M. R., Surface Passivation of Bare Aluminum Nanoparticles Using Perfluoroalkyl Carboxylic Acids. *Chem. Mat.* **2005**, *17*, 2987-2996.
- (10) Shao, T.; Zhang, P. Y.; Jin, L.; Li, Z. M., Photocatalytic Decomposition of Perfluorooctanoic Acid in Pure Water and Sewage Water by Nanostructured Gallium Oxide. *Appl. Catal. B-Environ.* **2013**, *142*, 654-661.
- (11) Karoyo, A. H.; Borisov, A. S.; Wilson, L. D.; Hazendonk, P., Formation of Host-Guest Complexes of Beta-Cyclodextrin and Perfluorooctanoic Acid. *J. Phys. Chem. B* **2011**, *115*, 9511-9527.
- (12) Benesi, H. A.; Jones, A. C., An Infrared Study of the Water-Silica Gel System. *J. Phys. Chem.* **1959**, *63*, 179-182.
- (13) Moreno, E.; Cordobilla, R.; Calvet, T.; Cuevas-Diarte, M. A.; Gbabode, G.; Negrier, P.; Mondieig, D.; Oonk, H. A. J., Polymorphism of Even Saturated Carboxylic Acids from N-Decanoic to N-Eicosanoic Acid. *New J. Chem.* **2007**, *31*, 947-957.

- (14) Petroski, J.; El-Sayed, M. A., FTIR Study of the Adsorption of the Capping Material to Different Platinum Nanoparticle Shapes. *J. Phys. Chem. A* **2003**, *107*, 8371-8375.
- (15) Moulder, J. F. S., W. F.; Sobol, P. E.; Bomben, K. D., *Handbook of X-Ray Photoelectron Spectroscopy: A Reference Book of Standard Spectra for Identification and Interpretation of XPS Data*; Physical Electronics Division, Perkin-Elmer Corp.: Eden Prairie, Mn, 1992.
- (16) C.D. Wagner, A. V. N., A. Kraut-Vass, J.W. Allison, C.J. Powell, J.R. Rumble NIST Standard Reference Database 20, Version 3.4 (Web Version). <http://srdata.nist.gov/xps/> (accessed 8/14/15).
- (17) Lin, T. C.; Seshadri, G.; Kelber, J. A., A Consistent Method for Quantitative XPS Peak Analysis of Thin Oxide Films on Clean Polycrystalline Iron Surfaces. *Appl. Surf. Sci.* **1997**, *119*, 83-92.
- (18) Brundle, C. R.; Chuang, T. J.; Wandelt, K., Core and Valence Level Photoemission Studies of Iron-Oxide Surfaces and Oxidation of Iron. *Surf. Sci.* **1977**, *68*, 459-468.
- (19) Yamashita, T.; Hayes, P., Analysis of XPS Spectra of Fe²⁺ and Fe³⁺ Ions in Oxide Materials. *Appl. Surf. Sci.* **2008**, *254*, 2441-2449.